Research Programme of the Research Fund for Coal and Steel

Steel RTD

Project carried out with a financial grant of the
Research Programme of the Research Fund for Coal and Steel

Robustness of car parks against localised fire

Grant Agreement Number RFSR-CT-2008-00036

Deliverable V: Practical behavioural models for car park structures towards design practice

March 2012

Authors:

Cheng Fang (ICST)
Bassam Izzuddin (ICST)
Ahmed Elghazouli (ICST)
David Nethercot (ICST)
Ludivine Comeliau (ULGG)
Jean-Pierre Jaspart (ULGG)
Jean-François Demonceau (ULGG)
Cécile Haremza (FCTUCOIMBRA)
Aldina Santiago (FCTUCOIMBRA)
Luís Simões da Silva (FCTUCOIMBRA)
Renata Obiala (ARCELORPROFIL)
Bin Zhao (CTICM)
Dhionis Dhima (CSTB)
Frédéric Gens (GREISCH)
Vincent de Ville (GREISCH)

Table of contents

I. Introduction 3

II. Analytical model of slabs 3

III. Global FEM model and its application to the reference car park 4

IV. Global analytical model and its application to the reference car park 5

V. References 6

Annex A – 3D behaviour of slabs further to a column loss

Annex B – Global FEM model and its application to the reference car park

Annex C – Global frame analytical model

I. Introduction

This deliverable is a continuation of the 'Deliverable IV: Development of FEM simulation of car parks under localised fire'. While Deliverable IV presents detailed FEM modelling guidelines, focus of this deliverable is more on practical behavioural models predicting the response of the car park structures by means of design-oriented approaches. Three issues are dealt with in this deliverable, namely, *analytical model of slabs*, *global FEM model and its application to the reference car park*, and *global analytical model and its application to the reference car park*.

1) *Analytical model of slabs*: following the numerical investigations on slabs as discussed in Deliverable IV, this deliverable further employs the analytical slab model developed by Omer *et al*., 2010 to illustrate its application to the current car park. The influence of slab boundary conditions is also discussed.
2) *Global FEM model and its application to the reference car park*: after the verification of the model reduction strategy discussed in Deliverable IV, the car park designed according to WP5 is investigated with ADAPTIC (Izzuddin, 1991) using the reduced models, specifically, reduced full slab and reduced grillage models. Four V3 class cars parked around an internal column are selected as the main scenario in this investigation.
3) *Global analytical model and its application to the reference car park*: in Liège, a global analytical model is proposed to predict the structural response of a building subject to column loss. Application of the global analytical model to the investigated car park is presented. Towards practical application, the analytical model is simplified, and the accuracy of the simplified model is justified.

II. Analytical model of slabs

In order to illstrate the application of the analytical slab model, it is assumed that a localised fire occurs near a supporting column. Also, it is considered that the unidirectional concrete ribs of the composite slabs do not significantly influence the behaviour of the slab when significant membrane effects are developed, i.e. it is assumed that only the upper part of the slab contributes to the slab resistance. Accordingly, the behaviour of the composite slab can be investigated through the study of a 3D uniform slab, subjected to the loss of one of its supporting columns, assuming that this slab remains at ambient temperature. The objective of this study is to show that the response of slab subject to column loss can be predicted through analytical methods, taking into account the membrane effects.

Before presenting the analytical model, a parametric numerical study is conducted to investigate the influence of the boundary conditions on the slab behaviour (Lemaire, 2010). It is observed that significant tension forces are developed in the centre of the slab, while a compression ring forms on the slab borders to equilibrate the central membrane forces. Importantly, the most critical case is the one where the slab is least restrained, so this most critical case is studied.

The basic assumptions and solving procedures of the simplified ambient temperature slab models developed by Omer *et al*., 2010 are recalled as follows:

- Main assumptions:

– No horizontal and rotational restraints at the slab edges (= simply supported edges)
– Slab subjected to uniformly distributed load (q)
– Uniform slab (constant thickness, no ribs)
– Single layer of reinforcement
– Orthotropic reinforcement (layers in the two directions assumed at the same level)
– Rigid-strain hardening material model for steel
– Negligible concrete tensile strength
– Concrete fully rigid in compression
– Bond-slip response described by a rigid-plastic law

- Solution procedure to obtain the $q - U_c$:

– choose a value of U_C, the central deflection of the slab
– by compatibility of displacements, find the elongations Δ_s of reinforcement in the different cracks
– knowing these elongations, determine the rebar forces T_s, according to the rigid-strain hardening law material
– knowing the elongations and the rebar forces, compute the internal dissipated energy $\dot{D}$ which is a function of U_c(through Δ_s and T_s) (all the energy is dissipated in the steel reinforcement and through bond-slip because concrete is assumed to be fully rigid)
– compute the external dissipated energy $\dot{E}$, which is a function of q, the uniformly distributed load acting on the slab
– find the q corresponding to the chosen U_c by writing $\dot{D} = \dot{E}$ ($\dot{D} = f(U_c)$ and $\dot{E} = f(q)$)

An illustration of the above procedure for the current car park is detailed in **Annex A**.

III. Global FEM model and its application to the reference car park

It is shown in Deliverable IV that the responses of the higher level model and lower level model are very close, which verifies that the reduced system model is capable of capturing the response of the overall structure subject to localised fire with sufficient accuracy, provided that the spring representing the response of upper ambient floors is accurately modelled. Therefore, in this study, reduced substructure models (Levels B and C) are employed for simulating the reference building, as shown in Figure 1.

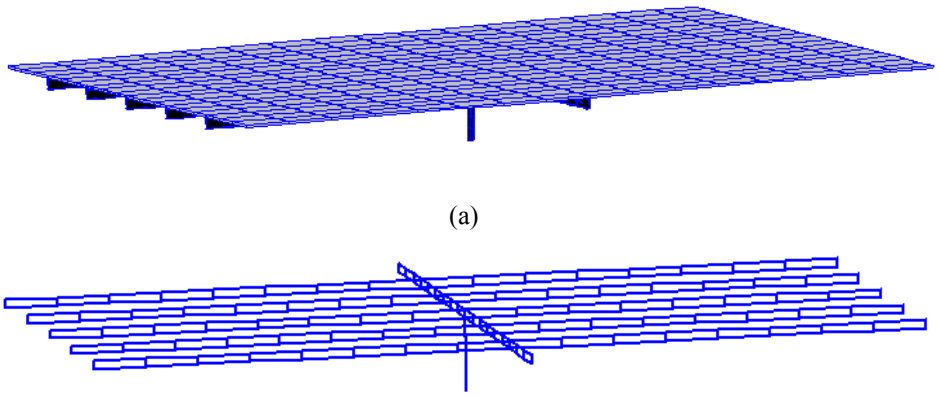

(a)

(b)

Figure 1. ADAPTIC substructure models: (a) Level B full slab model, (b) Level C grillage model

To illustrate the application of the numerical model to the current car park, a vehicle fire scenario is considered. The selected fire scenario assumes that four V3 class cars are parked around an internal column. The maximum heat release rate of each car is 8.3MW. The interval of the fire spreading from one car to another/other car/s is 12 minutes, and the history of temperature distribution within structural members (e.g. steel beams and composite slab) was captured at 3 minute intervals. The vertical distance between the fire origins and the ceiling is 2.4m. The finite element programme SAFIR (Franssen, 2005) was employed to conduct the thermal analysis for the car park under the selected fire scenario. The thermal output data were extracted and input into the finite element model established in ADAPTIC (Izzuddin, 1991) for structural analysis aided by HPC system.

A joint failure criterion (Fang *et al.*, 2010) is proposed for structural robustness assessment. Recent research (Izzuddin *et al.*, 2008) indicated that even the collapse of one floor can cause severe damage in the floor below for typical steel-framed composite constructions, thus triggering progressive collapse. Therefore, the definition of safe structure in this study is based on the avoidance of collapse in any of the affected floors; in other words, structural failure/progressive collapse occurs when the deformation of either the fire affected floor or the upper ambient floors exceeds their respective ductility capacity. In this respect, the failure of any floor system is attributed to the ductility failure of any surrounding

ambient joint on that floor, thus failure criteria are defined in terms of whether the ductility limits of the joint are exceeded. If the surrounding ambient joints have sufficient resistance, but the joints directly exposed to fire fails first, the structure is still deemed safe (Fang *et al.*, 2011).

Based on this failure criterion, the structural models are investigated. Three failure types were generally observed for the reference building subject to the selected fire scenarios, namely, 'single-span failure' type, 'double-span failure' type and 'shear failure' type. In addition, dynamic effects arise for the floor system following column buckling due to fire. The corresponding final floor deflection was found to fall between two idealised extreme cases, which are 'static column loss' and 'dynamic sudden column loss'. This suggests that in order to predict a reliable ductility demand of a car park subsequent to column loss due to vehicle fire, dynamic analysis that accurately models the column buckling process may be necessary. More discussion about the FEM model and the related outcomes is provided in **Annex B**.

IV. Global analytical model and its application to the reference car park

In this study, a general global analytical model is discussed. The global concept will be first introduced on a 2D frame, and then generalised to a 3D frame. Afterwards, this model is adapted to the scenario investigated within this project, i.e. the loss of a column in a parking structure under localised fire. In particular, the main assumptions leading to a simplification of the global model will be considered.

- 2D analytical frame model

  For this model, the beneficial effects of the slab are not considered. The study is focusing on frames which are only comprised of columns and beams. No dynamics effects are considered and the method is for ambient temperature. The analysis procedure includes:

  1) Extraction of the substructure

  The studied substructure includes all the stories of the directly affected part. The indirectly affected part is replaced by horizontal springs, representing the lateral anchorage provided by the rest of the structure.

  2) Equations of the analytical model

  The equations used in the analytical model come from two distinct parts of the frame: the directly affected part (above the lost column) and the indirectly affected part. For these two parts of the structures, equations can be written (compatibility of displacement, elongations, forces equilibrium...). These equations are coupled, representing the coupling between the directly and indirectly affected parts.

  3) Derivation of robustness requirements

  The system of equations allows finding the forces and displacements in the entire structure when the column is completely lost. With these forces and displacements, ductility and resistance conditions are checked to ensure robustness.

- 3D analytical frame model

  The idea of 3D-frame analytical model is the same as for the 2D-case. It is assumed in the 3D case that the two main perpendicular plans are not coupled with each other. Moreover, the frames are assumed to be uncoupled to the other frames parallel to them. Accordingly, it is possible to study a 3D-frame through the study of two 2D-substructures.

- Application of global analytical model to the investigated car park

  The car park designed in the ROBUSTFIRE project (designed within WP5) is examined. The considered car park model is presented as follows:

  – The beams are composite beams
  – There is a reinforced concrete slab "linking" these composite beams

- The exceptional event is a fire occurring next to a supporting column
- There is a bracing system in the two main directions

To apply the global model, the following assumptions are made:

- The column is completely lost and there is no remaining resistance in the column.
- The beneficial effect of the slab is neglected.
- The extremities of the substructure are totally fixed.
- The heated beams just above the lost column are neglected.

The substructure to be studied is only comprised of a single double-beam, at ambient temperature, subject to a force P equal to the total load Q acting on the structure. The complete equations and solving procedure can be found in **Annex C**.

V. References

Demonceau J.-F. (2008), "Steel and composite building frames: sway response under conventional loading and development of membrane effects in beams further to an exceptional action", PhD Thesis realised at the ULg.

EN 1090-2:2008, "Execution of steel structures and aluminium structures, Part 2: Technical requirements for steel structures", 2008.

EN 1992-1-1:2004, "Eurocode 2: Design of concrete structures - Part 1-1: General rules and rules for buildings", European committee for standardization, December 2004.

Fang C., Izzuddin B.A., Elghazouli A.Y., Nethercot D.A., and Obiala R. (2010). "ROBUSTFIRE Internal report - Behaviour of a multi-storey composite car park under a selected real localised fire scenario", Internal Report, Imperial College London.

Fang, C., Izzuddin, B.A., Elghazouli, A.Y., Nethercot, D.A. (2011) "Robustness of Steel-composite Building Structures Subject to Localised Fire". Fire Safety Journal, 46:6, 348-363.

Izzuddin B.A. (1991). "Nonlinear Dynamic Analysis of Framed Structures", PhD Thesis, Imperial College, University of London.

Izzuddin B.A., Vlassis A.G., Elghazouli A.Y. and Nethercot D.A. (2008). "Progressive Collapse of Multi-Storey Buildings due to Sudden Column Loss – Part I: Simplified Assessment Framework", Engineering Structures, 30:5, 1308-1318.

Lemaire F. (2010), "Etude du comportement 3D de structures en acier ou mixtes lors de la perte d'une colonne", Master Thesis realised at the ULg.

Luu N.N.H. (2009), "Structural response of steel and composite building frames further to an impact leading to the loss of a column", PhD Thesis realised at the ULg.

Malvern L.E. (1969). "Introduction to the mecanics of a continuous medium", Englewood Cliffs, NJ: Prentice-Hall.

Omer E., Izzuddin B.A., and Elghazouli A.Y. (2010). "Failure of Unrestrained Lightly Reinforced Concrete Slabs under Fire, Part II: Verification and Application", Engineering Structures, 32, 2647-2657.

Omer E., Izzuddin B.A., and Elghazouli A.Y. (2010). "Failure of Unrestrained Lightly Reinforced Concrete Slabs under Fire, Part I: Analytical Models", Engineering Structures, 32, 2631-2646.

SAFIR. Franssen J. M. (2005). "A Thermal/Structural Program Modelling Structures under Fire", Engineering Journal, AISC, 42:3, 143-158, http://hdl.handle.net/2268/2928.

Vlassis A.G., Izzuddin B.A., Elghazouli A.Y. and Nethercot D.A. (2008). "Progressive Collapse of Multi-Storey Buildings due to Sudden Column Loss – Part II: Application", Engineering Structures, 30:5, 1424-1438.

ANNEX A

Faculté des Sciences Appliquées
Département ArGenCo
Secteur MS²F (mécaniques des solides, des fluides et des structures)
Dr. Ir. J.P. JASPART, Professeur
Ir. J.F. DEMONCEAU, Assistant

Liège, the 14th of March 2012

Robustfire project

3D behaviour of slabs further to a column loss
–
Liège University

Authors:
L. Comeliau
J.-F. Demonceau
C. Huvelle
J.-F. Jaspart

I. 3D behaviour of slabs further to a column loss 3
I.1. Introduction 3
I.2. Influence of boundary conditions 3
I.3. Presentation of existing models for totally unrestrained slabs 6
I.4. Unrestrained slab simplified model with full-depth crack in the centre of the slab (CM) 9
I.4.1. $q - Uc$ curve 9
I.4.2. Failure criteria 12
I.5. Unrestrained slab simplified model with full-depth cracks at the intersection of the diagonal yield lines (IM) 13
I.5.1. $q - Uc$ curve 13
I.5.2. Failure criteria 14
I.6. Solving procedure 14
II. References 15

I. 3D behaviour of slabs further to a column loss

I.1. Introduction

In this part, it will be assumed that a localised fire occurring near a supporting column just below a composite slab will lead to the total loss of this supporting column, the inefficiency of the beams (primary and secondary) and the inefficiency of the steel profile of the composite slab. Also, it is assumed that the unidirectional concrete ribs of the composite slabs are not significantly influencing the behaviour of the slab when significant membrane effects are developing i.e. it is assumed that only the upper part of the slab is contributing to the slab resistance.

Accordingly, the behaviour of the composite slab can be investigated through the study of a 3D uniform slab, submitted to the loss of one of its supporting column, assuming that this slab remains at ambient temperature. The objective is to investigate if the response of the slab further to its support loss can be predicted through analytical methods, taking into account the membrane effects.

In a first step, a parametrical numerical study has been conducted to investigate the influence of the boundary conditions on the slab behaviour. Then, in a second step, the applicability of existing analytical methods to predict the behaviour of the slab under the considered scenario has been investigated.

I.2. Influence of boundary conditions

In [3], a preliminary study has been conducted to investigate the effect of the boundary conditions of a slab on the development of membrane forces in case of a column loss (see Figure 1). In total, four slab configurations have been investigated:

	Horizontally unrestrained edges	Horizontally restrained edges
No rotational restraints	CASE 1	CASE 2
Rotational restraints	CASE 3	CASE 4

For CASE 1, the development of significant membrane forces at the middle of the concrete slab is observed (see Figure 2 – tensile stresses in red, compression stresses in blue). In parallel, a compression ring is developing on the slab borders to equilibrate the tensile forces.

For CASE 2 (Figure 3), a different behaviour is observed. Indeed, as the borders of the slab are horizontally restraints, the membrane forces developing at the middle of the slab are directly anchored on the slab borders and the development of a compression ring is not observed.

For CASE 3 and CASE 4 (Figure 4 and Figure 5), a similar behaviour to the one observed for CASE 1 is identified. It appears that, when the slab boundaries are fully rigid in rotation, there is no influence of the horizontal support conditions. Indeed, as confirmed in Figure 6, the curves representing the evolution of the vertical displacement at the middle of the slab according to the applied load Q are identical for CASE 3 and CASE 4.

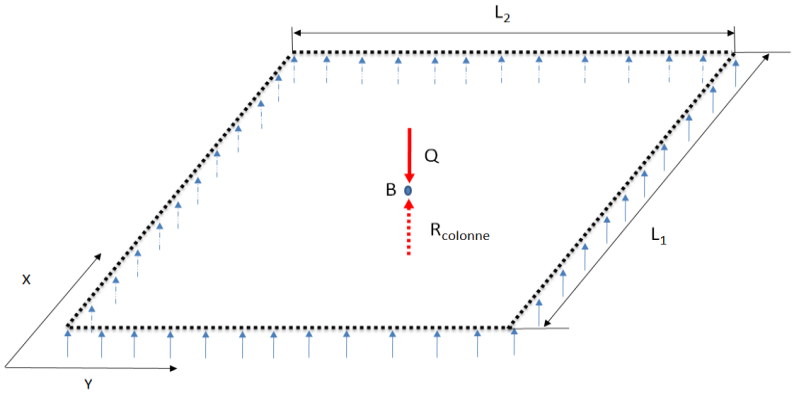

Figure 1. Investigated slab further to a column loss

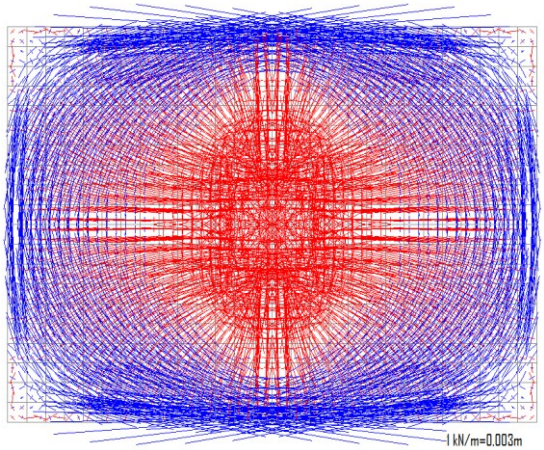

Figure 2. CASE 1 – Distribution of the axial stresses in the plane of the concrete slab

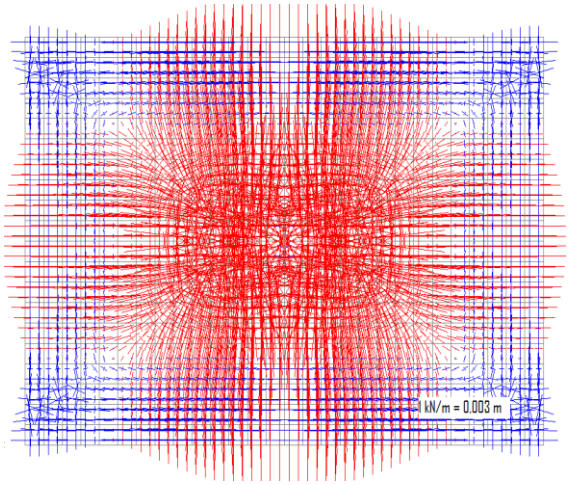

Figure 3. CASE 2 – Distribution of the axial stresses in the plane of the concrete slab

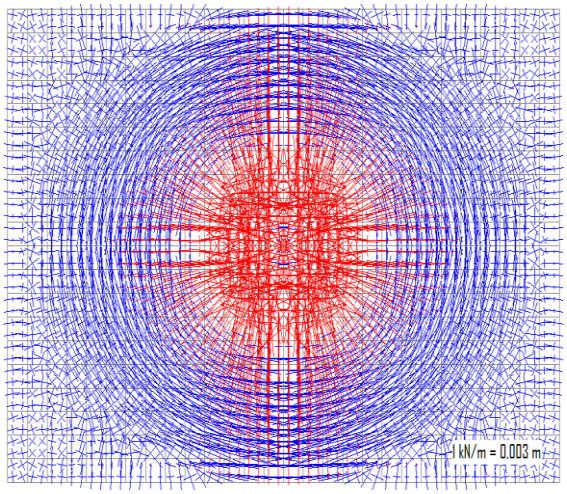

Figure 4. CASE 3 – Distribution of the axial stresses in the plane of the concrete slab

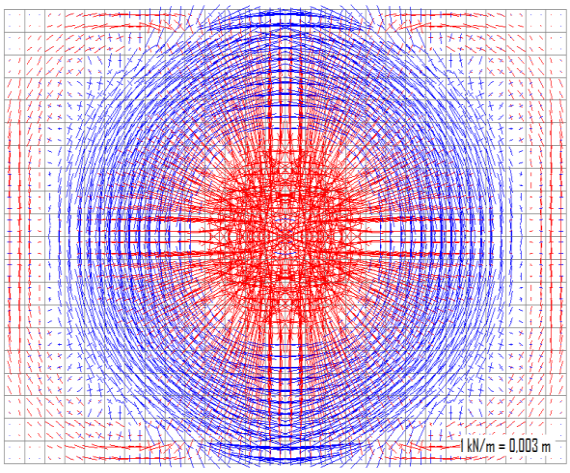

Figure 5. CASE 4 – Distribution of the axial stresses in the plane of the concrete slab

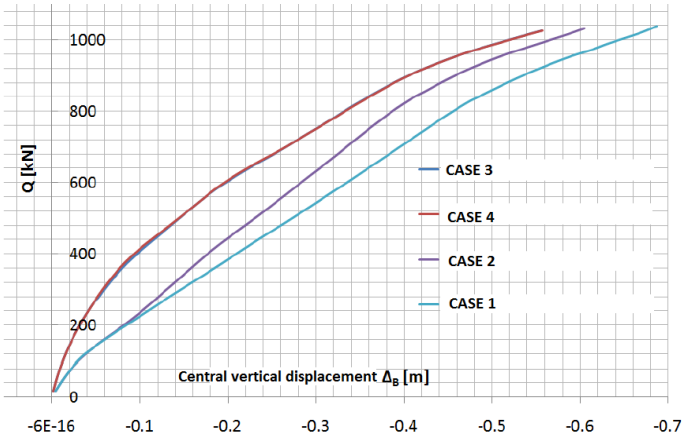

Figure 6. Results for different boundary conditions

For the 4 cases, it has been observed that significant tension forces developed in the center of the slab, while a compression ring was forming on the slab borders, to equilibrate the central membrane forces. As can be seen in Figure 6, the most critical case is case 1, which is the case for which the slab is less restrained.

So, the case that has been studied analytically is case 1. The analytical models which will be used come from the article "Failure of unrestrained lightly reinforced concrete slabs under fire, Part 1: Analytical Models", by E. Omer, B.A. Izzudin, A.Y. Elghazouli (**[1]**)

I.3. Presentation of existing models for totally unrestrained slabs

The simplified ambient temperature models developed by B.A. Izzudin, A.Y. Elghazouli and E.Omer (article "Failure of unrestrained lightly reinforced concrete slabs under fire, Part 1: Analytical Models", by E. Omer, B.A. Izzudin, A.Y. Elghazouli ([1])) are presented within the present section.

In [1], the studied slab is assumed to be loaded by a uniformly distributed load. The models are kinematic models. They are based on the assumption of the development of a yield line mechanism, followed by the development of membrane forces and the occurrence of full depth cracks in the slab. In [1], it is assumed that the yield line mechanism occurring in slabs submitted to uniformly distributed load is the following (Figure 7):

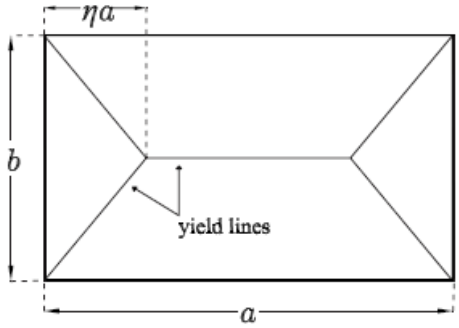

Figure 7. Yield line plastic mechanism in uniformly loaded slabs (**[1]**)

With $\eta = \frac{1}{2\alpha^2}\left(\sqrt{3\alpha^2+1}-1\right)$ and $\alpha = \frac{a}{b}$. For recall, the slab edges are simply supported, there are no rotational restraints. The load leading to this plastic mechanism is given by:

$$q = \frac{12M_p}{ab(3-2\eta)}.\frac{1+2\eta\alpha^2}{\eta\alpha} \quad (1)$$

The M_p in Equation (1) corresponds to sagging resistant moment.

When the plastic mechanism is formed, the stress in the reinforcement crossing the yield lines is equal to f_y. It is assumed that the elastic deformation of the slab can be neglected towards the deformation occurring after the development of this plastic mechanism.

Once the plastic mechanism is formed, the parts of the slab, delimited by the yield lines, are assumed to rotate rigidly around their support and the yield lines. These rigid parts are linked to each other by the reinforcement that stretches out, according to a rigid-strain hardening law material. The failure is defined as the moment when the stress in the reinforcement reaches the ultimate strength of the steel.

The kinematic models take into account the strain concentration in the reinforcement that links the rigid parts of the slab. This strain concentration is influenced by the bond-slip strength σ_b: if the latter is big, then the bond length l_b will be very short and the strain concentration will be important.

The kinematic model to be considered depends on the support conditions:

For slabs with horizontal restraints:

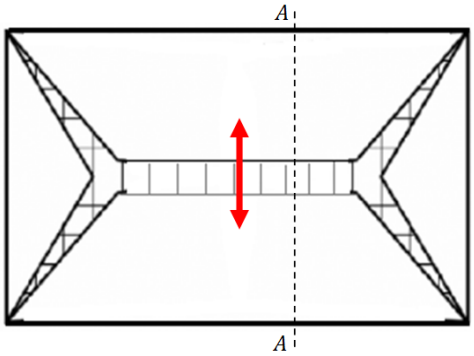

Figure 8. Ruin mechanism for horizontally restrained slabs

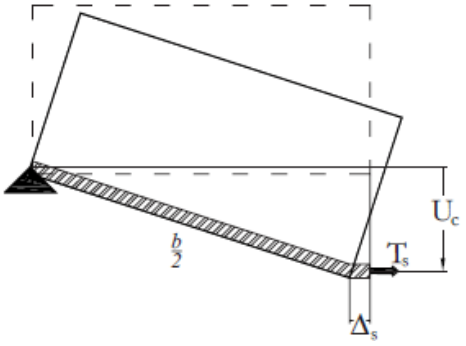

Figure 9. Section A-A in Figure 8 (**[1]**)

Full depth crack parallel to the long span of the slab (Figure 8). Rupture occurs when the reinforcement across the longitudinal yield line reaches the ultimate strength of the rebar.

For horizontally unrestrained slabs:

2 configurations are possible for the position of the full depth cracks, parallel to the shorter span of the slab (Figure 10).

CM model IM model

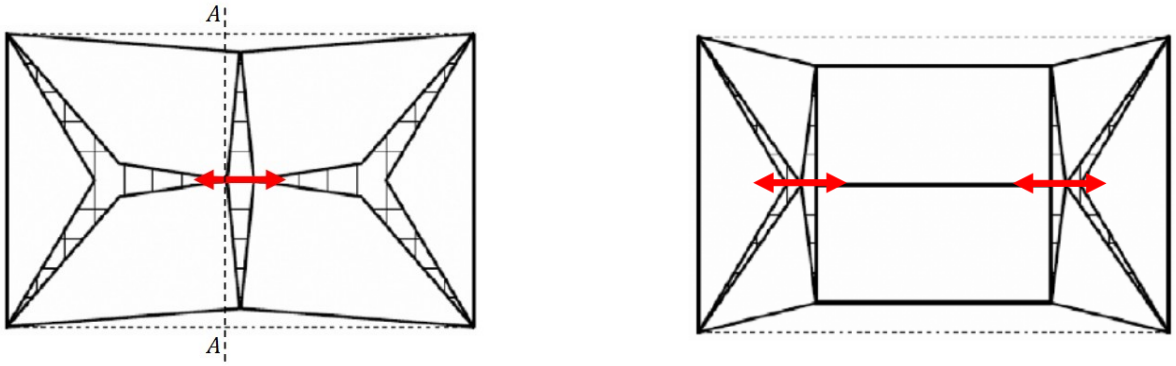

Figure 10. Ruin mechanisms for horizontally unrestrained slabs (**[1]**)

When the full depth-crack occurs in the centre of the slab, the denomination "CM" will be used. When the full depth cracks occur at the intersection of the diagonal yield lines, the denomination "IM" will be used. Rupture occurs when the reinforcement across the full depth crack (in the centre or at the intersection of the yield lines) reaches the ultimate strength of steel.

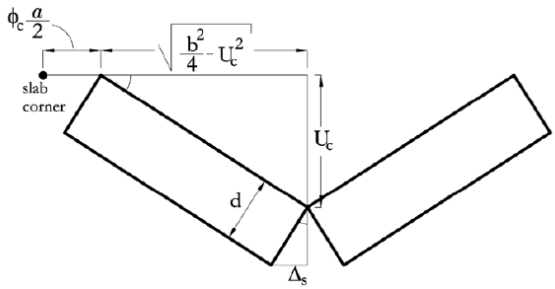

Figure 11. Section A-A in Figure 10 (**[1]**)

For recall, it is assumed that the slab is horizontally unrestrained, so the crack pattern will be one of the two given in Figure 10, and Figure 8 is only given for information.

As the concrete is assumed to be fully rigid in compression, all the internal energy $\dot{D}$ is dissipated through the elongation of the rebar across the cracks. These elongations Δ_s depend on the vertical displacement in the centre of the slab, U_c , by compatibility of displacements:

$$\dot{D} = f(\Delta_s) = f(\Delta_s = g(U_c))$$

On the other hand, the external work depends on the uniformly distributed load q:

$$\dot{E} = f(q) = \frac{qab(3-2\eta)}{24}$$

Finally, the link between U_c and q is established by writing the equality between the internal and the external dissipated energy:

$$\dot{D} = \dot{E}$$

To summarize, the mains assumptions of these models are listed here below:

- Slab submitted to uniformly distributed load
- Uniform slab
- Single layer of reinforcement
- Orthotropic reinforcement (layers in the two directions assumed at the same level)
- Rigid-strain hardening material model for steel (Figure 12)

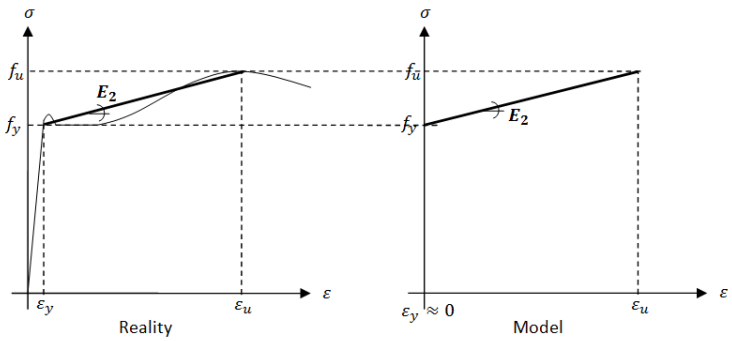

Figure 12. Law material for steel

- Negligible concrete tensile strength
- Concrete fully rigid in compression
- Bond-slip response described by a rigid-plastic law (Figure 13)

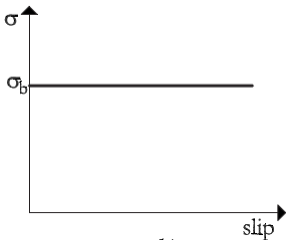

Figure 13. Bond-slip response (**[1]**)

I.4. Unrestrained slab simplified model with full-depth crack in the centre of the slab (CM)

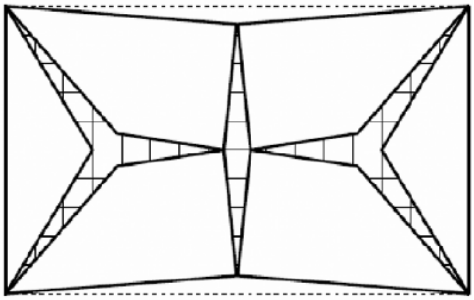

Figure 14. CM model (**[1]**)

The first developed method will be for the case where the full depth crack occurs in the centre of the slab.

I.4.1. $q - U_c$ curve

q $[kN/m^2]$ is the uniformly distributed load acting on the slab and U_c $[m]$ is the vertical displacement in the centre of the slab.

- Definition of the parameters

Table 1. Models parameters

Symbol	Units	Meaning
$\boldsymbol{a}$	m	Long span of the slab
$\boldsymbol{b}$	m	Short span of the slab
α	$-$	Aspect ratio $\alpha = \frac{a}{b} > 1$
η	$-$	Plastic mechanism parameter $\eta = \frac{1}{2\alpha^2}\left(\sqrt{3\alpha^2+1}-1\right)$
$\boldsymbol{d}$	m	Effective thickness of the slab
$\boldsymbol{A_s}$	m^2/m	Steel area per unit width of the slab $(A_{sx} = A_{sy} = A_s)$
$\boldsymbol{f_y}$	N/m^2	Yield strength of the reinforcement
$\boldsymbol{f_u}$	N/m^2	Ultimate strength of the reinforcement
T_y	N/m	$T_y = A_s * f_y$
T_u	N/m	$T_u = A_s * f_u$
$\boldsymbol{E_2}$	N/m^2	Hardening modulus of the reinforcement
$\boldsymbol{\sigma_b}$	N/m^2	Bond strength per unit width per unit length of slab
ε_u	$-$	Ultimate strain of the reinforcement $\varepsilon_u = \frac{f_u - f_y}{E_2}$
$\boldsymbol{f_c}$	N/m^2	Compression strength of the concrete

The symbols in bold characters in Table 1 are the input data of the analytical model.

- Elongations

$$\Delta_{sce}^{C} = \frac{2dU_c}{b} + \frac{U_c^2(1-2\eta)}{2b}$$
$$\Delta_{sdy}^{C} = \frac{2dU_c}{b} + \frac{U_c^2(1-2\eta)}{2b}$$
$$\Delta_{sdx}^{C} = \frac{dU_c}{\eta a} + \frac{U_c^2(1-2\eta)}{4\eta a}$$
$$\Delta_{scr}^{C} = \frac{U_c^2}{2a}$$

The indexes "ce", "dy, "dx" and "cr" are relative to the different cracks and the orientation of the considered elongations, as illustrated in Figure 15:

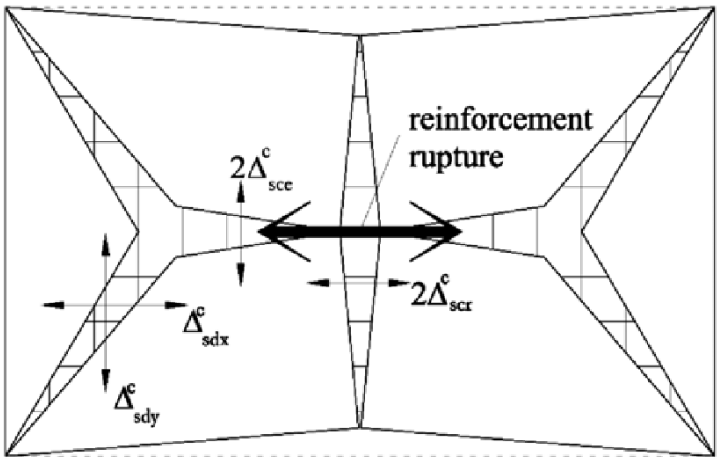

Figure 15. Cracks in CM model (**[1]**)

- Forces in the rebar

$$T_{sce}^{C} = T_y + \sqrt{2A_s E_2 \sigma_b \Delta_{sce}^{C}}$$
$$T_{sy}^{C} = T_y + \sqrt{A_s E_2 \sigma_b \Delta_{sdy}^{C}}$$
$$T_{sx}^{C} = T_y + \sqrt{A_s E_2 \sigma_b \Delta_{sdx}^{C}}$$
$$T_{scr}^{C} = T_y + \sqrt{2A_s E_2 \sigma_b \Delta_{scr}^{C}}$$

- Relation between q and U_c

$$q = 12\frac{\left[T_{sce}^{C}(1-2\eta)\alpha + 2T_{sy}^{C}\eta\alpha + \frac{T_{sx}^{C}}{2\eta\alpha}\right][2d + (1-2\eta)U_c] + T_{scr}^{C}\frac{U_c}{\alpha}}{ab(3-2\eta)}$$

So, for a given value of U_c, the reinforcement elongations Δ_s can be found, and so the efforts in the rebar T_s, and finally, the value of q corresponding to considered value of U_c. That's how the curve $q - U_c$ can be plot.

- Additional information

Value of d

To know where the $q - U_c$ curve starts:

$$U_c = 0$$

$$\rightarrow \Delta_{sce}^{C} = \Delta_{sdy}^{C} = \Delta_{sdx}^{C} = \Delta_{scr}^{C} = 0$$

$$\rightarrow T_{sce}^{C} = T_{sy}^{C} = T_{sx}^{C} = T_{scr}^{C} = T_y$$

$$\rightarrow q = 12.\frac{\left[T_y(1-2\eta)\alpha + 2T_y\eta\alpha + \frac{T_y}{2\eta\alpha}\right]2d}{ab(3-2\eta)} = \frac{24T_y d}{ab(3-2\eta)}\left[\alpha - 2\alpha\eta + 2\eta\alpha + \frac{1}{2\eta\alpha}\right]$$

$$q = \frac{24T_y d}{ab(3-2\eta)}.\frac{2\eta\alpha^2+1}{2\eta\alpha} = \frac{12T_y d}{ab(3-2\eta)}.\frac{1+2\eta\alpha^2}{\eta\alpha}$$

If this formula is compared with the Equation (1), it can be seen that the analytical method considers $M_{pl} = T_y * d$, which is a simplification.

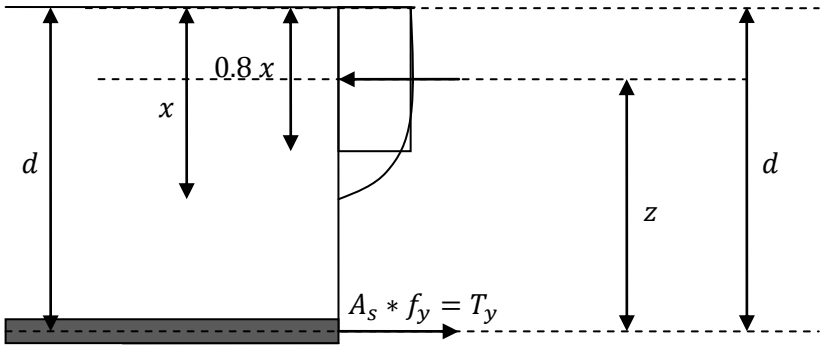

Figure 16. Definition of d

Indeed, in reality, $M_{pl} = T_y * z$ with $z = d - 0.4x$. So, in reality, $M_{pl} = T_y * d * \left(1 - 0.4 * \frac{x}{d}\right)$.

Here, the ductility of this reinforced concrete cross section must be taken into account. Referring to the EC2, §5.6.2 (2):

> *The required ductility may be deemed to be satisfied without explicit verification if all the following are fulfilled:*
>
> *i. the area of tensile reinforcement is limited such that, at any section*
> $x_u/d \leq 0{,}25$ *for concrete strength classes ≤ C50/60*
> $x_u/d \leq 0{,}15$ *for concrete strength classes ≥ C55/67*
>
> *ii. reinforcing steel is either Class B or C*
>
> *iii. the ratio of the moments at intermediate supports to the moments in the span should be between 0,5 and 2*

So, as the value of x/d cannot exceed the value of 0.25, the term $\left(1 - 0.4 * \frac{x}{d}\right)$ varies between 1 (for $x \rightarrow 0$) and $0.9 = 1 - 0.4 * 0.25$. Accordingly, the relative error when considering $T_y * z$ or $T_y * d$ for M_{pl} is 10% maximum.

So, for the value of d, it appears to be reasonable to take the distance between the rebar and the upper fibre of the slab.

Value of $f_y, f_u, E_2, \varepsilon_u$

These characteristics depend on the type of steel that is considered in the project. In EC2, Annex C, the Table 2 can be found:

Table 2. Properties of reinforcement

Product form	Bars and de-coiled rods			Wire Fabrics			Requirement or quantile value (%)
Class	A	B	C	A	B	C	-
Characteristic yield strength f_{yk} or $f_{0,2k}$ (MPa)	400 to 600						5,0
Minimum value of $k = (f_t/f_y)_k$	≥1,05	≥1,08	≥1,15 <1,35	≥1,05	≥1,08	≥1,15 <1,35	10,0
Characteristic strain at maximum force, ε_{uk} (%)	≥2,5	≥5,0	≥7,5	≥2,5	≥5,0	≥7,5	10,0
Bendability	Bend/Rebend test			-			
Shear strength	-			0,3 $A f_{yk}$ (A is area of wire)			Minimum
Maximum deviation from nominal mass (individual bar or wire) (%) — Nominal bar size (mm) ≤ 8	± 6,0						5,0
Maximum deviation from nominal mass (individual bar or wire) (%) — Nominal bar size (mm) > 8	± 4,5						

Referring to ductility conditions given previously, class A steel cannot be considered.

Value of σ_b

In §8.4.2 of EC2, the following formula can be found:

$$f_{bd} = 2.25 * \eta_1 * \eta_2 * f_{ct}$$

With :

- f_{ct} is the concrete tensile strength according to §3.1.6 of EC2
- η_1 : related to the quality of the bond condition
- η_2 : related to the bar diameter

f_{bd} is the bond strength per unit reinforcement surface area. So, to get the value of σ_b, the bond strength per unit width per unit length of slab, f_{bd}has to be multiplied by P, which is the rebar "perimeter" per unit width. If e is the spacing of the rebar (in mm) and Φ their diameter (also in mm), then $P = \frac{1}{e} * \pi\Phi\ [mm/mm]$ and $\sigma_b = P * f_{bd}$.

I.4.2. Failure criteria

For recall, failure happens when the reinforcement crossing the cracks reaches its ultimate strength f_u. So, the deflection at failure U_{fc} is given by:

$$U_{fc}^{C} = \max\begin{cases} U_{fc1} = \begin{cases} \sqrt{\dfrac{a}{2A_sE_2\sigma_b}}(T_u - T_y) & if\ \dfrac{T_u - T_y}{\sigma_b} \le \dfrac{a}{4}(1-2\eta) \\ \dfrac{a(1-2\eta)}{2\sqrt{A_sE_2}}\sqrt{\dfrac{T_u - T_y}{1-2\eta} - \dfrac{\sigma_b a}{8}} & if\ \dfrac{T_u - T_y}{\sigma_b} \ge \dfrac{a}{4}(1-2\eta) \end{cases} \\ U_{fc2} = \sqrt{d^2 + \dfrac{\eta\alpha(T_u - T_y)^2}{A_sE_2\sigma_b}} - d \end{cases}$$

U_{fc1} is determined considering that the failure occurs in the central through depth crack (Δ_{scr} elongation), while U_{fc2} is determined by considering the rebar elongation Δ_{sdx} in addition to Δ_{scr}.

I.5. Unrestrained slab simplified model with full-depth cracks at the intersection of the diagonal yield lines (IM)

The case when the full depth cracks occur at the intersections of the diagonal yield-lines will be studied in this part. The parameters in the model are the same as described before.

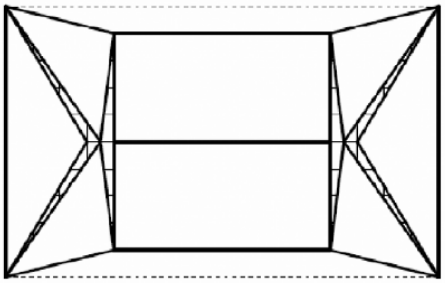

Figure 17. IM model (**[1]**)

I.5.1. $q - U_c$ curve

- Elongations

$$\Delta_{sce}^{I} = \frac{2dU_c}{b}$$
$$\Delta_{sdy}^{I} = \frac{2dU_c}{b}$$
$$\Delta_{sdx}^{I} = \frac{dU_c}{\eta a}$$
$$\Delta_{scr}^{I} = \frac{U_c^2}{4\eta a}$$

- Forces in the rebar

$$T_{sce}^{I} = T_y + \sqrt{2A_s E_2 \sigma_b \Delta_{sce}^{I}}$$
$$T_{sy}^{I} = T_y + \sqrt{A_s E_2 \sigma_b \Delta_{sdy}^{I}}$$
$$T_{sx}^{I} = T_y + \sqrt{A_s E_2 \sigma_b \Delta_{sdx}^{I}}$$
$$T_{scr}^{I} = T_y + \sqrt{A_s E_2 \sigma_b \Delta_{scr}^{I}}$$

- Relation between q and U_c

$$q = 24\frac{T_{sce}^{I}(1-2\eta)\alpha d + 2T_{sy}^{I}\eta\alpha d + \frac{T_{sx}^{I} d}{2\eta\alpha} + T_{scr}^{I}\frac{U_c}{4\eta\alpha}}{ab(3-2\eta)}$$

I.5.2. Failure criteria

$$U_{fc} = \sqrt{d^2 + \frac{\eta a (1-2\eta)^2}{4 A_s E_2 \sigma_b} \Gamma_{ia}} - d$$

With

$$\Gamma_{ia} = \begin{cases} 8\left(\frac{T_u - T_y}{1-2\eta}\right)^2 & if \quad \frac{T_u - T_y}{\sigma_b} \leq \frac{a}{2}(1-2\eta) \\ \left(\frac{2(T_u - T_y)}{1-2\eta} + \sigma_b a\right)^2 - 2\sigma_b^2 a^2 & if \quad \frac{T_u - T_y}{\sigma_b} \geq \frac{a}{2}(1-2\eta) \end{cases}$$

The failure is relative to the sum of the elongations Δ_{sdx} and Δ_{scr}.

I.6. Solving procedure

For the $q - U_c$ curve

- Choose a value of U_c
- Compute the rebar elongations in the different cracks
- Compute the forces in the rebar
- Compute the value of q corresponding to the chosen value of U_c

For the failure criteria

Compute $U_{c,limit}$ (I.4.2 for CM model, I.5.2 for IM model), and compute the q corresponding, following the procedure here above.

Accordingly, with this procedure, it is possible to predict the maximum deflection capacity of the slab ($U_{c,limit.}$) and its associated load (q_{limit}). Knowing that, it is finally possible to check if the slab is sufficiently resistant by checking if the uniformly applied load q is smaller than q_{limit}.

II. References

[1] Izzudin B.A., Omer E., Elghazouli A.Y. (2010). "Failure of unrestrained lightly reinforced concrete slabs under fire, Part 1: Analytical Models", Engineering Structures.

[2] Omer E., Izzudin B.A., M. ASCE, Elghazouli A.Y., M. ASCE (2009). "Failure of Lightly Reinforced Concrete Floor Slabs with Planar Edge Restraints under Fire", Journal Of Structural Engineering.

[3] Lemaire F. (2010), "Etude du comportement 3D de structures en acier ou mixtes lors de la perte d'une colonne", Master Thesis realised at the ULg.

[4] Six-monthly report of Robustfire project

ANNEX B

ROBUSTFIRE REPORT

Global FEM model and its application on the reference car park

Imperial College London

Cheng fang

Bassam Izzuddin

Ahmed Elghazouli

David Nethercot

ArcelorMittal

Renata Obiala

Contents

I Introduction 3

II Structural configuration 3

III Fire load 5

III.1 Selected fire scenario 5

III.2 Temperature distribution 7

IV Modelling techniques 10

IV.1 Material modelling 10

IV.2 Structural modelling 12

IV.2.1 General 12

IV.2.2 Beam/column modelling 13

IV.2.3 Slab modelling 14

IV.2.4 Joint modelling 15

IV.2.4.1 Identification of active components 16

IV.2.4.2 Joint ductility supply / failure criteria 17

IV.2.4.3 Elevated temperature degradation 21

IV.2.4.4 Creep assessment 23

IV.2.4.5 Example of major axis beam-to-column joint modelling 25

IV.2.4.6 Example of minor axis beam-to-column and beam-to-beam joints modelling 27

V Structural analysis 28

V.1 Response of upper ambient floor 29

V.2 Response of fire affected structural system 31

V.2.1 Fire on floor level 1 32

V.2.2 Fire on floor level 5 35

V.2.3 Fire on floor level 8 38

V.3 Summary of analysis 40

VI References 43

I Introduction

Numerical structural analysis can give a clear and accurate insight into the structural responses of a building subject to fire. This report investigates the behaviour of a multi-storey composite car park subject to a real localised fire near an internal column. In this study, the design of the car park is in accordance with the current UK practice (WP5) and the performance of the structure is predicted based on the detailed heat transfer analysis undertaken by the 'ROBUSTFIRE' project partner ArcelorMittal. Finite element package SAFIR (Franssen, 2005) is employed for the heat transfer analysis, where all the output temperature results are extracted directly and incorporated into the nonlinear FEM program ADAPTIC (Izzuddin, 1991) for structural analysis. Two levels of structural modelling are employed, which are full slab model and grillage model. Hereafter, the structural configuration, the modelling techniques and the associated assumptions are firstly described. This is followed by an elaboration of the temperature distribution obtained by SAFIR. Finally, the structural analysis results from ADAPTIC will be discussed.

II Structural configuration

A typical eight-storey car park designed for the ROBUSTFIRE project is considered as a reference building. A conventional composite steel-concrete construction is selected, where the top floor is also used as a level of parking. IPE 550 and IPE450 beams are used for primary beams and secondary beams respectively for all floors. The plan view structural layout is illustrated in Figure 1.

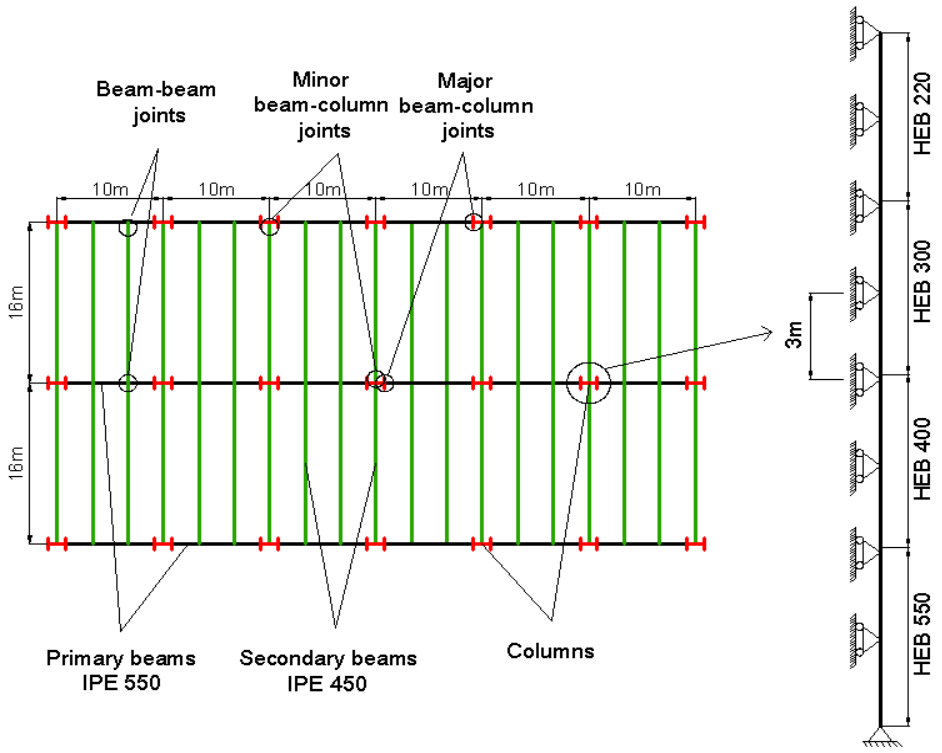

Fig. 1 Structural layout for reference building

The height of each floor is 3 m, which makes a total height of the building equal to 24m. The size of the columns varies at every two floors from the HEB220 for the top two floors to the HEB550 for the bottom two floors (Figure 1). The required lateral resistance is provided by wind-bracings and the concrete ramp on each side of the building. Therefore, lateral movements of the columns can be ignored, and the buckling length of each column can be considered as 3m when they are designed.

Type COFRAPLUS 60 ribbed slab is selected for the composite floor of a 3.333m span, as shown in Figure 2. The floor slab is 120mm deep, and consists of a ribbed metal sheet of 1 mm thickness. This steel deck cannot only act as lower reinforcement in the longitudinal direction of the ribs, but also acts as formwork during the casting of the concrete. A basic mesh of Φ8mm spaced at 200mm (A_s=250mm^2/m) is used in order to limit concrete cracking. To ensure composite action for the major axis beam-to-column joints, additional rebars (10×Φ12mm) are added in order to increase the bending resistance of these joints. Full shear interactions between concrete and steel are assumed for the floor system. All floors are designed to carry the same gravity load, including the roof. The values of the unfactored composite slab self weight and vehicle loads on each floor are 2.145kN/m^2 and 2.5kN/m^2, respectively. So a basic load of 5kN/m^2 is considered in this study.

With respect to the joints, flush end-plate connections are employed for the major axis beam-column joints, and double web-cleat (double angle) connections are adopted for the minor axis beam-column joints as well as for the beam-to-beam joints. These joints are designed in accordance with the current Eurocode guidelines (EN 1993-1-8, 2005). In addition, as far as structural integrity is concerned, the tying force requirements specified in BS 5950: Part 1 (2001) are satisfied. The geometric details of the joints are illustrated in Figure 3.

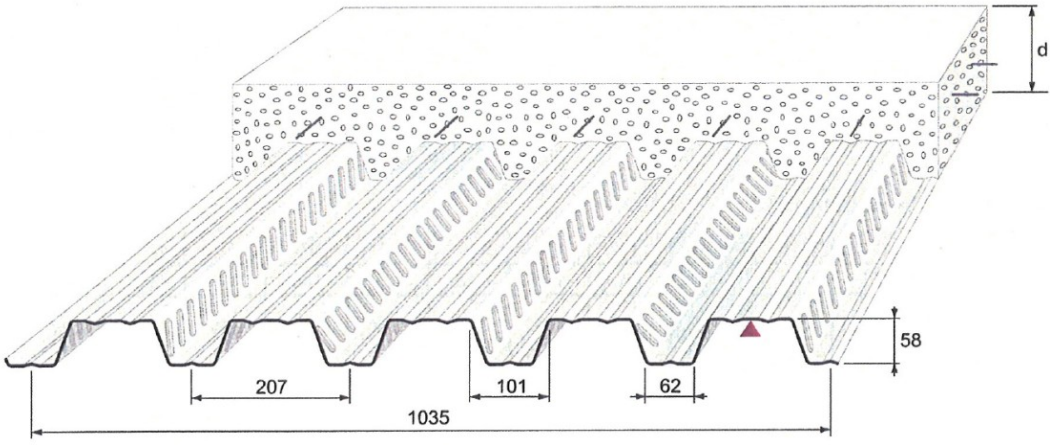

Fig. 2 Geometric configuration of the floor slab type COFRAPLUS 60

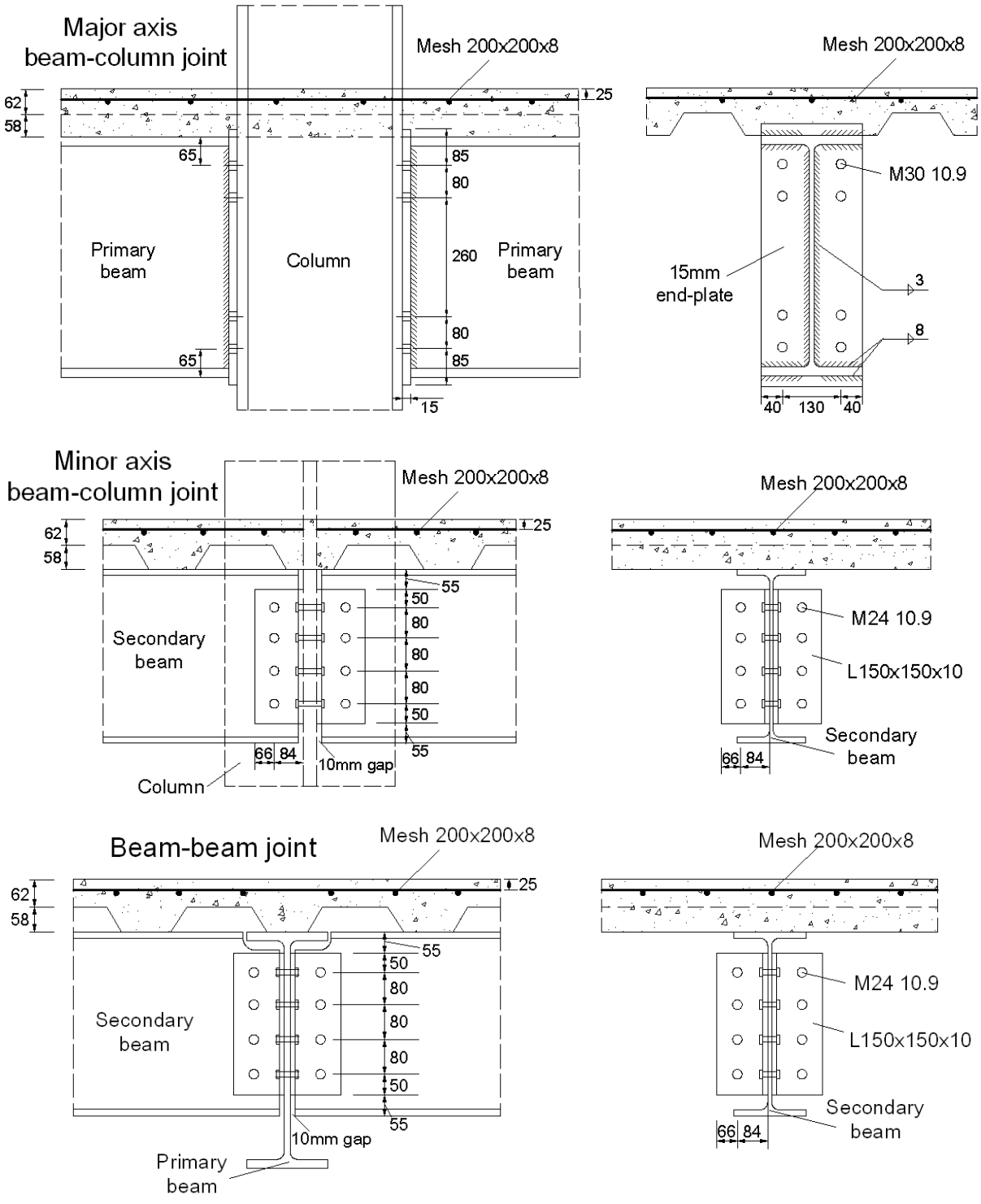

Fig. 3 Geometric configuration of joints

III Fire load

III.1 Selected fire scenario

The selected fire scenario assumes that four V3 class cars are parked around an internal column, and the fires are triggered in the sequence shown in Figure 4. The interval of the fire spreading from one car to another/other car/s is 12 minutes, and

the history of temperature distribution within structural members (e.g. steel beams and composite slab) are captured at 3 minute intervals. The rate of heat release of each burning car is shown in Figure 5, where the maximum heat release rate is 8.3MW. The vertical distance between the fire origins and the ceiling is 2.4m.

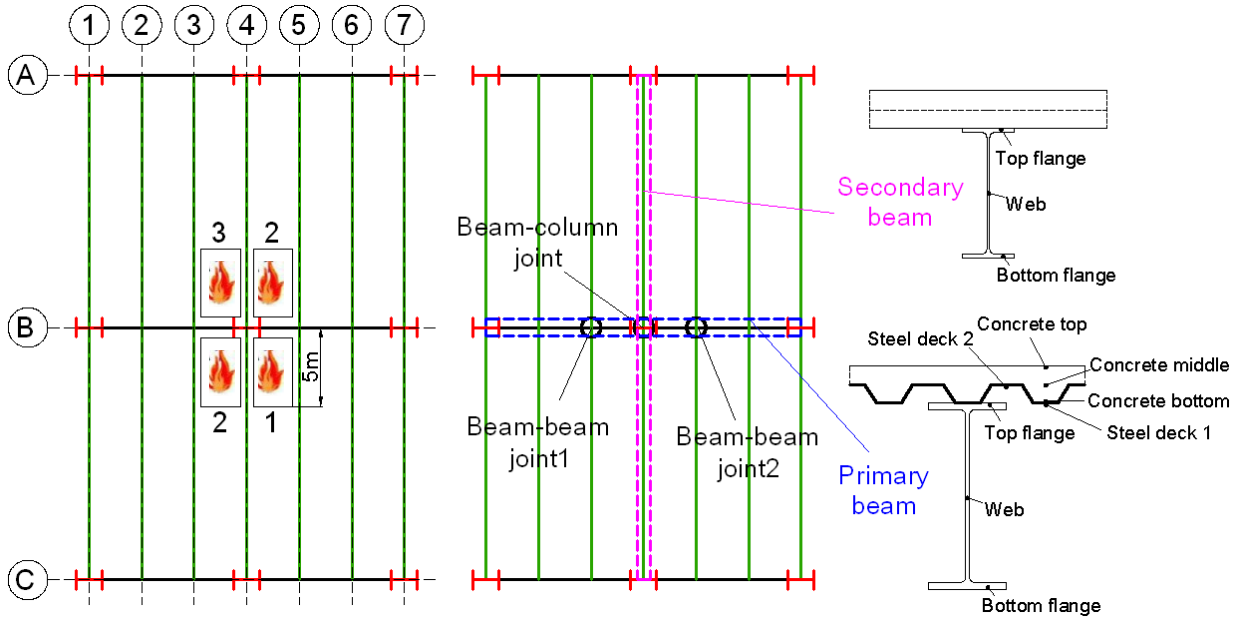

Fig. 4 Illustration of fire scenario

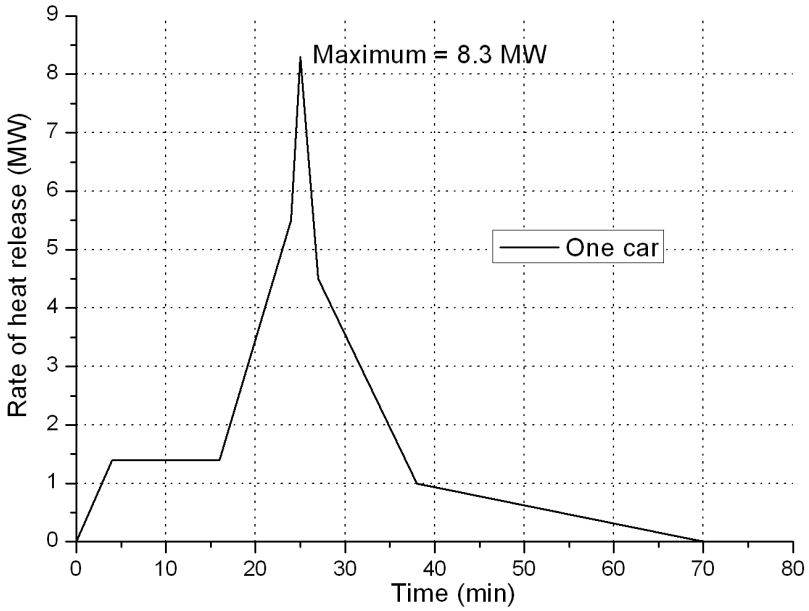

Fig. 5 Rate of heat release for each V3 car

III.2 Temperature distribution

The finite element programme SAFIR is employed to conduct thermal analysis for the car park under the selected fire scenario, as shown in Figure 6. The thermal output data are extracted and input into the finite element model established in ADAPTIC for structural analysis. Here, several temperature distribution results within some principal structural members (outlined in Figure 4) measured from SAFIR are briefly presented and discussed.

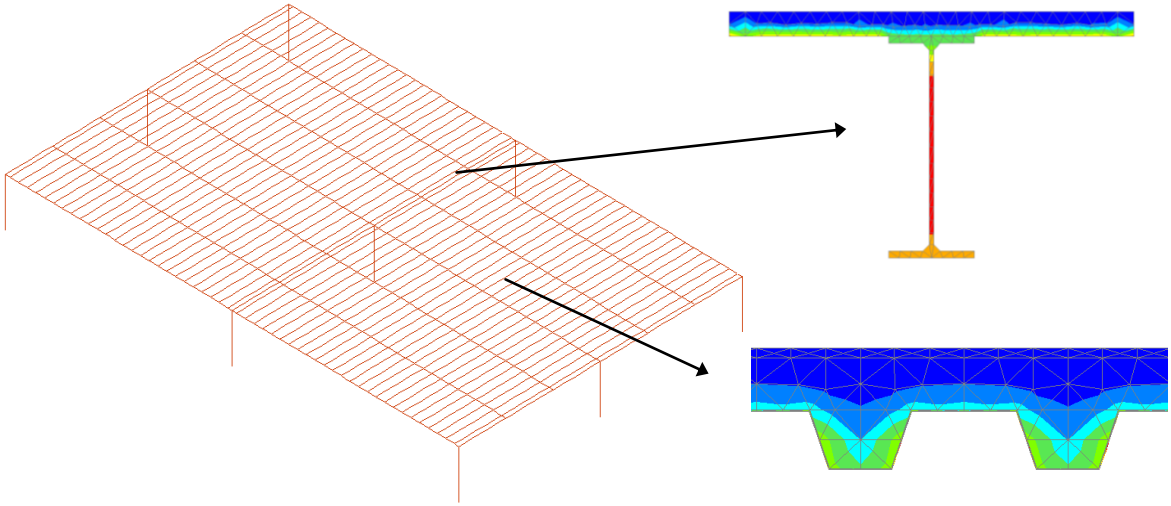

Fig. 6 Illustration of thermal analysis outputs by SAFIR

The temperature-time relationships at the position of the beam-to-column joint and two adjacent beam-to-beam joints ('beam-beam joint 1' and 'beam-beam joint 2' in Figure 4) are shown in Figure 7. An evenly distributed temperature field is assumed within each joint. The temperature within the fire affected column is considered to be identical to the one within the beam-to-column joint. It is observed that the peak temperature within the beam-to-column joint as well as the fire affected column is around 750°C at the time of 30 minutes, which can cause a considerable reduction to the resistance of the fire affected column, joints and slab systems.

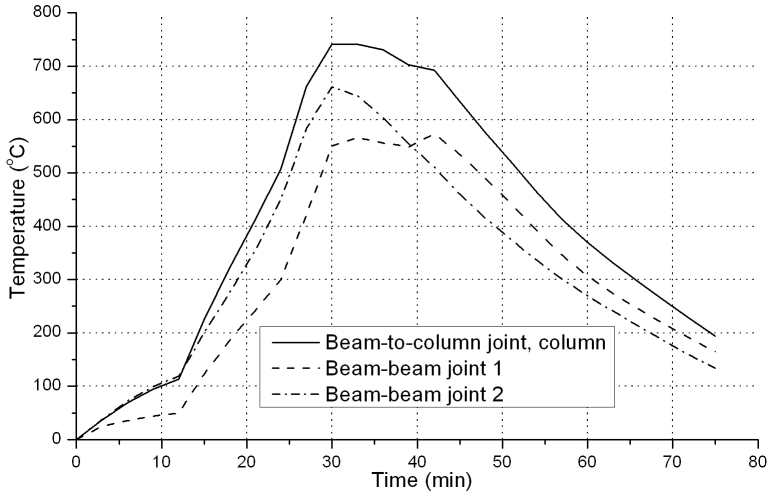

Fig. 7 Temperature-time curves for joints by SAFIR

Figure 8 shows the temperature distributions along the primary beam (identified in Figure 4) obtained by SAFIR, where three points across the cross-section (i.e. top flange, web, and bottom flange) are monitored along the 20m double-span. Based on the results, a peak temperature of approximately 750°C is found in the beam web, and a distinct thermal gradient across the cross-section is identified. Around the peak temperature, the temperatures at the bottom flange and web are considerably higher than that at the top flange, whereas this difference decreases during the cooling phase, during which the temperature distribution tends to be even over the cross-section. Similar trends are observed from the results of the temperature distribution within a selected secondary steel beam, as shown in Figure 9, where the three points across the cross-section are also captured along the 32m double-span. The peak temperature found within the secondary beam is around 920°C in the web. Furthermore, for both primary and secondary beams, high temperatures are only observed within parts of the beam length in the vicinity of the fire origins, whereas for adjacent beam parts which are not immediately above the fire origins, the temperature decreases rapidly to room temperature. This indicates that the fire affected area is rather localised, and the surrounding structural members can be seen at ambient temperature.

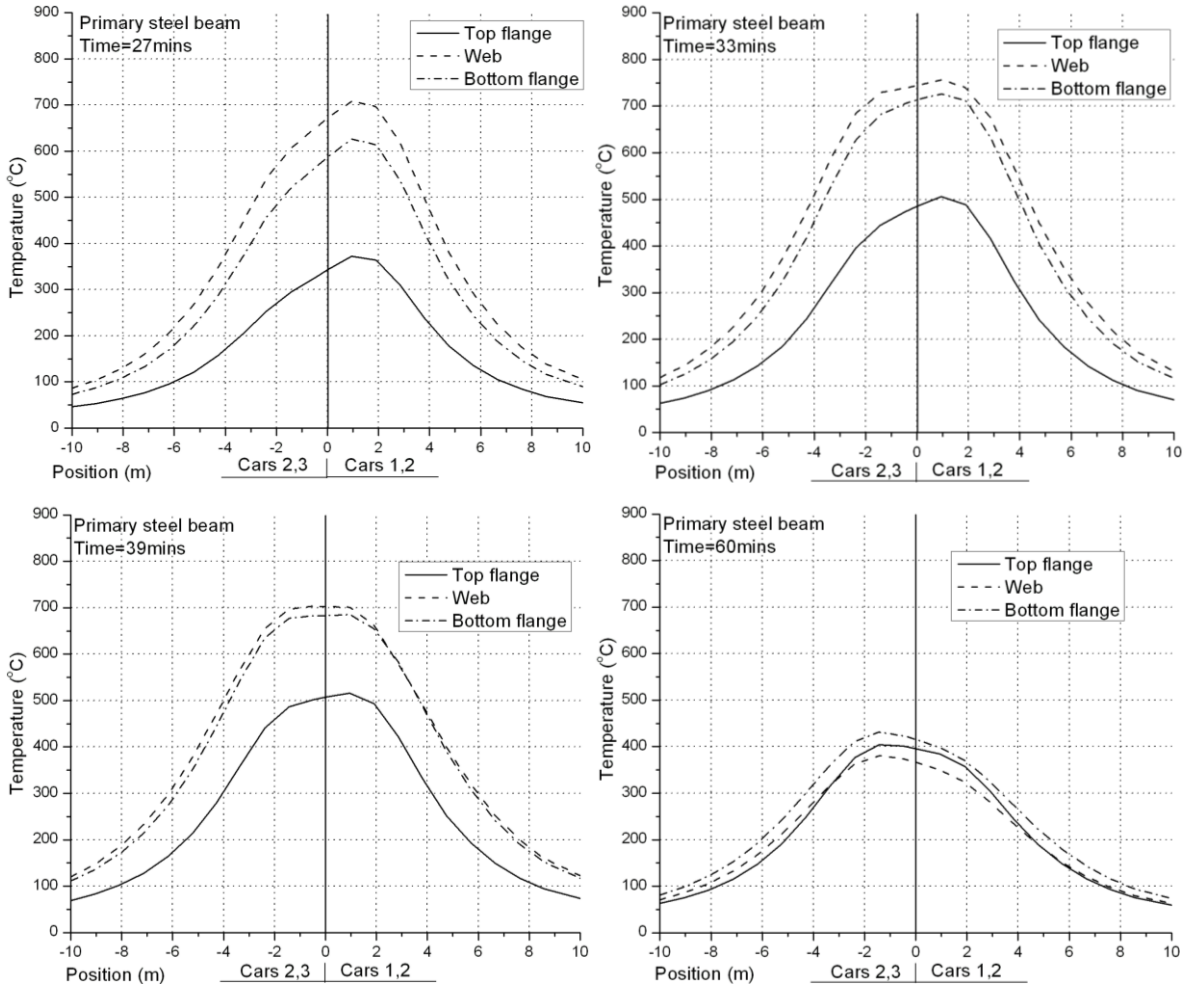

Fig.8 Temperature distribution within primary steel beam by SAFIR

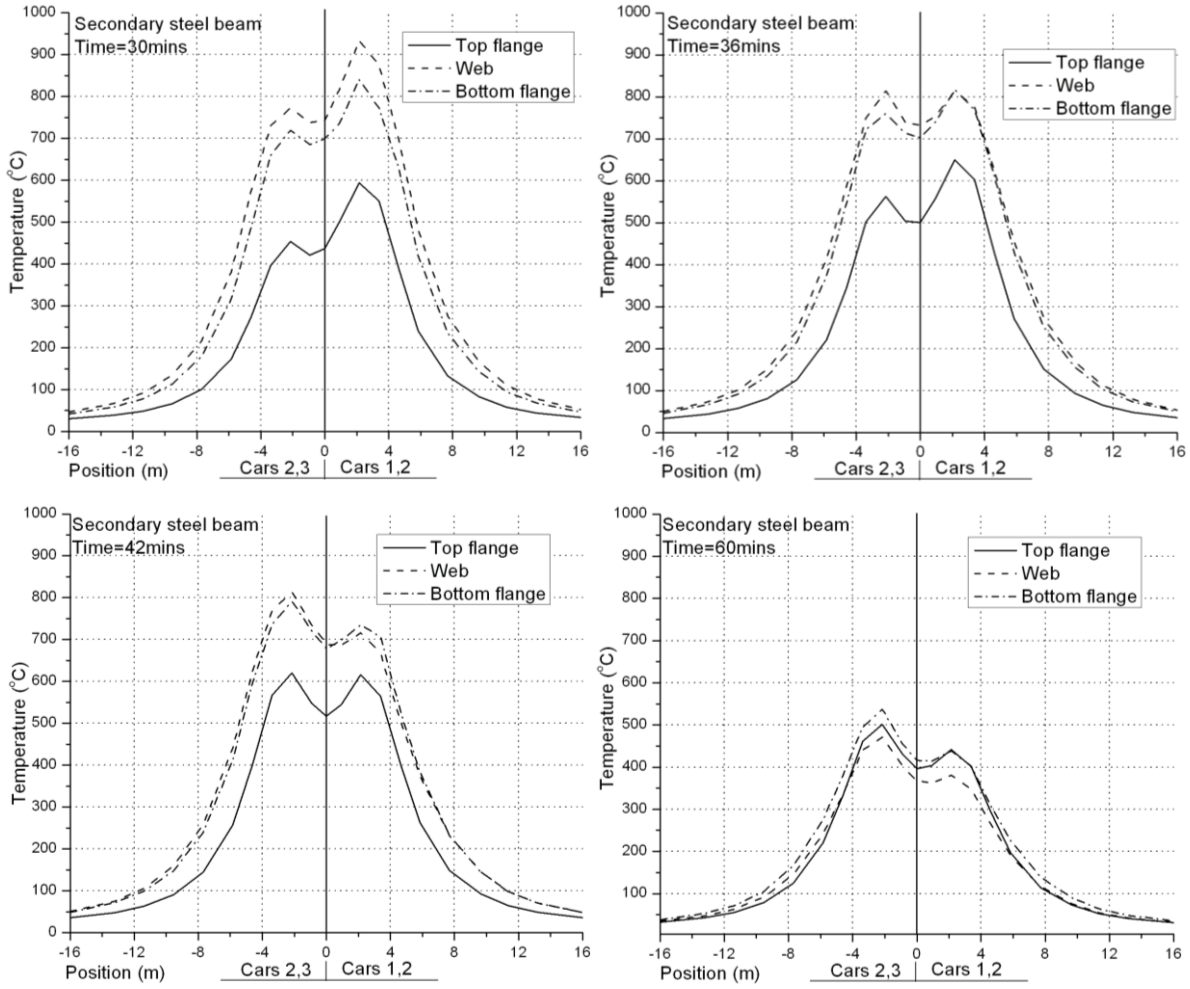

Fig.9 Temperature distribution within secondary steel beam (supported by columns) by SAFIR

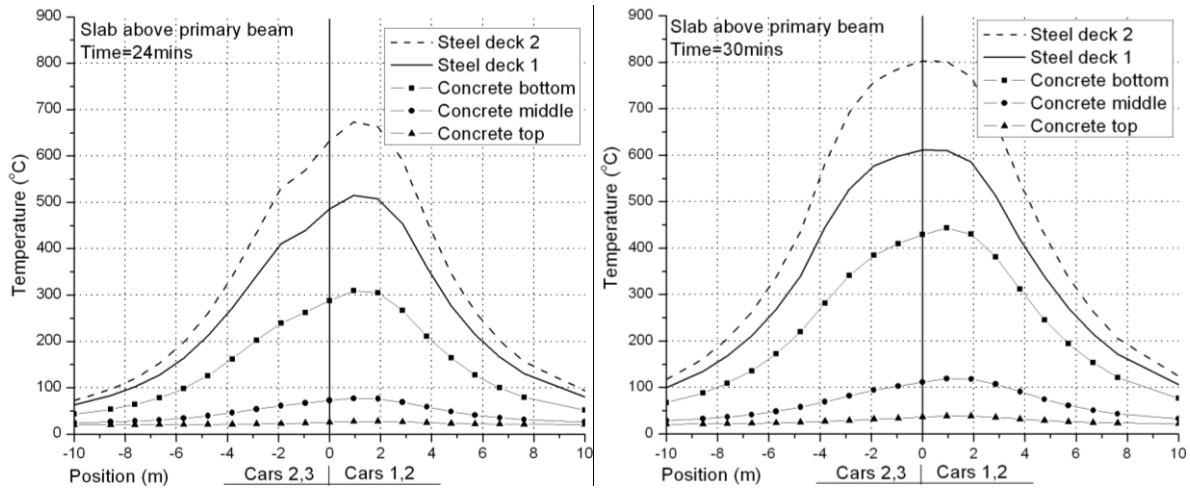

Fig.10 Temperature distribution within concrete slab above primary beam by SAFIR (Cont…)

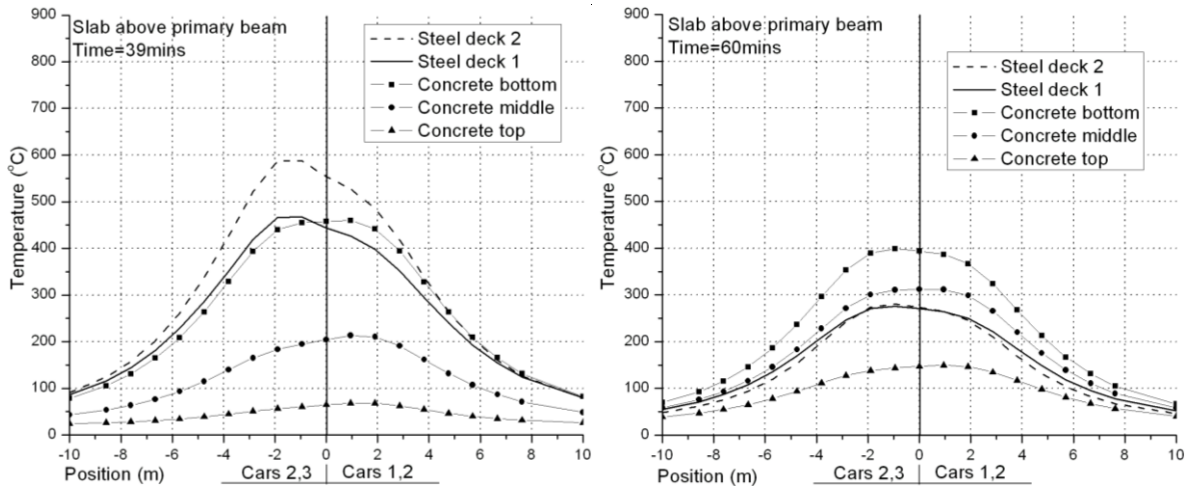

Fig.10 (…Cont) Temperature distribution within concrete slab above primary beam by SAFIR

Figure 10 provides the temperature distributions within the concrete slab above the primary beam, as identified in Figure 4, where five points over the cross-section of the ribbed slab (i.e. steel deck 1, steel deck 2, concrete top, concrete middle, and concrete bottom) are captured along the 20m double-span. It is observed that during the heating phase, the temperature in the steel deck is much higher than in the concrete, even for the concrete immediately above the steel deck. The temperature decreases further towards the top of the slab which is almost under room temperature. During the cooling phase, a faster temperature decreasing rate is found in the steel deck than in the concrete, thus reducing the thermal gradient over the cross-section. Also, high temperatures are only observed within the slab near the fire origins, while the surrounding part of the slab remains under a much lower temperature.

IV Modelling techniques

IV.1 Material modelling

For the reference building, different steel grades are employed for beams, steel decks, columns, and reinforcement bars. The ambient steel properties for the structural members are given in Table 1. In ADAPTIC, a linear-elliptic material model is used for steel under ambient and elevated temperature conditions (EN1993-1-2, 2005). The material degradations (i.e. yield strength f_y, proportional limit f_p, and the elastic modulus E) and the thermal strain of steel induced by temperature elevation are based on the relative recommendation specified in EN1993-1-2 (2005).

Table 1 Ambient properties for steel

Component	Yield strength f_y(N/mm^2)	Elastic modulus E (N/mm^2)
Beam	355	210000
Reinforcement bar	500	200000
Column	460	210000
Steel deck	350	210000

For concrete, an advanced nonlinear concrete material model, which accounts for the combined effects of compressive nonlinearity, tensile crack opening and closure, and temperature, is employed for the 2D slab in the full slab model. Details of this concrete model can be found elsewhere (Izzuddin *et al.*, 2004). The basic ambient properties of concrete employed in ADAPTIC are listed in Table 2. The material degradations (i.e. compressive strength f_c, and compressive strain ε_{c1}) and the thermal strain of concrete induced by temperature elevation are in accordance with the relative recommendation in EN1994-1-2 (2005). It is noted that the tension resistance of concrete is also considered, which is presented by a linear ascending/descending response, and the same material degradation factors are adopted as the compressive behaviour. The sketches of the stress-strain relationships for steel and concrete are illustrated in Figure 11.

The stress-strain relationship of the 'concrete flange' for the grillage model is slightly different, where a linear descending branch in compression is considered instead of the nonlinear one used in the 2D slab concrete material model. Details of the concrete model for beam-column elements can been found elsewhere (ADAPTIC user manual, 2010).

Table 2: Ambient properties for concrete

Young's modulus E (N/mm^2)	31476
Possion's ratio	0.2
Tensile strength f_t (N/mm^2)	2.6
Compressive strength f_c (N/mm^2)	33
Compressive strain ε_{c1}	0.0021
Tensile softening slope E_{cr} (N/mm^2)	1000
Normalised initial compressive strength s_c	0.4
Normalised residual compressive strength r_c	0.0
Factor for biaxial compressive interaction b_c	0.6
Elastic shear retention factor β_s	0.5
Factor scaling direct tensile stresses for shear Φ_s	0.5
Normalised shear softening relative to direct tensile softening γ_s	0.0

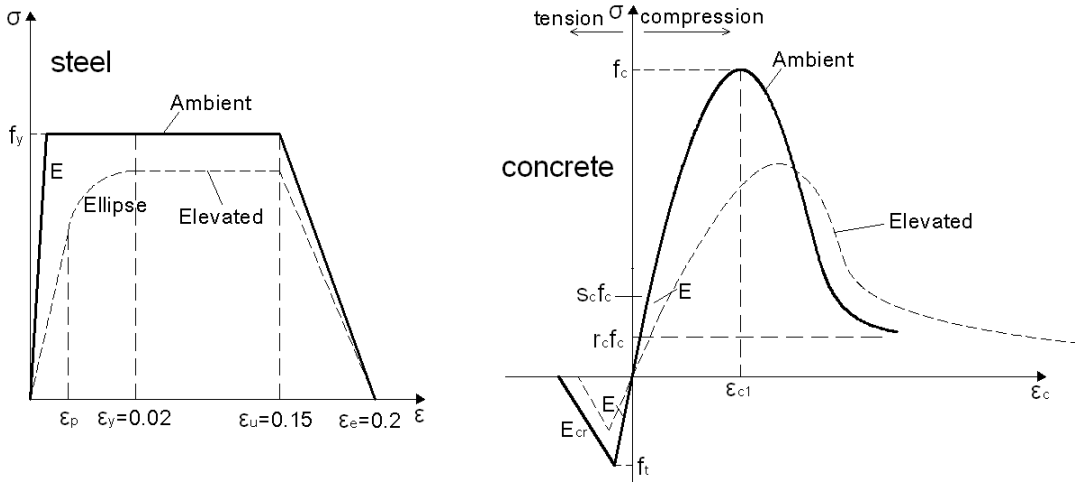

Fig. 11 Sketches of steel and concrete stress-strain relationships

IV.2 Structural modelling

IV.2.1 General

A multi-level modelling approach has been developed by Izzuddin et al. (2008) and Vlassis et al. (2008) for assessing the robustness of multi-storey buildings subject to sudden column loss scenarios at ambient conditions. This concept can be extended to the localised fire scenarios considered in this study. Three modelling levels (A, B and C) can be generally employed. At level A, consideration is given to a whole system of an influenced sub-structure with appropriate boundary conditions to represent the surrounding cool structures. The interactions among the heated column, the fire affected floor and the upper ambient floors are fully considered. Provided that the upper ambient floor systems have identical structure type and applied loadings, the assessment model can be simplified to level B, where a reduced model consisting of a fire affected floor-column system and the upper ambient floor systems is considered. At this level, the two systems (i.e. fire and ambient) are investigated separately. The derived characteristics of the ambient floors can be incorporated into a nonlinear 'spring' applied at the top of the fire-affected floor system. Then emphasis is given to the behaviour of the fire affected floor system with the added spring. Finally, at level C, planar effects within the floor slab are ignored, and grillage models with composite beams are considered instead. The illustrative descriptions for the three modelling levels are shown in Figure 12.

It is expected that the upper ambient floors can provide a certain level of load resistance for the fire floor, and the response of each upper ambient floor is basically similar to each other. Although the boundary conditions for the edge floor systems may be slightly variable due to the difference in column sizes adopted for different floors, this difference is negligible. In this respect, only the model levels B and C are

considered in the current study because they are relatively simpler compared with the overall structural model (level A), and sufficient accuracy can still be maintained.

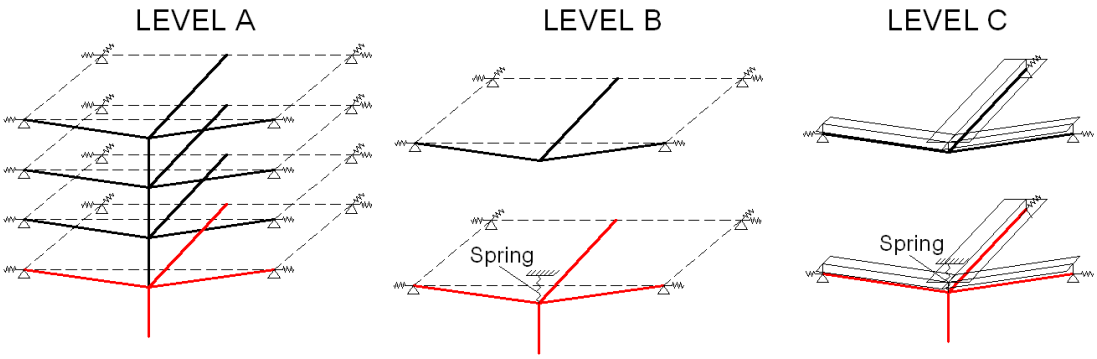

Fig. 12 Illustrative descriptions of three model levels

IV.2.2 Beam/column modelling

Cubic elasto-plastic beam-column elements are employed to simulate the steel beams and columns (Izzuddin and Elnashai, 1993a, 1993b). A full shear interaction between the steel beams and concrete slabs is assumed and is realised by interconnecting the steel beams and the slab through rigid links. A linear elastic boundary spring is applied at the end of each primary beam to replicate the axial response of the adjacent member. The stiffness of the boundary spring varies in tension and in compression. The stiffness of the boundary spring in tension is contributed by the axial stiffness of the adjacent beam E_sA_s/L and the axial stiffness of the steel connection on the other side of the supported column, where E_s is the steel Young's modulus, A_s is the area of the steel beam cross section, and L is the length of the adjacent beam. Due to cracking, the tensile stiffness of concrete is ignored. The compressive stiffness of the primary beam boundary spring is calculated from the axial stiffness of the composite cross-section $E_sA_s/L+E_cA_c/L$ assuming an effective width of the concrete flange, where E_c is the concrete Young's modulus, and A_c is the effective cross-section of concrete flange ignoring the ribbed part. The rotational flexibility of the boundary spring is assumed as infinite. In the considered model, the stiffness of the primary beam boundary springs in tension and compression are 229.7kN/mm and 734.2kN/mm, respectively. The stiffness of the boundary springs for secondary beams are taken as zero due to the lacking of blocking ramps in the transverse direction of the car park.

For elevated temperature analysis of the steel beams, three temperatures (i.e. top flange, web, and bottom flange) at each node are captured at a time interval of 3 minutes during the scenario. Parabolic temperature curves are employed across the cross-section with the three points. For the fire affected steel column, a uniform temperature distribution along the length and across the cross-section is considered.

IV.2.3 Slab modelling

Regarding the selected model levels B and C, two slab modelling approaches are considered accordingly, which are named the shell element slab model and the composite grillage model.

For the level B slab model, the shell element, which considers the geometric orthotropy, compressive nonlinearity, crack opening and closure as well as temperature, are employed (Izzuddin et al. 2004). The modified Reissner-Mindlin hypothesis is employed to capture the influence of geometric orthotropy more accurately. Additional Rib freedoms in conjunction with the conventional freedoms typically associated with shell elements are incorporated in the new element which was proved to have sufficient accuracy and robustness via comparisons with experimental results and other analysis tools. The slabs are assumed to be vertically supported and free to rotate along supporting edges. Full horizontal (planar) restraints are applied along the edges of the slab perpendicular to the primary beam directions, while no horizontal restraint is applied along the two other edges.

With respect to the level C slab model, a composite grillage is established. The slab is represented by elasto-plastic beam-column elements (Izzuddin and Elnashai, 1993a, 1993b), of which the effective width calculation for the concrete slab is provided from the Eurocode (EN1994-1-1, 2004) to consider the shear lag effects. Assuming the distance between the centres of the two outstand shear connectors of 150mm, and considering a double-span action of the composite beams, the effective concrete flange width for the secondary beams at both mid-span and supporting areas is 3.333m, while the ones for the primary beams at mid-span and two end-supporting areas are 3.65m and 2.025m, respectively. Instead of adopting a linearly increasing width in the length from the end support to the edge of the mid-span area, a constant average value of effective width (i.e. the mean value of 3.65m and 2.025m) is employed along the end support area. The beam-column elements with a T-section are employed for simulating the primary beam concrete sections parallel to the ribs. The ratio of upper width over lower width of the T-section is determined by the ratio of total slab width over the width of ribs. Besides the equivalent cross-sectional area of reinforcement to represent the anti-crack reinforcement mesh ($250mm^2/m$), an additional equivalent cross-sectional area of reinforcement is added at the bottom of the elements to simulate the steel deck ($1000mm^2/m$). For the secondary concrete sections perpendicular to the direction of ribs, only the concrete and reinforcement above the top of rib profile is considered, and the contribution of steel deck is also ignored. The sketches of the primary and secondary composite sections are illustrated in Figure 13.

It is noted that in order to enhance the joint performance, additional reinforcement bars are positioned in the slab to mobilise the composite response. This is realised by employing the elements (either shell elements or beam-column elements) locally with heavier reinforcement ratios in the required direction in the vicinity of joint areas where additional rebars are applied.

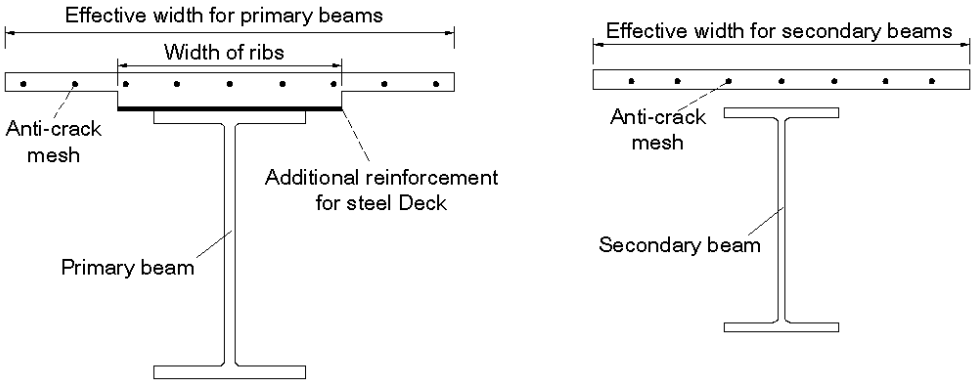

Fig. 13 Sketches of cross-sections in grillage model

At elevated temperature, the temperature distribution over the cross-section is modelled using a multi-linear approximation through several monitoring points for the full slab model, as shown in Figure 14. The temperature at the middle position of the 'concrete cover', the temperature difference between the cover bottom and slab top, and the temperature within the steel deck of the cover part of slab are captured. For the ribbed part, the temperature of the concrete rib and the one within the steel deck at the rib bottom are additionally considered.

For the grillage model, the elevated temperature modelling of the slab flange is similar to the one for the steel beams. For the primary beam slab flange, three temperatures (slab top, slab middle, steel deck) at each node are captured. Parabolic temperature curves are employed across the cross-section with the three points. For the secondary beam slab flange, due to the fact that the steel deck and the ribs are ignored, and the remaining parts are generally under room temperature, no elevated temperature is considered in the secondary slab flange.

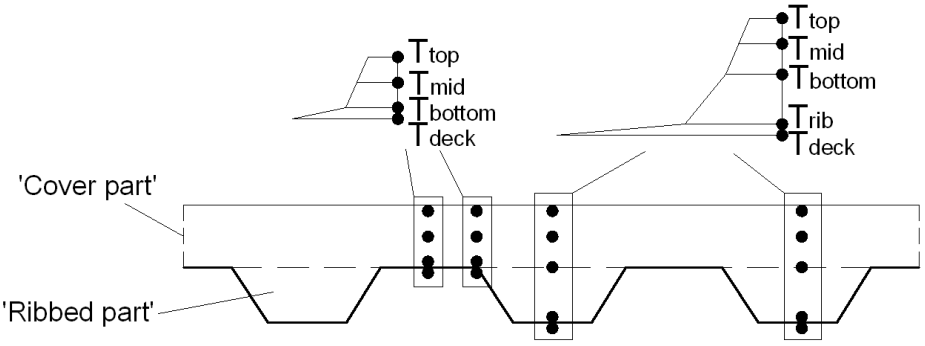

Fig. 14 Temperature capturing points over the cross-section of 3D slab

IV.2.4 Joint modelling

In this study, the joints are simulated using a component-based method which is a simplified analytical approach adopted in the Eurocode (EN 1993-1-8, 2005). The principle of this method is to separate a joint into a tension zone (T-stubs), a compression zone, and a shear zone, and each zone is further divided into several basic components of known characteristics. The component-based method can possess sufficient accuracy if the property (i.e. load-displacement relationship) of

each component is accurately predicted. In the current global model, sets of axial springs to represent individual bolt rows and compression zones are modelled, and temperature effects are considered by degrading the properties of these springs. Through this approach, the axial force and bending moment of the joints can be coupled. For now, the shear action is considered separately and not coupled with bending or axial loading.

IV.2.4.1 Identification of active components

The components used for the simulation of the major axis end-plate joints, the minor axis double web-cleat joints, and the beam-beam double web-cleat joints can be selected from the following 'component library':

Shear zone:
1) Column web in shear (cws)
Tension zone:
2) Column web in tension (cwt)
3) Bolts in tension (bt)
4) Bolts in shear (bs)
5) End plate in bending (epb)
6) Column flange in bending (cfb)
7) Angle in bending (ab)
8) Angle plate in bearing (abr)
9) Beam web plate in bearing (bwbr)
Compression zone:
10) Beam web/flange in compression (bwfc)
11) Column web in compression (cwc)

The behaviour of each component is represented by a force-deformation relationship, which is usually characterised by bi-linear, tri-linear, or nonlinear curves (Figure 15). In the considered model, the bi-linear curves are employed to simulate the load-deformation response of each component. The first segment of the curve represents the elastic performance with a stiffness of k_e, followed by a post-limit curve with a post-limit stiffness $k_{pl}=\mu_1 k_e$, where μ_1 is a strain hardening coefficient. EN1993-1-8 (2005) provides full details for the calculation of initial stiffness and resistance of each component; these are reproduced in Table 3.

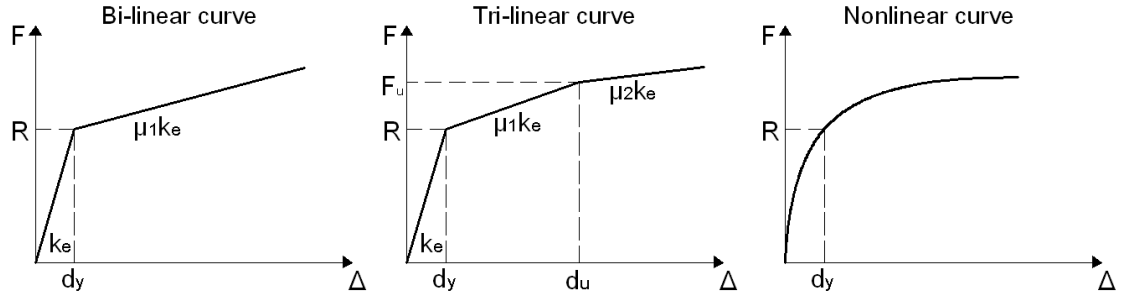

Fig.15 Load-deformation relationships for components

IV.2.4.2 Joint ductility supply / failure criteria

Compared with normal loading conditions, larger deflections are inevitable when structures are subjected to extreme loadings. The vulnerability of a structure to progressive collapse greatly depends on the capability of the joints to withstand large deformations. Predictions of the joint ductility supply require a clear definition of failure criteria that can explicitly account for the ductility supply of each individual joint component. In other words, the joint ductility capacity is directly associated with the deformation capacity of each active component.

So far few investigations have been devoted to systematic evaluations of the post-limit response for each individual component. EN1993-1-8 (2005) suggested that the post-limit stiffness can conservatively be taken as zero. In reality, the post-limit stiffness may be considerable for some components, especially for high ductility components; hence ignoring them may lead to an underestimation of rotational and bending moment capacities of the considered joints to a great extend. Al-Jabri et al. (2004) and Ramli-Sulong *et al.* (2007) suggested a 5% strain hardening coefficient for a ductile component until its ultimate strength is reached. Simões da Silva *et al.* (2002) adopted different strain hardening coefficients for various ductile components, where the values range from 1% to 5%. Based on the limited available data, the strain hardening coefficient μ_1 is taken as 3% for all ductile components in this study. With respect to the deformation capacity of each component, three ductility classes were first proposed by Kuhlmann *et al.* (1998), namely, the components with high ductility, the components with limited ductility, and the components with brittle failure, respectively. Based on this concept, a ductility index $\varphi=d_f/d_y$ for each component was developed by Silva *et al.* (2002), where d_f is the maximum deformation, and d_y is the elastic deformation for each component. The deformation capacity for each component considered in this model is given in table 3. In the following analysis, a structural system is deemed to fail when any joint firstly exceeds its ductility supply capacity, and the considered joint is assumed to reach its ductility supply capacity when any of the weakest active components firstly exceeds its deformation capacity.

Notwithstanding, as noted in Table 3, all the 'high ductility' components have an infinite deformation capacity in tension, which is unrealistic. Vlassis *et al.* (2008). suggested 30mm for the tensile deformation capacity of each bolt-row in typical end-plate and web-cleat joints. This value is based on the relevant test data (Jarrett, 1990; Owens and Moore, 1992). Nine flexible end-plate and eleven double-web angle connections were tested under tensile force until failure by Jarrett (1990). The average axial deformation capacities for the two connection types are 25.4mm and 37.2mm respectively. Similar tests were undertaken by Owens and Moore (1992), and the average axial deformation capacities for end-plate and web-cleat connections are 26.8mm and 37.3mm respectively. In this study, maximum deformations of 25mm and 35mm are employed for all bolt-rows in end-plate connections and double web-cleat connections respectively, according to the value recommended by Vlassis *et al.* (2008).

Table 3 Elastic response and ductility classification for each component

Ductility index	Component	Elastic Resistance	Stiffness	Limit deformation (d_f/d_y)
High ductility	Column web in shear	$R_{cws} = \frac{0.9 f_{y,wc} A_{vc}}{\sqrt{3}}$	$k_{cws} = E\frac{0.38 A_{vc}}{\beta . z}$	Infinite
	Column web in tension	$R_{cwt} = \omega b_{eff,t,wc} t_{wc} f_{y,wc}$	$k_{cwt} = E\frac{0.7 b_{eff,t,wc} t_{wc}}{d_c}$	Infinite
	End-plate in bending	*Equivalent T-stub model*	$k_{cfb} = E\frac{0.85 l_{eff} t_{fc}^{\ 3}}{m^3}$	Infinite
	Column flange in bending	*Equivalent T-stub model*	$k_{cfb} = E\frac{0.85 l_{eff} t_{fc}^{\ 3}}{m^3}$	Infinite
	Angle in bending	*Equivalent T-stub model*	$k_{ab} = E\frac{0.85 l_{eff,a} t_a^{\ 3}}{m_a^{\ 3}}$	Infinite
Limited ductility	Angle plate in bearing	$R_{ab} = k_1 a_b f_u d t_a$	$k_{abr} = 24 n_b k_b k_t d f_u$	15
	Beam web plate in bearing	$R_{bwbr} = k_1 a_b f_u d t_{bw}$	$k_{bwbr} = 24 n_b k_b k_t d f_u$	15
	Column web in compression	$R_{cwc} = \omega k_{wc} \rho b_{e,ff,c,wc} t_{wc} f_{y,wc}$	$k_{cwc} = E\frac{0.7 b_{eff,c,wc} t_{wc}}{d_c}$	5
Brittle failure	Bolts in tension	$R_{bt} = 2 k_2 f_{ub} A_s$	$k_{bt} = 1.6 E A_s / L_b$	1
	Bolts in shear	$R_{bs} = n_s \alpha_v f_{ub} A_s$	$k_{bs} = \frac{16 n_b d^2 f_{ub}}{d_{M16}}$	1
	Beam flange/web in compression	$R_{bfwc} = \frac{M_{c,Rd}}{z}$	∞	1

Note:
1) Apart from the above limit, an additional deformation limit of 35mm is applied for all bolt-rows in tension in double web-cleat joints, and 25mm for all bolt-rows in tension in end-plate joints.
2) For joints designed in terms of composite behaviour, the rupture deformation of reinforcement bars are in accordance with the simplified calculation method proposed by Anderson *et al.* (2000), and is considered as an additional failure criterion.

The shear resistance of joints is also considered in the mechanical model through incorporating a rigid-plastic load-deformation curve into the vertical shear property of the bottom spring of the joint model. The load-deformation response of the shear spring is illustrated in Figure 16. Indeed, shear failure is not likely to occur in ambient joints, since they are usually designed with sufficient resistance reserve to consider the increased shear force due to column loss. Under fire conditions, however, the shear resistance of fire affected joints can be greatly impaired under high temperatures; therefore the shear failure of the fire affected floor has to be considered as a possible failure mode.

Considering a floor system in fire as shown in Figure 17, shear failure is deemed to occur when the overall shear force applied onto the four steel beam-to-column connections exceeds their overall shear resistance at elevated temperatures. This failure criterion assumes a rigid-plastic shear failure response of all the beam-to-column connections and allows for shear force redistribution among the adjacent connections after any first connection attains its maximum shear resistance. Contribution to the shear resistance from concrete slab is not considered in this study.

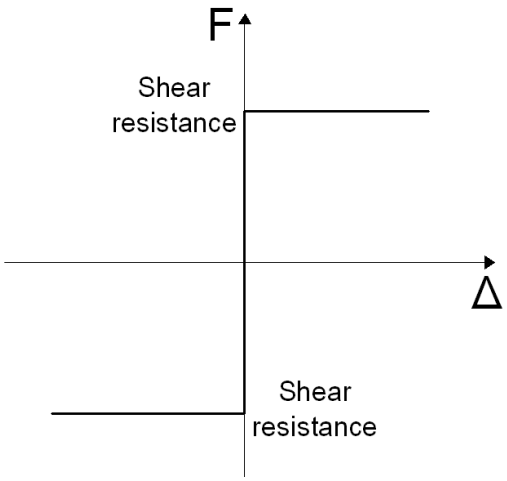

Fig. 16 Rigid-plastic shear response of connections

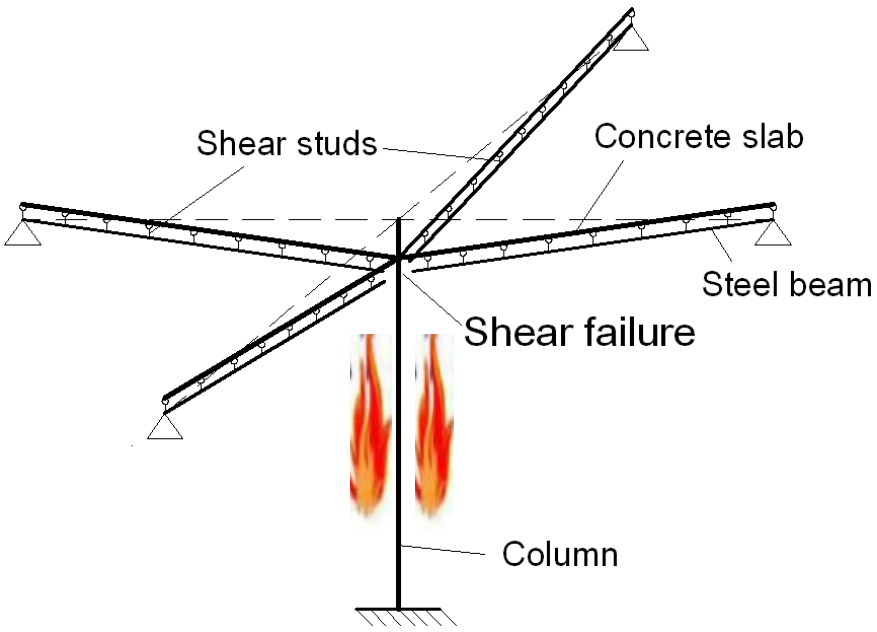

Fig. 17 Illustration of shear failure of fire affected floor system

When composite action is considered, the ductility of composite joints not only relies on the deformation capacity of the steel component discussed above, but is also associated with the rupture of reinforcement rebars. Due to steel-concrete bond action and cracking of concrete, the reinforcement stress is concentrated in the

vicinity of the cracking, which leads to the rupture of the reinforcement bars only at crack locations. The CEB-FIP model code (1990) gives a simplified stress-mean strain relation for embedded reinforcement and compares with the corresponding curve for bare reinforcement (Figure 16). Based on this model, Anderson *et al.* (2000) developed a simplified calculation method for predicting the rotational capacity of composite joints due to ultimate reinforcement elongation. This method has been proved to have sufficient accuracy through validations against experiments, and it has been employed by various researchers (Vlassis et al. 2008; Gil and Bayo, 2008; Fu et al. 2010). The principle of the method is to predict the ultimate mean strain of embedded reinforcement ε_{smu} that is related to the properties of bare reinforcement and concrete, and then to obtain the maximum reinforcement elongation $\Delta_{u,s}$ through multiplying ε_{smu} by an effective length. The details of the method are repeated as follows.

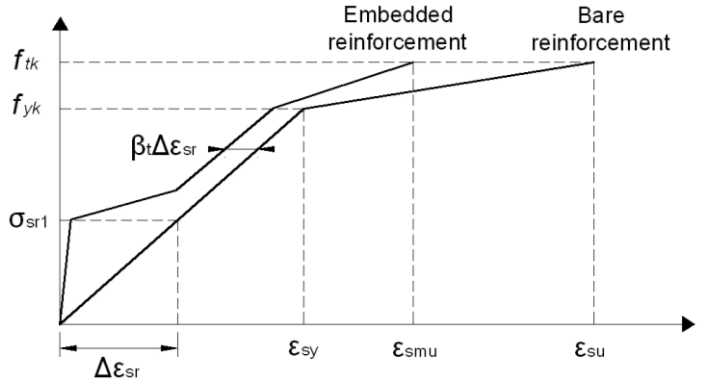

Fig.16 Simplified stress-strain relationship of embedded reinforcement (CEB, 1990)

The ultimate mean strain ε_{smu} is calculated as follows:

$$\varepsilon_{smu} = \varepsilon_{sy} - \beta_t.\Delta\varepsilon_{sr} + \delta.\left(1 - \frac{\sigma_{sr1}}{f_{yk}}\right).\left(\varepsilon_{su} - \varepsilon_{sy}\right)$$

where

β_t is taken as 0.4 for short-term loading,

$\Delta\varepsilon_{sr}$ is the increase of reinforcement strain when the first crack forms, $\Delta\varepsilon_{sr} = \dfrac{f_{ctm}k_c}{E_s\rho}$,

δ is taken as 0.8 for high ductility bars,

σ_{sr1} is the reinforcement stress at the location of first crack, $\sigma_{sr1} = \dfrac{f_{ctm}k_c}{\rho}\left(1 + \rho\dfrac{E_s}{E_c}\right)$,

ρ is the longitudinal reinforcement ratio,

k_c is a coefficient that allows for the self-equilibrating stresses and the stress distribution in the slab prior to cracking, $k_c = \dfrac{1}{1 + d/2z_0}$,

d is the thickness of the concrete flange, excluding any ribs,

z_0 is the vertical distance between the centroid of the uncracked, unreinforced

concrete flange and the uncracked, unreinforced composite section, calculating using the modular ratio for short-term effects.

Then, calculate the ultimate reinforcement elongation $\Delta_{u,s}$:

$\Delta_{u,s} = 2.L_t.\varepsilon_{smu}$ for ρ<0.8%

$\Delta_{u,s} = \left(\frac{h_c}{2} + L_t\right).\varepsilon_{smu}$ for $\rho \geq 0.8\%$, and $a < L_t$

$\Delta_{u,s} = \left(\frac{h_c}{2} + L_t\right).\varepsilon_{smu} + \left(a - L_t\right).\varepsilon_{smy}$ for $\rho \geq 0.8\%$, and $a > L_t$.

where

a is the distance from the face of column to the first shear stud,

h_c is the column section depth,

L_t is the transmission length $L_t = \frac{k_c.f_{ctm}\phi}{4.\tau_{sm}.\rho}$,

ϕ is the diameter of the reinforcement bar,

τ_{sm} is the average bond stress along the transmission length $\tau_{sm} = 1.8 f_{ctm}$.

IV.2.4.3 Elevated temperature degradation

Joints in fire exhibit significant reductions in strength and stiffness, thus consequently affecting the global response of the structure. Therefore, a method that could predict the actual response of a joint subjected to fire loading has to be carefully implemented.

The 'reduction factor approach' is employed in the current component-based model, where the reduction factors for strength and stiffness (SRF) recommended by Jabri et al. (2004) are adopted (Table 4) for all the components except the strength of bolts. For the response of bolts, Kirby (1995) undertook a series of fire tests aimed to obtain the fire response of high-strength Grade 8.8 bolts. The degradation of the bolt strength was proposed, which is given in the following expressions. However, no recommendation has been given for the reduction factor on the stiffness of bolts; hence the stiffness reduction values in the table are also applicable for the bolts. The same values of the strain hardening coefficient (μ_1 =3%) and joint failure criteria are employed for the elevated temperature cases.

$\mathrm{SRF} = 1.0$ for T<300°C,

$\mathrm{SRF} = 1.0 - \left(T - 300\right) \times 2.128 \times 10^{-3}$ for 300°C <T<680°C,

$\mathrm{SRF} = 0.17 - \left(T - 680\right) \times 5.13 \times 10^{-4}$ for 680°C <T<1000°C,

where T is the temperature of the bolts.

Previous studies (Leston-Jones, 1997; Jabri, 1999) have indicated that the joint response at elevated temperatures can be predicted with adequate accuracy by considering only the material property degradation with increasing temperature. Hence the effect of thermal expansion within the connection components can be ignored. In ADAPTIC, a newly developed joint element which enables a tri-linear degradation of stiffness and strength with the increase of temperature is employed in this study. The tri-linear degradation approximation is illustrated in Figure 17.

Table 4 Strength and stiffness reduction factors recommended by Jabri et al. (2004)

Temperature (^{o}C)	Strength SRF	Stiffness SRF
20^{o}C	1.000	1.000
100^{o}C	1.000	1.000
200^{o}C	0.971	0.807
300^{o}C	0.941	0.613
400^{o}C	0.912	0.420
500^{o}C	0.721	0.360
600^{o}C	0.441	0.180
700^{o}C	0.206	0.075
800^{o}C	0.110	0.050
900^{o}C	0.060	0.0375
1000^{o}C	0.040	0.0250
1100^{o}C	0.020	0.0125
1200^{o}C	0.000	0.000

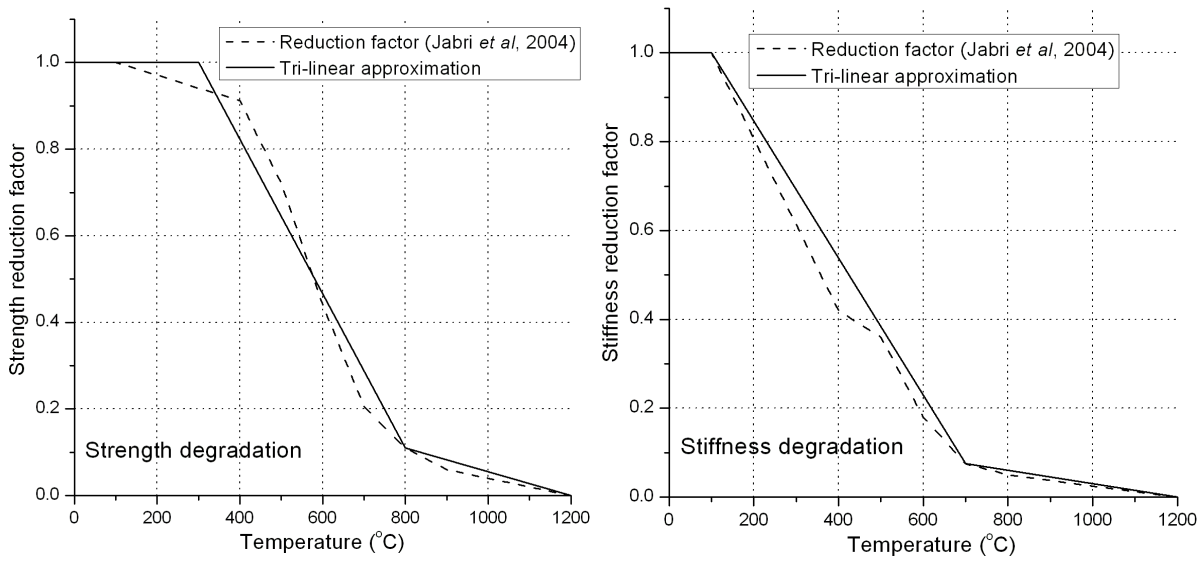

Fig.17 Tri-linear degradation approximation of strength and stiffness on joints

IV.2.4.4 Creep assessment

The aim of this study is to investigate the steel creep effect on the behaviour of steel joints at elevated temperatures. As a first step, a T-stub is considered and is ideally modelled using 2D beam elements, as illustrated in Figure 18. Carbon steel 1411 is employed for the steel material which is modelled with a bilinear stress-strain relationship. The ambient and elevated temperature material properties as well the parameters for steel creep can be found elsewhere (Song 1998; Izzuddin *et al.* 2000; Song *et al.* 2000).

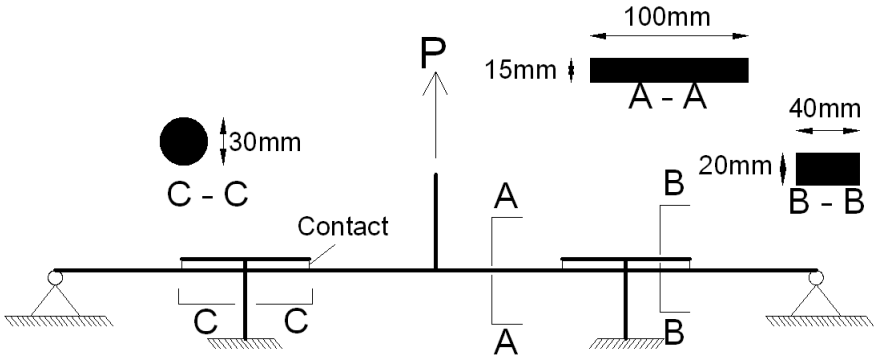

Fig. 18 Illustration of T-stub model using beam elements

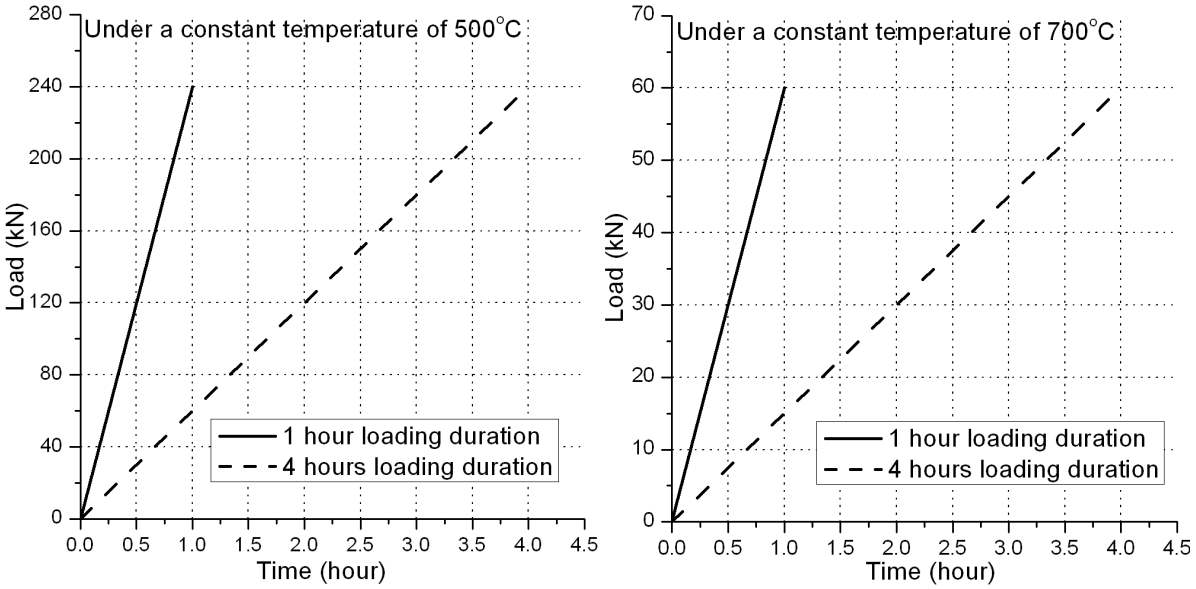

Fig. 19 Loading conditions for T-stubs

The considered T-stub model is subjected to a linearly increasing point load under two constant temperatures (500°C and 700°C), as shown in Figure 19. Two loading durations are considered, which are 1 hour and 4 hours. Figures 20 and 21 provide the load-displacement behaviour of the T-stub with different loading rates at the constant temperatures of 500°C and 700°C respectively. It can be seen that the influence of the creep effect is not significant at either 500°C or 700°C, but is more pronounced beyond 700°C.

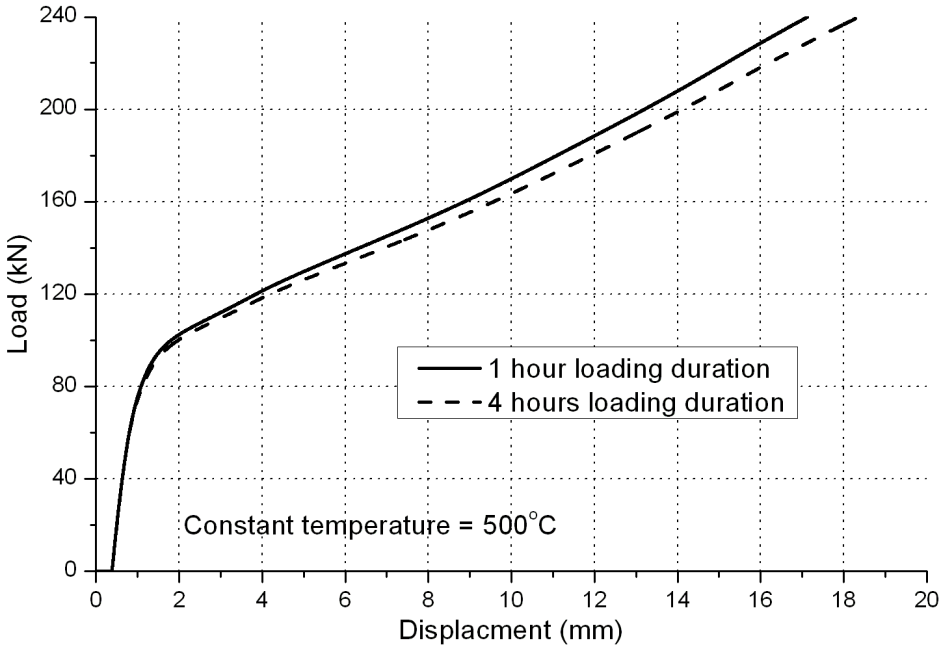

Fig. 20 load-displacement relationships of T-stub under 500°C

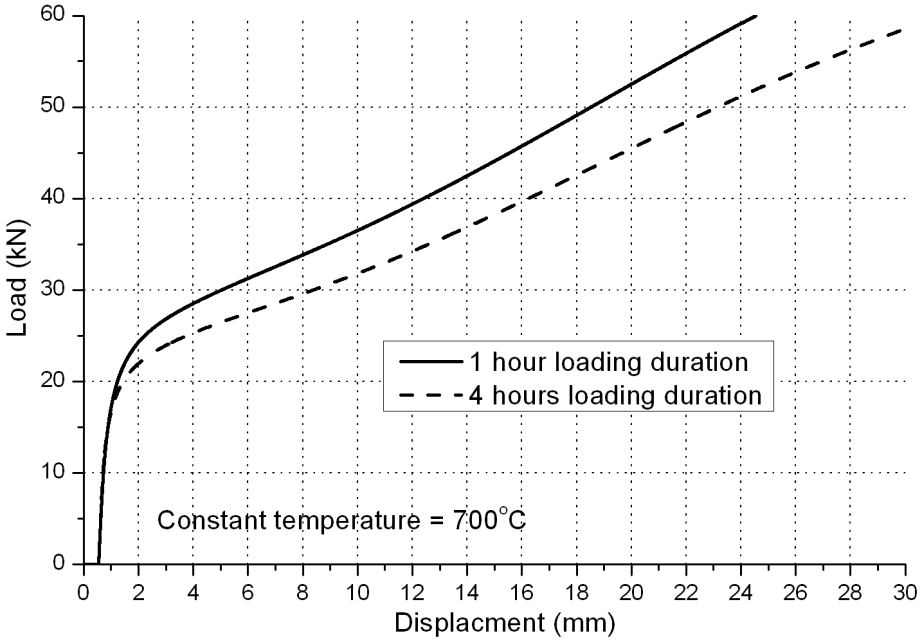

Fig. 21 load-displacement relationships of T-stub under 700°C

The results can also give a basic insight into suitable loading durations considered for the experimental tests in WP2. The proposal of the WP2 test loading duration for each test specimen is 5 hours, including 1 hour heating duration (to either 500°C or 700°C) and the subsequent 4 hours loading duration. Based on the findings from the T-stub behaviour, creep effect does not need to be considered for a 4 hours loading duration of the test specimen at 500°C, whereas at 700°C, a shorter loading duration is recommended in order to minimise the creep effect.

IV.2.4.5 Example of major axis beam-to-column joint modelling

Flush end-plate connections are employed for the major axis beam-to-column joints in the reference building, where geometry is depicted in Figure 3. The size of the supported primary beam is IPE550, and four sizes of supporting columns are considered depending on the floor level (HEB220, HEB300, HEB400, and HEB 550). The S355 15mm thick end-plate with four bolt-rows is welded to the supported beam web. M30 10.9 bolts in 32mm-diameter holes are employed to connect the plate to the column flange. The considered joints are assumed to be double-sided and have a shear capacity of 1302kN governed by the shear failure of beam web.

Figure 22 presents the mechanical model developed for predicting the flush end-plate response. Rigid links and spring series are employed to simulate the behaviour of bolt-rows and contact positions between the beam flange and the column flange. The axial properties in tension for the four internal bolt-row spring series are contributed from four components, namely, column web in tension (cwt), column flange in bending (cfb), bolt in tension (bt), and end-plate in bending (epb). The compressive characteristic for the inner springs are based on the resistance of column web in compression (cwc). The two outer spring series are free to be pulled in tension, but in compression the resistance and stiffness are contributed from the column web in compression (cwc) and the beam web/flange in compression (bwfc). Moreover, the column web in shear (cws) is represented by applying an additional spring at the bottom flange of the beam.

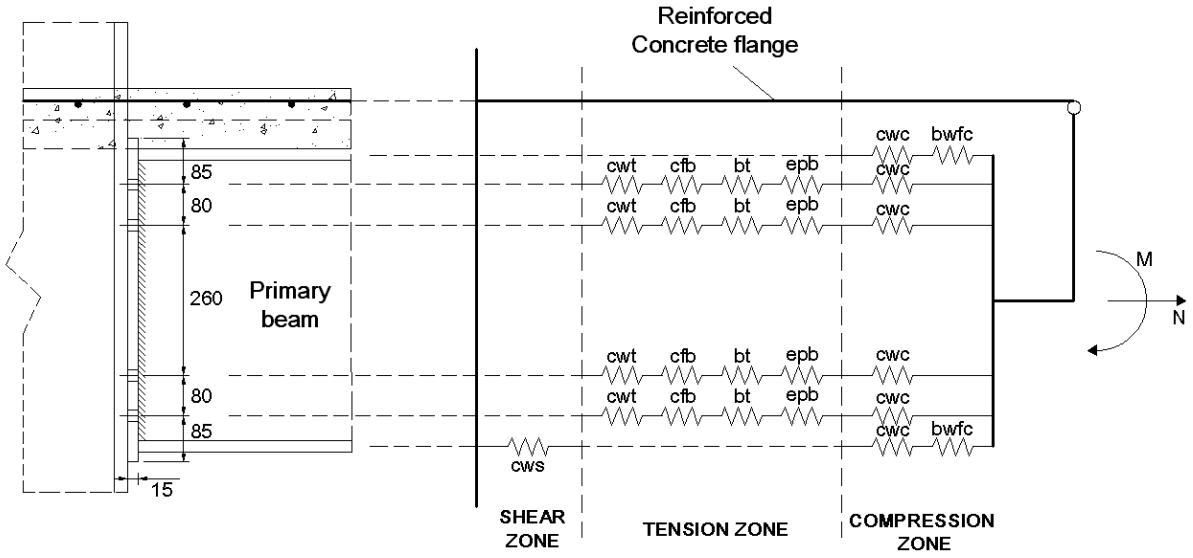

Fig. 22 Mechanical model for major axis beam-to-column flush end-plate joint

For the concrete flange, the effective width calculated from the grillage model is employed. The tensile strength of concrete is ignored conservatively. Ten 12mm diameter rebars are used, and for all the rebars, the yield stress is 500MPa with 0.01 strain hardening. The ultimate reinforcement strain is conservatively assumed to be 10%. Full interaction shear studs are considered, and the spacing between them is 250mm. According to the calculation method proposed by Anderson *et al.* (2000), the ultimate reinforcement elongation for the composite joint is 11.95mm. Figure 23 shows the moment-rotation relationships for each joint, and Table 5 provides the related bending moment capacities, the maximum rotations as well as the failure mode for the considered joints.

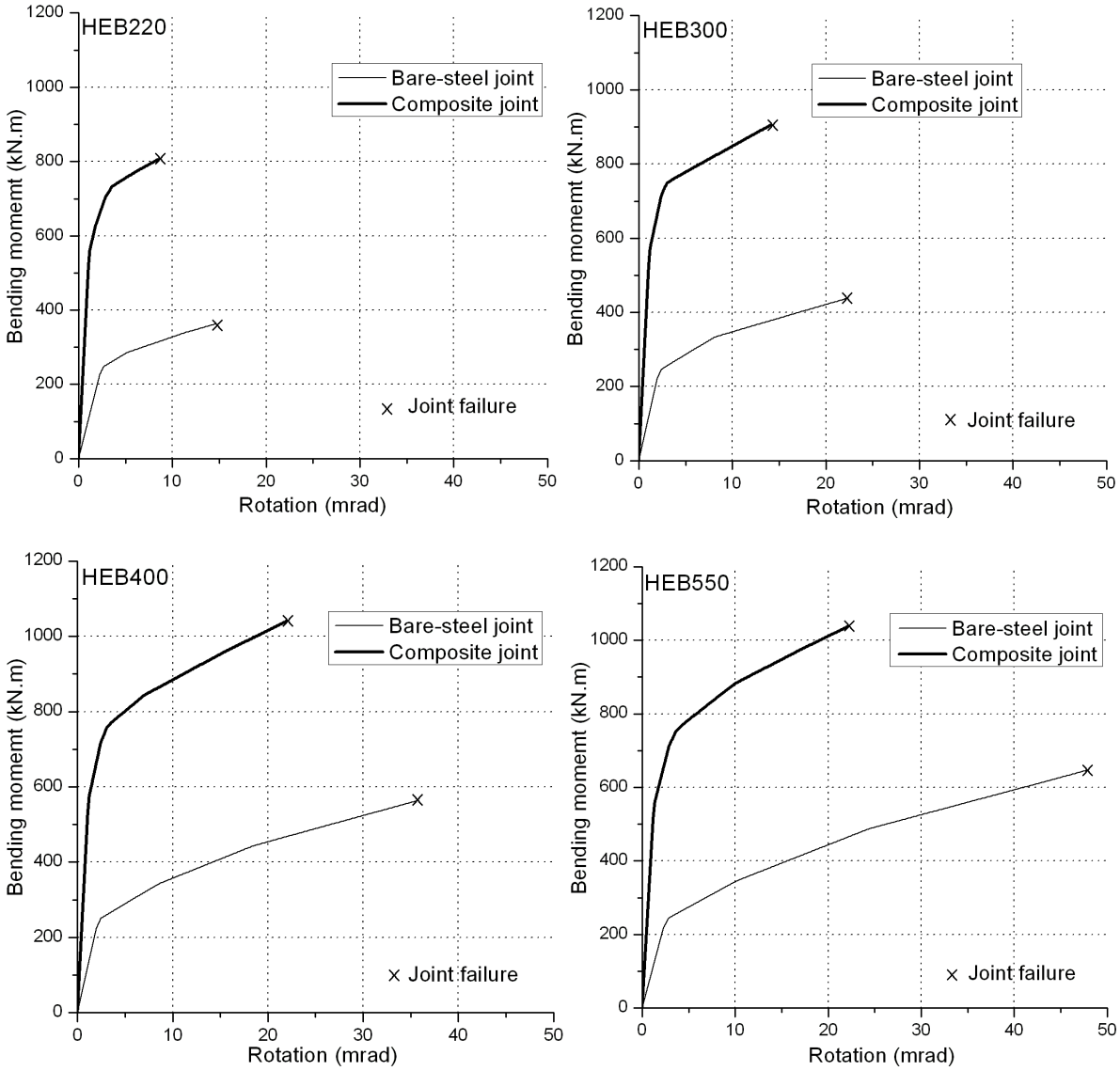

Fig. 23 Moment-rotation relationships of end-plate joints

Table 5 Failure data of end-plate joints

Joint	Bending moment Capacity (kN.m)	Maximum Rotation (mrad/degree)	Failure mode
Bare-steel joint (HEB220 column)	363	14.6 / 0.84^o	Column web in compression
Composite joint (HEB220 column)	806	8.5 / 0.49^o	Column web in compression
Bare-steel joint (HEB300 column)	438	22.3 / 1.28^o	Column web in compression
Composite joint (HEB300 column)	906	14.1 / 0.81^o	Column web in compression
Bare-steel joint (HEB400 column)	563	35.6 / 2.04^o	Column web in compression
Composite joint (HEB400 column)	1040	21.9 / 1.25^o	Rupture of reinforcement
Bare-steel joint (HEB550 column)	647	47.8 / 2.74^o	Column web in compression
Composite joint (HEB550 column)	1038	22.2 / 1.27^o	Rupture of reinforcement

IV.2.4.6 Example of minor axis beam-to-column and beam-to-beam joints modelling

Double web-cleat connections are employed for the minor axis beam-to-column joints and the beam-to-beam joints in the reference building, and their geometries are illustrated in Figure 3. The size of the supported secondary beam is IPE450, which is connected to the column web / beam web with two 150×150×10mm angle plates using four rows of M24 10.9 bolts. This joint has a shear capacity of 617kN governed by the bearing failure of the beam web. The mechanical model is illustrated in Figure 24. The four internal bolt-row spring series represent the behaviour of four bolts-rows, where the axial property in the tension zone is contributed from five components, namely, bolts in tension (bt), bolts in shear (bs), angle plate in bending (ab), angle plate in bearing (abr), and beam web in bearing (bwbr). The compressive characteristics for the four inner springs depend on the properties of bolts in shear (bs), angle plate in bearing (abr), and beam web in bearing (bwbr). The two outer spring series are free to be pulled in tension, but in compression, the resistance and stiffness are contributed from the beam web/flange in compression (bwfc). Moreover, two additional gap-contact elements are adopted to simulate the 10mm gap between the beam flanges and the column/beam web. The gap between bolts and bolt-holes and the friction between bolts and plates are not considered in this mechanical model. The elastic responses and failure criteria for all the components are based on Table 3. Due to the limited available data, bilinear curves are adopted for the post-limit stiffness, and a strain hardening coefficient of 3% is employed for all applicable components.

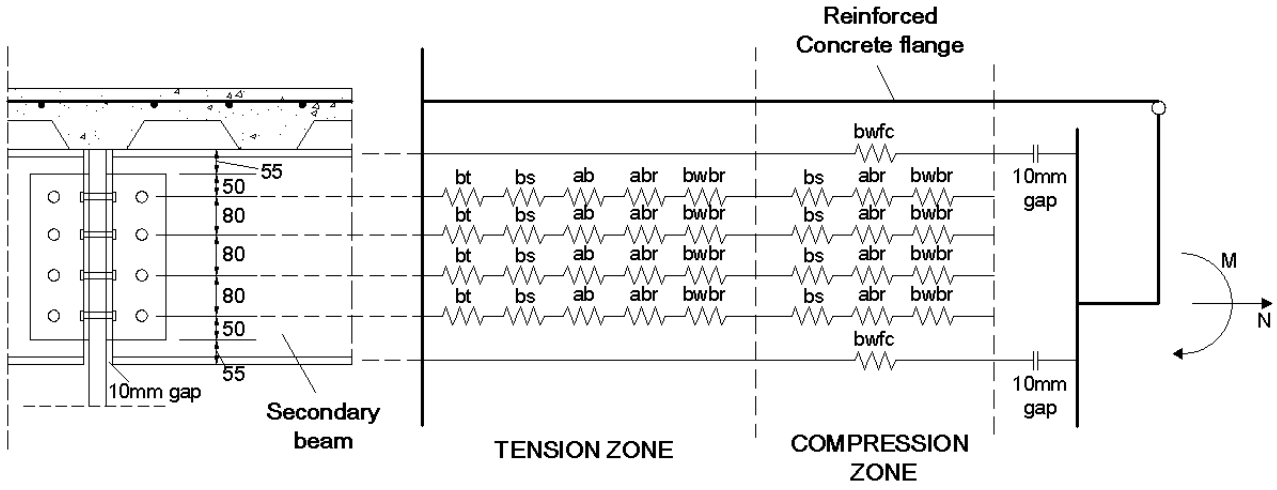

Fig. 24 Mechanical model for minor axis beam-to-column and beam-to-beam double web-cleat joints

Figure 25 shows the moment-rotation relationships for both bare-steel minor axis and beam-to-beam joints, from which it can be observed that the bare-steel double web-cleat joint has a much better ductility in comparison with the major axis beam-to-column flush end-plate joints.

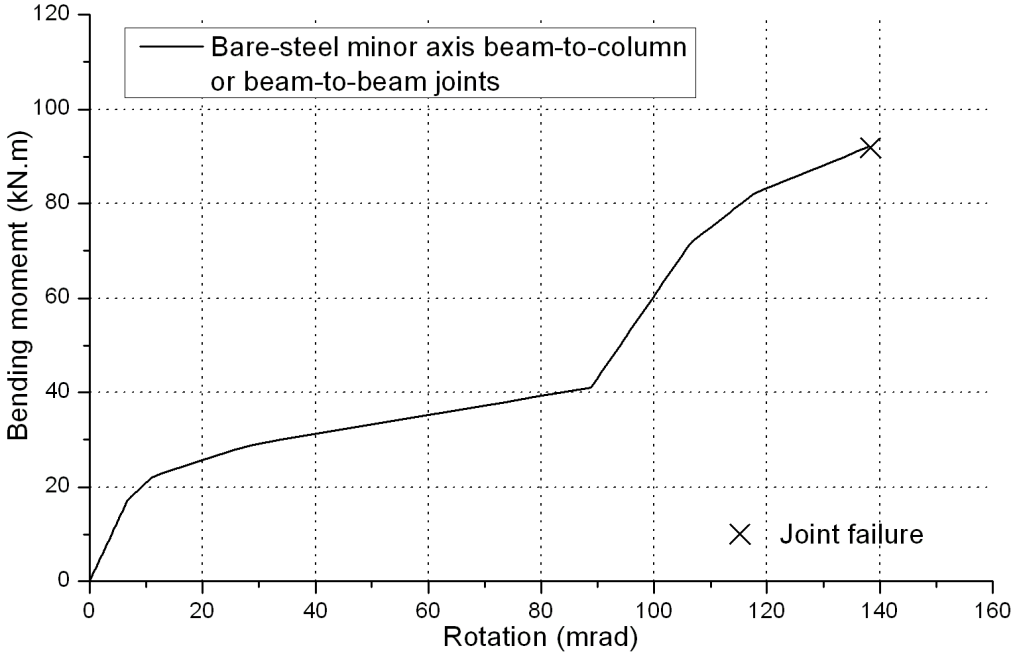

Fig. 25 Moment-rotation relationships of bare-steel web-cleat joint

V Structural analysis

System models subject to the selected load scenarios are analysed and discussed in this section. The considered system model is comprised of a fire affected column, a fire affected floor (either grillage approximation or full slab model), and a non-linear spring that replicates the performances of the above ambient floors. Each individual ambient floor has to be investigated first to assess its stiffness and resistance.

Accordingly, the characteristics of the spring can be obtained from the superposition of the responses of all the above floors. Finally, analysis is undertaken on the fire affected system model with initial gravity load and subsequent thermal load.

V.1 Response of upper ambient floor

Due to the different column sizes adopted for different floors, hence the diversity of ductility supplies that joints can offer, different types of floors supported by different columns (i.e. floor systems supported by HEB220, HEB300, HEB400, and HEB550 columns) should be considered individually.

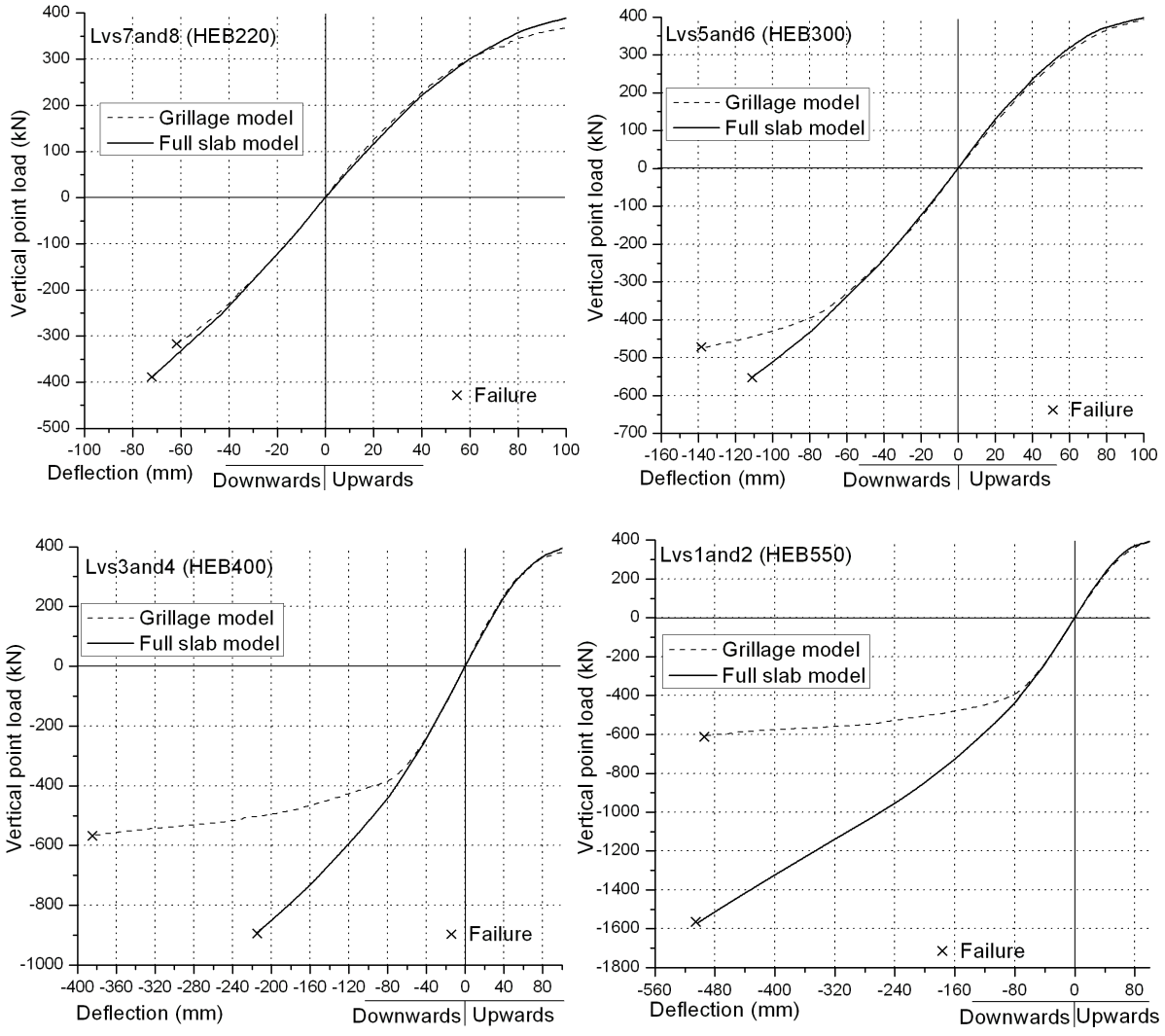

Fig. 26 Ductility supply of ambient floors

For each ambient floor system, a 5kN/m^2 UDL and an upward point load (exerted at the position of internal column) is initially applied. The upward point load is used to represent the supporting internal column, such that the initial floor deflection at the column location is zero. Subsequently, an increasing downward point load is exerted at the same position until one of the joints exceeds its ductility supply. The load-deflection relationship of the ambient floor can be recorded and incorporated as a part of the spring connected to the column top of the fire affected floor for later analysis. Considering the thermal elongation of the fire affected column, the evaluation of the upward stiffness of the ambient floor is also necessary. Figure 26 provides the ductility provision of each ambient floor in the grillage model as well as the full slab model. The maximum vertical deflection, the corresponding downward point load, and the failure mode of each ambient floor are given in Table 7.

Table 7 Response of each ambient floor

Floor levels	Vertical point load at failure (kN)	Maximum vertical deflection (mm)	Failure mode
Levels 1 and 2 grillage model (HEB550)	608	493.9	Rupture of reinforcement in hogging major axis beam-to-column end-plate joint
Levels 1 and 2 full slab model (HEB550)	1568	502	Failure of column web in compression in hogging major axis beam-to-column end-plate joint
Levels 3 and 4 grillage model (HEB400)	566	386.4	Failure of column web in compression in hogging major axis beam-to-column end-plate joint
Levels 3 and 4 full slab model (HEB400)	890	214.4	Failure of column web in compression in hogging major axis beam-to-column end-plate joint
Levels 5 and 6 grillage model (HEB300)	476	140.7	Failure of column web in compression in hogging major axis beam-to-column end-plate joint
Levels 5 and 6 full slab model (HEB300)	552	111.6	Failure of column web in compression in hogging major axis beam-to-column end-plate joint
Levels 7 and 8 grillage model (HEB220)	318	62.2	Failure of column web in compression in hogging major axis beam-to-column end-plate joint
Levels 7 and 8 full slab model (HEB220)	390	72.2	Failure of column web in compression in hogging major axis beam-to-column end-plate joint

It is shown that the failure of the supported column web in compression governs the collapse of almost all floors in the considered building, except the floor levels 1 and 2 in the grillage model, where the ultimate elongation of the reinforcement bars in hogging major axis joints is exceeded first. Since the failure mode is mainly attributed to the weakness of supported column web in compression, the upper floors have much less resistance than the lower floor where larger column sizes are employed. Moreover, the response of the full slab model subject to the vertical load starts to be stiffer than the one of the grillage model after a certain value of deflection (approximately 60mm). This is due to the fact that flexural bending action is mainly developed in the floor system when the deflection is relatively small, so the two models have a close vertical stiffness. However, as the deflection increases, benefits from 3D slab effect (e.g. membrane action) start to appear, which can enhance the vertical resistance and stiffness of the floor system. At a deflection of about 500mm for example, the vertical point load resisted by the full slab floor can be more than twice of what the grillage floor takes. This phenomenon indicates that using the grillage approximation that takes no account of slab 2D action can be overly conservative in assessing the resistance of floor systems from the robustness perspective.

Finally, it can be observed that when failure occurs, all the steel beams are still in compression. This implies that catenary stage, which has been recognised to be effective in postponing the collapse of floor systems, is largely prohibited by the premature failure of joints. Therefore, increasing the ductility of joints is essential to ensure a full development of catenary action, thus allowing a higher progressive collapse resistance of upper ambient floors.

V.2 Response of fire affected structural system

It is worth noting from the above discussion that the yielding of the perimeter column webs in compression dominates the failure mode of ambient floors at higher floor levels where smaller column sizes are employed. This type of failure inevitably reduces the vertical resistance of the unaffected perimeter columns, thus increasing the potential for a wider and more catastrophic failure of an entire floor. This is however in conflict with the robustness limit state defined initially for the current study, where no collapse of any floor system is allowed. Therefore, for the structural models considered in this section, column web stiffeners are added on all columns to avoid the premature failure of the column web in compression. The modified curves describing the typical vertical load-deflection responses of the grillage model and the full slab model that employ additional column web stiffeners are illustrated in Figure 27.

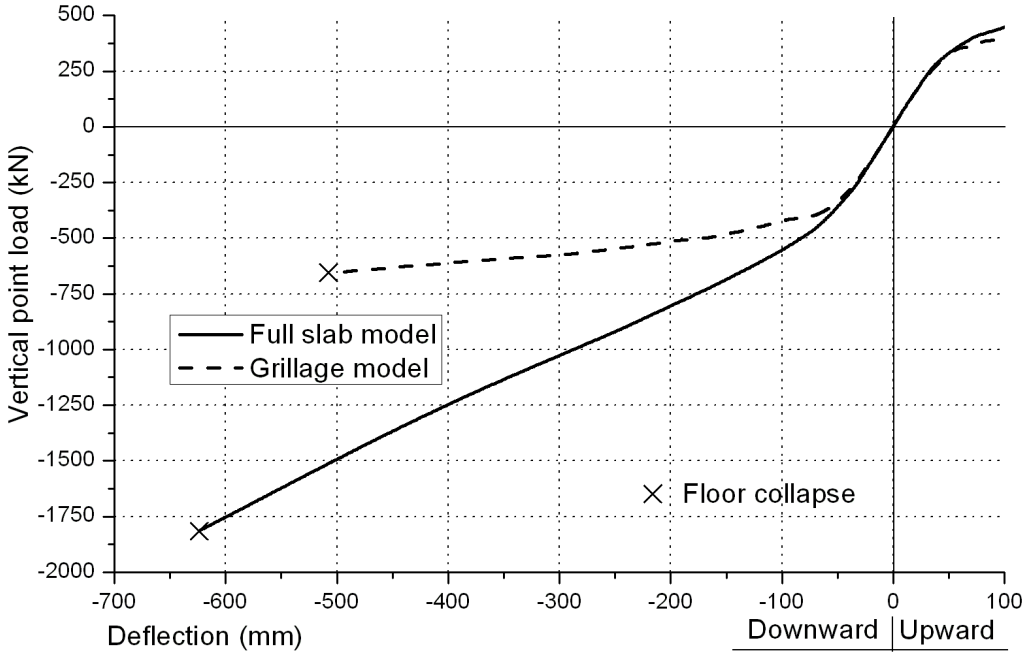

Fig. 27 Ductility supply of ambient floors (with column web stiffeners)

The selected fire scenarios at three selected floors levels are considered in this study, which are floor level 1, level 5, and level 8. Two slab modelling approaches (grillage approximation and full shell element model) are used and compared. The analysis is performed over a time domain, where the temperature-time response of the entire system model is extracted from the thermal analysis completed by SAFIR.

V.2.1 Fire at floor level 1

The deflection of the fire affected floor and the column axial forces for the grillage model and the full slab model during the considered fire scenario are shown in Figures 28 and 29 respectively. The response of column axial force is represented by the P_t/P_0 ratio, where P_t is the column axial force during the fire and P_0 represents the initial compressive force carried by the column.

The structural behaviour predicted by the full slab model shows that buckling of the fire affected column occurs at around 25minutes (column temperature of 600^{o}C), but this does not directly lead to overall failure of the system, which is largely attributed to the additional resistance provided by the seven ambient floors above the fire affected floor, therefore, the vertical floor deflection is arrested and then stabilized at approximately 300mm without exceeding the ductility supply offered by joints. The corresponding stabilised deflected shape after column buckling of floor level 1 is illustrated in Figure 30.

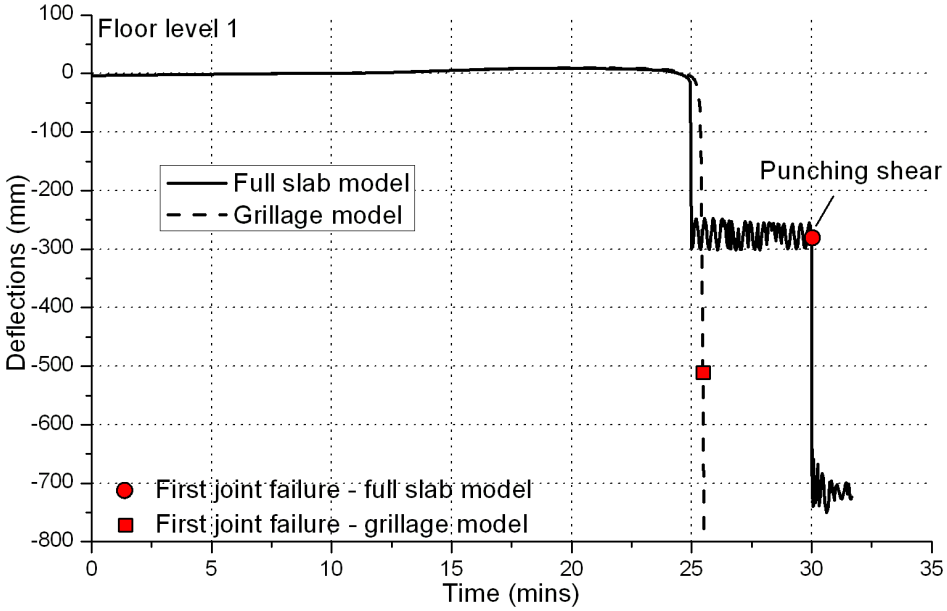

Fig. 28 Column top vertical displacements of floor level 1 in fire

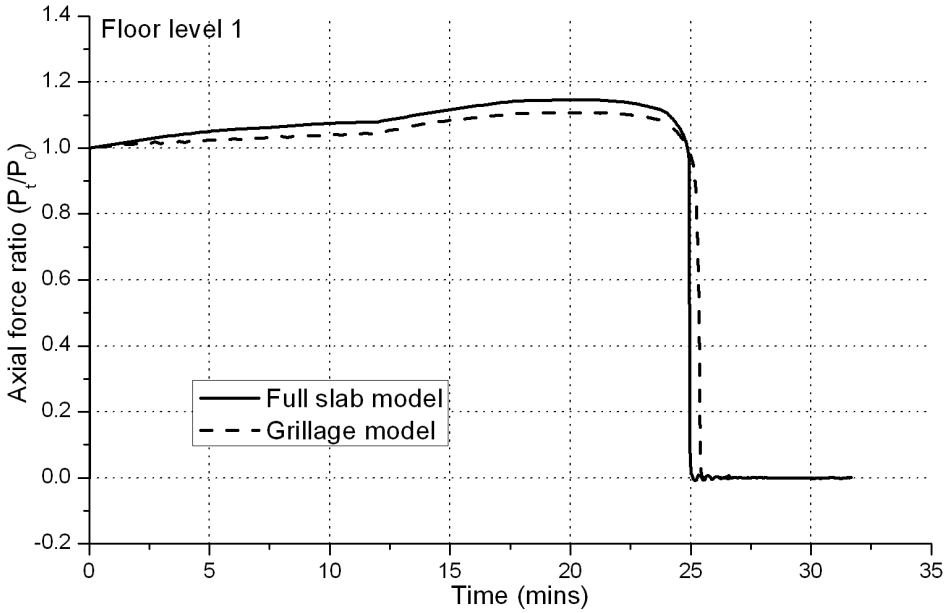

Fig. 29 Column axial forces of floor level 1 in fire

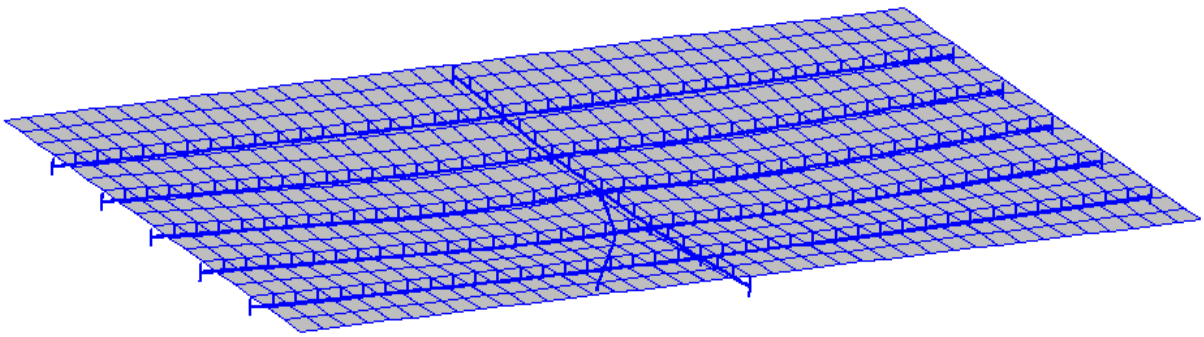

Fig. 30 Deflected shape of floor level 1 at time = 25m00s (full slab model)

However, shear failure (punching shear) of the fire affected beam-to-column joint is observed at a time of 30 minutes. The corresponding failure temperature of the joint is 723.4^{o}C, under which condition the overall shear force resisted by the four beam-to-column steel connections exceeds the overall elevated temperature shear capacity, as shown in Figure 31. The shear force/capacity vs. time relationship shows that before the buckling of the column, the fire affected beam-to-column joint is subjected to significant shear forces, but no shear failure is found due to limited decreasing of their shear capacity below the temperature of column buckling (around 560^{o}C). When the column buckles, the upper ambient floors have sufficient vertical load resistance to 'pull up' the fire affected floor with a stabilized deflection of 300mm, such that in effect the buckled column can be seen as to continue providing the vertical resistance. In this case the shear force transferred to the upper ambient structure through the steel beam-to-column connections stabilizes at around 600kN (but less than the initial ambient value of around 800kN). As the temperature keeps increasing, the shear capacity of the fire affected beam-to-column joint is further reduced, and when it drops below the transferred shear force, first joint failure of the system is triggered by means of punching shear. Initiated by the joint shear failure, the fire affected floor is detached from the upper ambient floors, as shown in Figure 28. The final deflection of the individual fire floor is then arrested at 740mm with sufficient ductility supply provided by the surrounding ambient joints. Since no successive joint failure is observed after the first joint failure, progressive collapse of the structure is prevented.

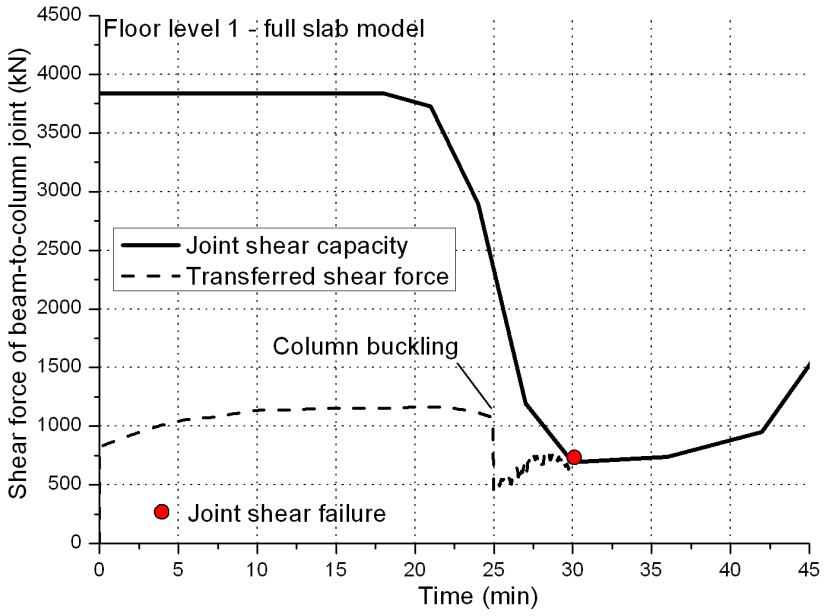

Fig. 31 Shear response of fire affected beam-to-column joint of floor level 1

On the other hand, the grillage model shows a less robust response. Figure 32 illustrates the first failure and the collapse mode of the grillage model subject to the real fire at floor level 1. First joint failure is observed at a time of 25 minutes and 27 seconds in the fire affected major axis beam-to-column joint under sagging moment

along with the buckling of the fire affected column, where the elongation of the lowest bolt-row exceeds the maximum limit of 25mm. Soon afterwards, successive joint failure is directly triggered in the surrounding ambient major axis beam-to-column joints due to the ruptures of reinforcement rebar. This failure mode is a typical 'double-span' failure mechanism which is largely due to the bucking of the fire affected column and insufficient upper ambient floor resistance.

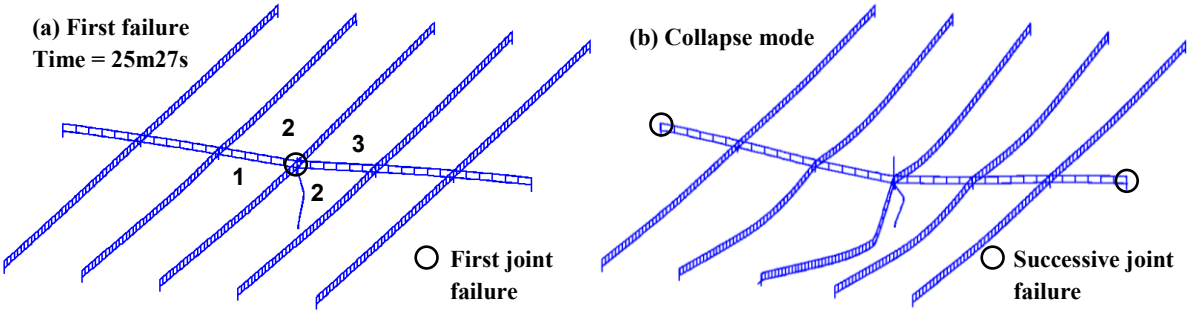

Fig. 32 First failure and post-failure collapse modes of floor level 1 under fire (grillage model)

V.2.2 Fire at floor level 5

The column top vertical displacements and the column axial forces for the grillage model and the full slab model during the considered fire scenario are shown in Figures 33 and 34 respectively. The response of column axial force is represented by the P_t/P_0 ratio, where P_t is the column axial force during the fire and P_0 represents the initial compressive force carried by the column.

With respect to the full slab model, no joint failure is observed at floor level 5 throughout the whole procedure of fire. The fire affected column starts to buckle at a time of 25 minutes and 25 seconds (column temperature of 572^{o}C), while due to sufficient load redistribution capacity of the structural system, a stabilized floor mid-span deflection of about 300mm is maintained. The stabilised deflected shape after column buckling of floor level 5 is illustrated in Figure 35. As the temperature continues to increase, the overall shear capacity of the four beam-to-column steel connections decreases to 18% of the ambient capacity at a time of 30 minutes where a peak temperature is achieved, but no shear failure (punching shear) is observed at the fire affected floor, as predicted in Figure 36. Therefore, sufficient robustness is exhibited of the reference structure subject to fire at floor level 5.

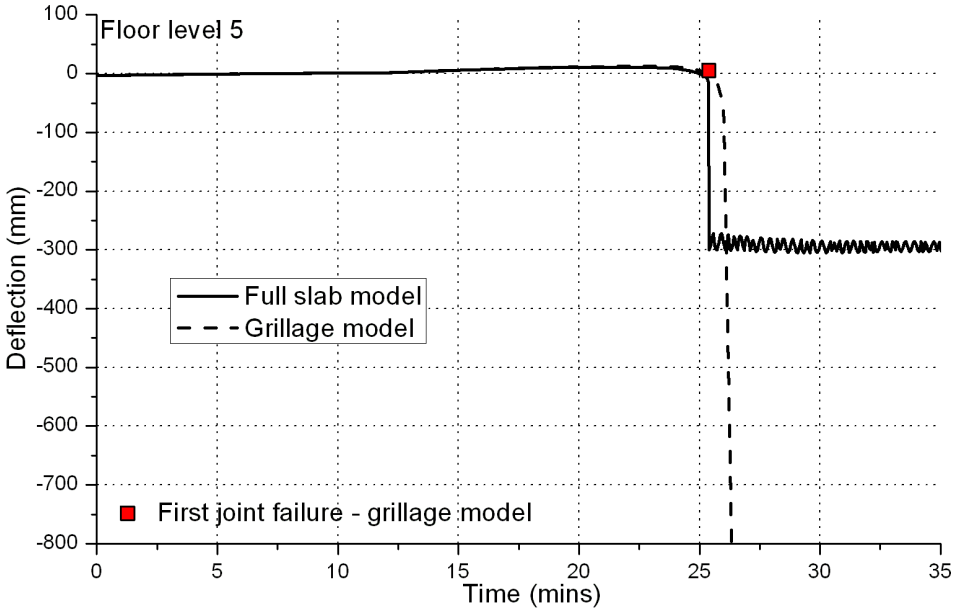

Fig. 33 Column top vertical displacements of floor level 5 in fire

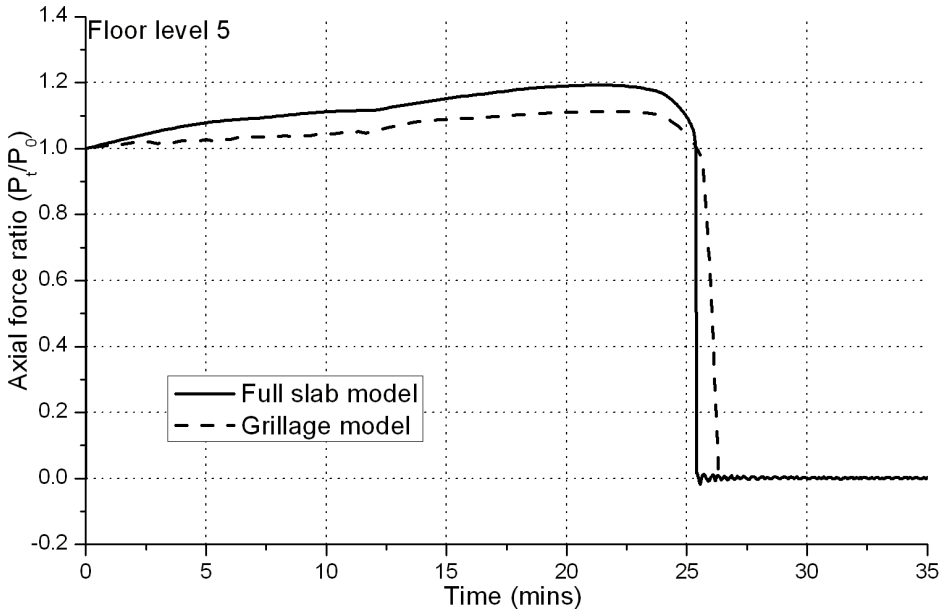

Fig. 34 Column axial forces of floor level 5 in fire

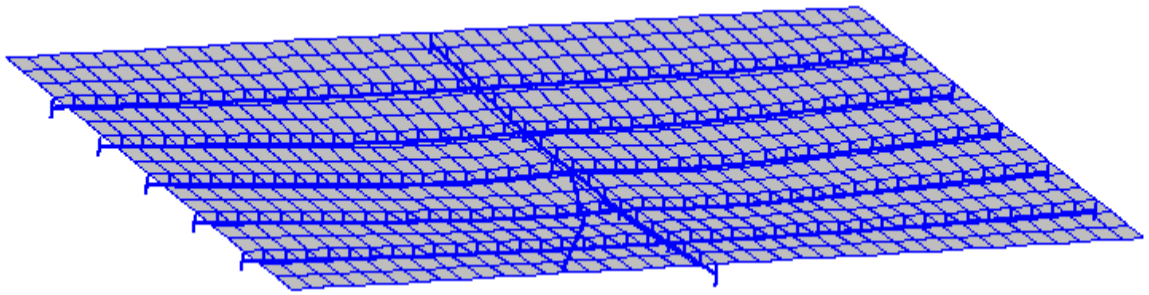

Fig. 35 Deflected shape of floor level 5 at time = 25m25s (full slab model)

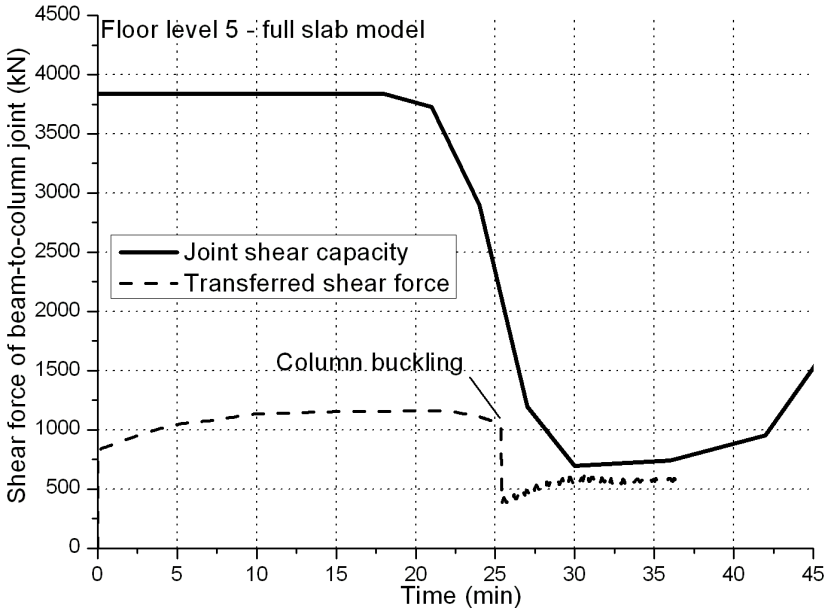

Fig. 36 Shear response of fire affected beam-to-column joint of floor level 5

On the other hand, for the results obtained from the grillage model subject to the fire at floor level 5, a poorer performance is observed. Figure 37 shows the first joint failure and the successive collapse mode of the grillage model. The first joint failure is observed at a time of 25 minutes 20 seconds in the fire affected minor axis beam-to-column joint under hogging moment, where the elongation of the highest bolt-row exceeds the maximum limit of 35mm. This is a typical 'single-span' failure type which is due to insufficient ductility offered by the fire affected joint (subject to a hogging moment) supporting a single-span beam when the supported fire affected column still maintains its resistance. Successive joint failure is found in the ambient minor axis beam-to-column joints located at the other end of the secondary beam, and at the mean time the fire affected column starts to buckle, the structure experiences a total collapse very soon after the first failure has occurred with insufficient ductility supply provided by the surrounding ambient joints. Clearly, the less robust response obtained by the grillage model compared with the full slab model is mainly due to the ignorance of 2D slab effects that can greatly contributes to the vertical resistance of floor systems.

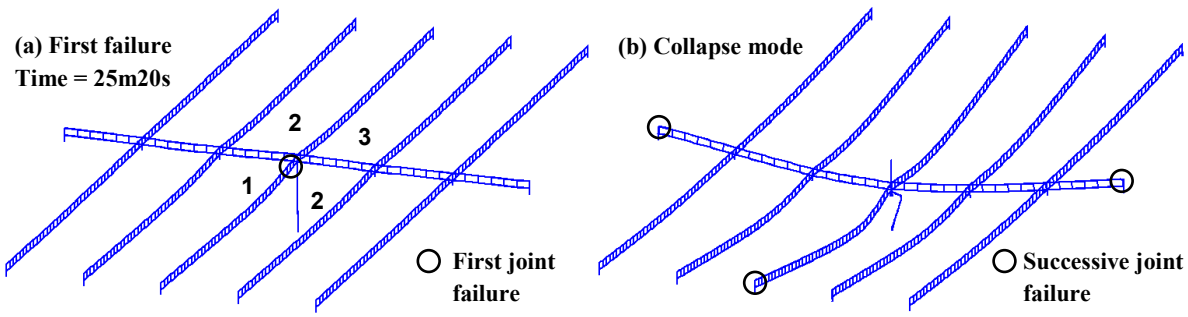

Fig. 37 First failure and post-failure collapse modes of floor level 5 under fire (grillage model)

V.2.3 Fire at floor level 8

The considered sub-structural model for floor level 8 is only comprised of a fire affected floor system without the spring representing upper ambient floors. This is different from the models of the other two fire cases at floor levels 1 and 5 where the resistance offered by the upper ambient floors can be relied on. The deflections and the column axial forces for the grillage model and the full slab model during the considered fire scenario are shown in Figures 38 and 39 respectively. The response of column axial force is represented by the P_t/P_0 ratio, where P_t is the column axial force during the fire and P_0 represents the initial compressive force carried by the column.

For structural response predicted by the full slab model, first joint failure is observed at a time of 27 minute 10 seconds (as shown in Figure 38) in the fire affected major axis beam-to-column joint under sagging moment, which is governed by the 25mm limit of the rupture elongation of the lowest bolt-row (furthest from the compressive centre). It is evident that this first joint failure mode is directly caused by the buckling of the column, and subsequently the fire affected floor system deflects significantly to withstand the vertical loading on its own in double span with the absence of contributions from upper ambient floors. The deflected shape after column buckling of floor level 8 is illustrated in Figure 40. Due to the fact that the HEB220 top floor column is relatively lightly load, the system failure (column buckling) temperature of the floor level 8 is 652°C, which is much higher than the column buckling temperatures of 560°C and 570°C respectively for floor levels 1 and 5 in fire. Importantly, no shear failure (punching shear) is observed in the fire affected beam-to-column joint before column buckling, and this can be explained through Figure 41, where the corresponding transferred shear force and shear capacity are illustrated.

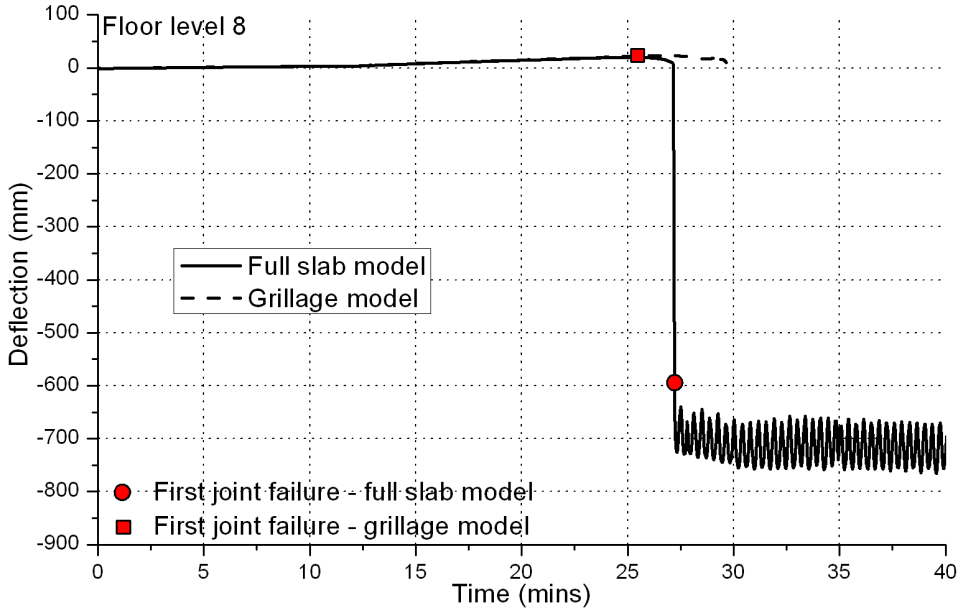

Fig. 38 Column top vertical displacements of floor level 8 in fire

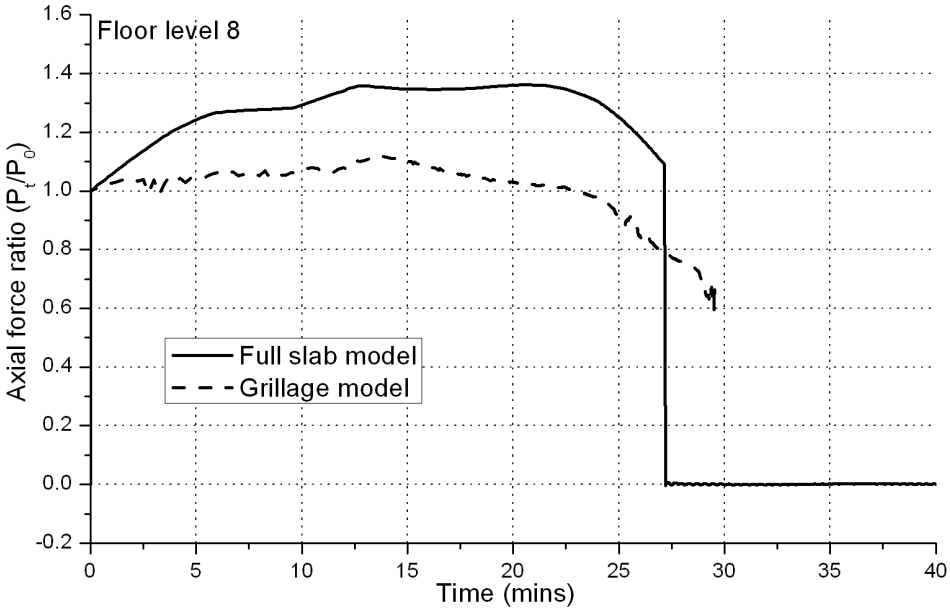

Fig. 39 Column axial forces of floor level 8 in fire

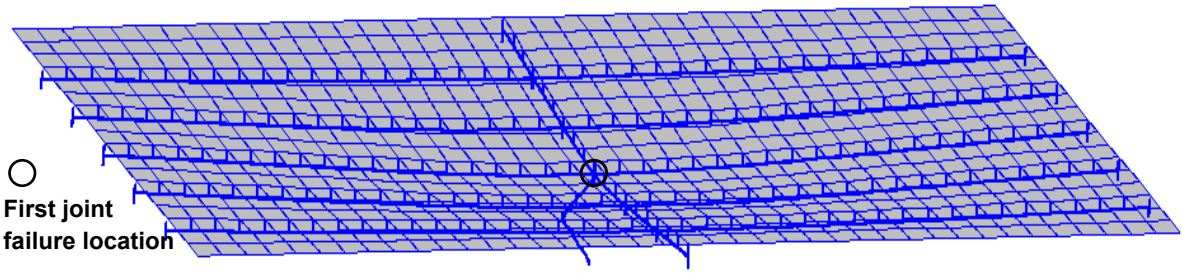

Fig. 40 First failure deflected shape of floor level 8 at time = 26m48s (full slab model)

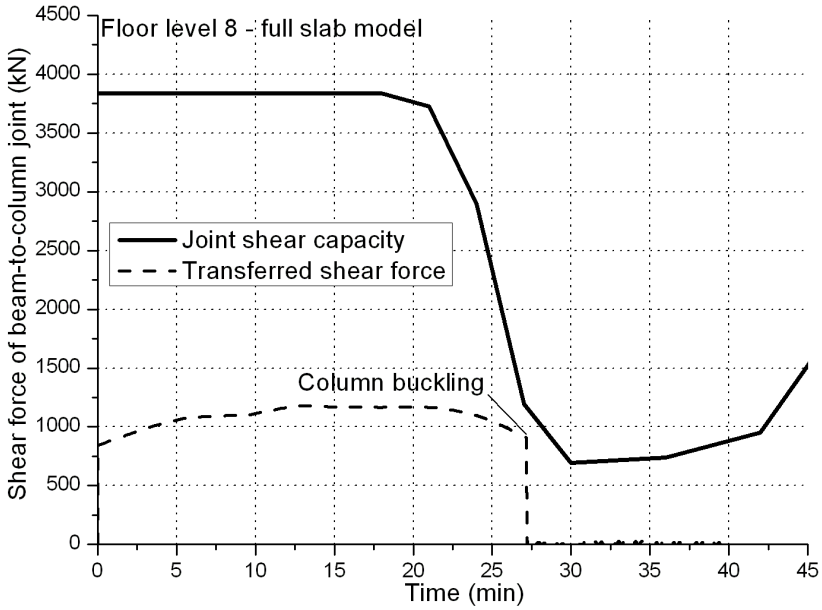

Fig. 41 Shear response of fire affected beam-to-column joint of floor level 8

Despite a complete loss of resistance of the fire affected column, which directly leads to the first failure of fire affected major axis beam-to-column joint, no successive surrounding ambient joint failure is induced in the double-span top floor system bridging over the buckled column, thus the final floor deflection is arrested at around 750mm without triggering progressive collapse. Therefore, sufficient robustness is exhibited of the reference car park subject to localised fire at the top floor when a full slab model is considered.

On the other hand, the grillage model predicts a different first joint failure mode, which occurs in a secondary beam where the fire affected minor axis beam-to-column joint fails under hogging moment associated with the rupture of the highest bolt-row (the elongation exceeds the maximum limit of 35mm), as shown in Figure 42a. Afterwards, successive failure is induced in the ambient minor axis beam-to-column joints located at the other end of the secondary beam (as shown in Figure 42b), thus initiating progressive collapse. No column buckling is observed at the moment of the collapse due to a relatively lightly load resisted by the fire affected column. It should be noted that the collapse stays localised in the failed secondary beam in a 'single-span' typed manner (i.e. the collapse of the secondary beam only). This is clearly attributed to the ignorance of 2D slab effect in grillage models where contributions from adjacent parts of floor slab cannot be relied on.

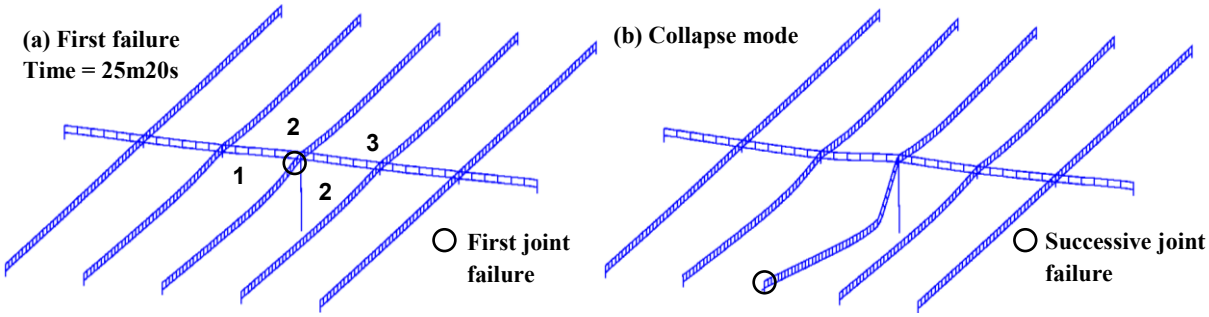

Fig. 42 First failure and post-failure collapse modes of floor level 8 under fire (grillage model)

V.3 Summary of analysis

Three failure types are generally observed for the reference building subject to the selected fire scenarios, namely, the 'single-span failure' type, the 'double-span failure' type and the 'shear failure' type, as illustrated in Figure 43. The single-span failure type usually occurs in the cases when the fire affected column maintains its strength during a fire, or the upper ambient floors can offer sufficient resistance for the fire affected floor system with an acceptably small deflection after the buckling of the column, while the single-span beams are unable to survive due to the failure of the supporting joints. This failure type is only found in the grillage model established in this study.

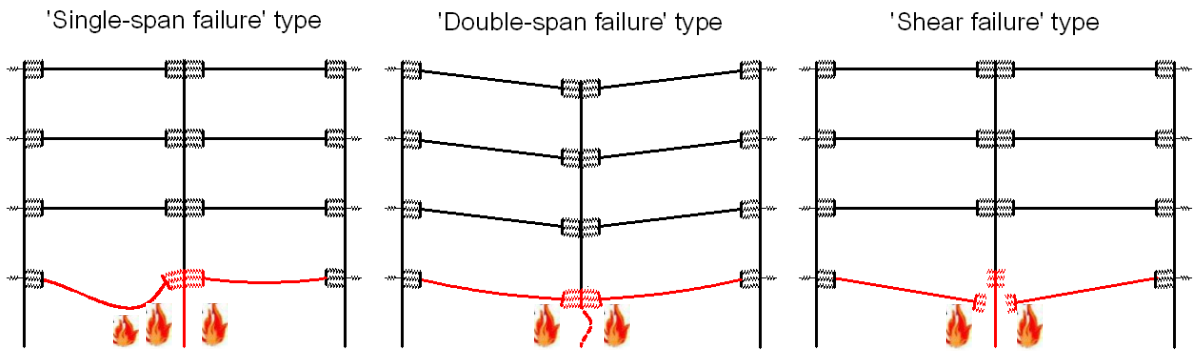

Fig. 43 Typical fire-induced first joint failure types

On the other hand, the ‘double-span failure’ type is associated with the case where the fire affected floor and the upper ambient floors do not have sufficient ductility to redistribute gravity load after the fire affected column is buckled. This failure type is typical for ‘column loss’ scenarios, and is found in both full slab and grillage models considered in this study.

The ‘shear failure’ type is associated with the shear failure of steel connections, and it is normally triggered by the shear failure of the fire affected joint. This failure type can either happen before or after the buckling of the fire affected column, as long as significant shear force is transferred between the column and the connected steel beams. As illustrated in Figure 43, when shear failure occurs, the fire affected floor can be completely detached from the middle supporting and subsequently deflects in a double-span cantilever manner. It should be noted that shear failure may be less easy to occur in real structures, because in this study the shear resistance of joints is predicted conservatively.

Table 8 gives the first failure times, the first failure modes and failure types of the reference structure subject to the considered fire scenarios on the three floors. Judging from the current situation, the full slab models predict a better structural robustness than the grillage models. For example, the floor level 5 grillage model experiences a single-span type failure of the beam above the burning cars 1 and 2 (due to the failure of the highest bolt-row in the double web-cleat connection), whereas no such failure is observed in the full slab model. This is because the composite slab above the steel beams is divided into several separate strips in the grillage models, as shown in Figure 44, and the steel deck and ribs are ignored for the concrete flange in the direction parallel to the secondary beams. Therefore, without the contribution from the adjacent strips, concrete cracks above the fire affected double web-cleat steel connection can directly impair the beam-end rotational stiffness and resistance. But for the full slab models, the overall slab works cooperatively in a 2D manner; hence a larger joint resistance under hogging moment is expected.

Table 8 Structural responses under fire

Structural response	Fire floor levels	Full slab model	Grillage model
Column buckling time	1	24m56s	25m27s
	5	25m25s	26m00s
	8	27m10s	No buckling
First joint failure time	1	30m00s	25m27s
	5	No first joint failure	25m20s
	8	27m10s	25m20s
First joint failure position	1	Fire affected beam-to-column steel connections in shear	Fire affected major axis beam-to-column joint under sagging moment
	5	No first joint failure	Fire affected minor axis beam-to-column joint under hogging moment
	8	Fire affected major axis beam-to-column joints under sagging moment	Fire affected minor axis beam-to-column joint under hogging moment
First joint failure type	1	Shear failure	Double-span
	5	No first joint failure	Single-span
	8	Double-span	Single-span
Progressive collapse triggered after first joint failure?	1	No	Yes
	5	-	Yes
	8	No	Yes
Successive joint failure position triggering progressive collapse	1	Structure safe	Ambient major axis beam-to-column joint under hogging moment
	5	Structure safe	Ambient major axis beam-to-column joint under hogging moment
	8	Structure safe	Ambient minor axis beam-to-column joint under hogging moment

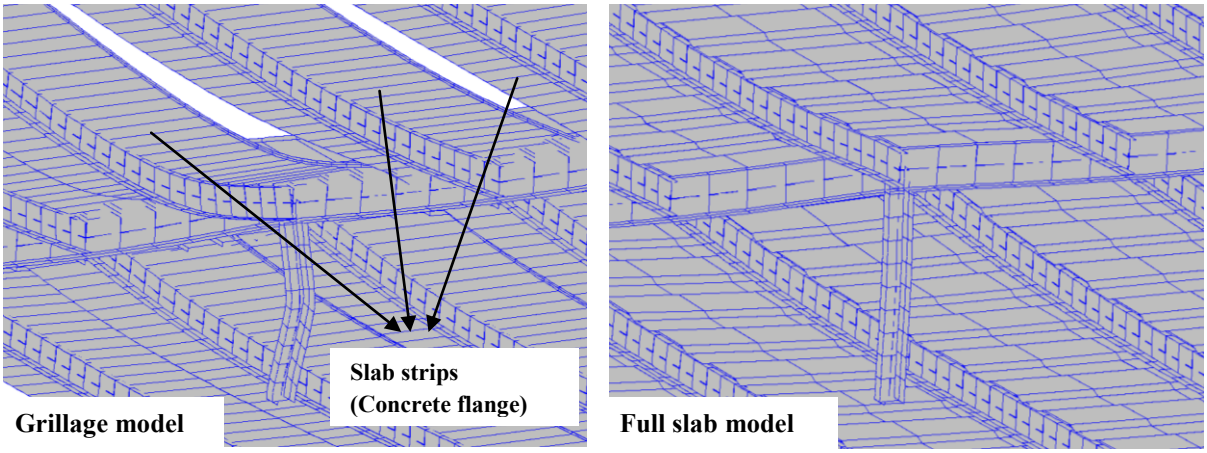

Fig. 44 Full plot view of grillage and full slab models

Finally, it can be seen that structures subject to higher floors in fire have a greater potential for progressive collapse than these with the fire at lower floors, particularly according to the results from the full slab models. For the lower floor levels (i.e. levels 1 and 5), the fire leads to a complete loss of column resistance due to buckling but no immediate overall system failure. In this case, the upper ambient floors offer additional resistance to the fire affected floor, and the vertical floor deflection is thus arrested at around 330mm and 360mm, respectively. While for the top floor, the buckling of the fire affected column can lead to a immediate failure of the whole floor, which is attributed to limited alternative load redistribution capabilities. Therefore, from a robustness perspective, it is recommended that extra care should be taken regarding the fire design of higher floor levels.

VI References

ADAPTIC user manual, Version 1.4, Izzuddin B. A,, 2010, March.

Al-Jabri KS. The behaviour of steel and composite beam-to-column connections in fire. Ph.D. Thesis, University of Sheffield; 1999.

Anderson D., Aribert J.M., Bode H. and Kronenburger, H. J. Design Rotation Capacity of Composite Joints. The Structural Engineer, 2000, 78, No. 6, pp. 25-29.

British Standards Institution. BS 5950: Structural Use of Steelwork in Buildings, Part 8: Code of Practice for Fire Resistance Design, 2003, London, UK.

CEB-FIP Model Code 1990, Lausanne, CEB, 1990

EN 1993-1-1:2005. “Eurocode 3: Design of steel structures - Part 1-1: General rules and rules for buildings”. European committee for standardization, May 2005.

EN 1993-1-2:2005. “Eurocode 3: Design of steel structures – Part 1-2: General rules – Structural fire design”. European committee for standardization, April 2005.

EN 1993-1-8:2005. Eurocode 3: Design of steel structures – Part 1.8: Design of steel structures-Design of joints, European Committee for Standardization, 2005, May.

EN 1994-1-1:2004. “Eurocode 4: Design of composite steel and concrete structures – Part 1-1: General rules and rules for buildings”. European committee for standardization, December 2004.

EN 1994-1-2:2005. “Eurocode 4: Design of composite steel and concrete structures – Part 1-2: General rules – Structural fire design”. European committee for standardization, 2005.

Fu, F., D. Lam, et al. "Moment resistance and rotation capacity of semi-rigid composite connections with precast hollowcore slabs." Journal of Constructional Steel Research 66(3): 452-461.

Gil, B. and E. Bayo (2008). "An alternative design for internal and external semi-rigid composite joints. Part I: Experimental research." Engineering Structures 30(1): 218-231.

Izzuddin, B.A. (1991) Nonlinear Dynamic Analysis of Framed Structures. PhD Thesis. Department of Civil Engineering, Imperial College, University of London, London, UK.

Izzuddin, B.A., and Elnashai, A.S. (1993a) Adaptive Space Frame Analysis – Part I: A Plastic Hinge Approach. Structures and Buildings, Proceedings of the Institution of Civil Engineers, 99, 303-316.

Izzuddin, B.A., and Elnashai, A.S. (1993b) Adaptive Space Frame Analysis – Part II: Distributed Plasticity Approach. Structures and Buildings, Proceedings of the Institution of Civil Engineers, 99, 317-326.

Izzuddin BA, Song L, Elnashai AS, Dowling PJ, An integrated adaptive environment for fire and explosion analysis of steel frames - Part II: verification and application, J CONSTR STEEL RES, 2000, Vol:53, Pages:87-111

Izzuddin, B.A., Tao, X.Y., and Elghazouli, A.Y. (2004) Realistic Modeling of Composite and Reinforced Concrete Floor Slabs under Extreme Loading. Part I: Analytical Method. Journal of Structural Engineering, ASCE, 130(12), 1972-1984.

Izzuddin B.A., Vlassis A.G., Elghazouli A.Y. and Nethercot D.A. (2008). “Progressive Collapse of Multi-Storey Buildings due to Sudden Column Loss – Part I: Simplified Assessment Framework”, Engineering Structures, 30:5, 1308-1318.

Jarrett, N.D. Axial Tests on Beam/Column Connections. BRE Client Report CR 55/90, Building Research Establishment, 1990, Garston, Watford, UK.

Jabri K S, Burgess IW, Plank RJ (2004). Prediction of the degradation of connection characteristics at elevated temperature. J Const Steel Res;60:771–81.

Kirby, B. R. (1995). "The Behaviour of High-strength Grade 8.8 Bolts in Fire." Journal of Constructional Steel Research, 33(1-2), 3-38.

Kuhlmann U, Davison JB, Kattner M. Structural systems and rotation capacity. Proceeding of COST Conference on Control of the Semi-rigid Behaviour of Civil Engineering Structural Connections, Liege, Belgium, 1998. p. 167–76.

Leston-Jones LC. The influence of semi-rigid connections on the performance of steel framed structures in fire. PhD Thesis. University of Sheffield; 1997.

Owens, G.W., and Moore, D.B. The Robustness of Simple Connections. The Structural Engineer, 1992, 70, No.3, pp. 37-46.

Sarraj Marwan (2007). The behaviour of steel fin plate connections in fire. Ph.D. thesis. UK: The University of Sheffield; 2007.

SAFIR. A Thermal/Structural Program Modelling Structures under Fire, Franssen J.-M., Engineering Journal, A.I.S.C., Vol 42, No. 3 (2005), 143-158, http://hdl.handle.net/2268/2928

Ramli-Sulong R. NH. Behaviour of steel connections under fire conditions. Ph.D. thesis. Imperial College London, University of London; 2005.

Ramli-Sulong, N. H., Elghazouli, A. Y. and Izzuddin, B. A. Behaviour and Design of Beam-to-Column Connections under Fire Conditions, Fire Safety Journal, 2007, 42, No.6, pp. 437-451.

Simoes da Silva, L, Santiago A, and Vila Real P. Post-limit Stiffness and Ductility of End-plate Beam-to-column Steel Joints. Computers & Structures, 2002, 80, pp. 515–31.

Song L, Izzuddin BA, Elnashai AS, Dowling PJ, An integrated adaptive environment for fire and explosion analysis of steel frames - Part I: analytical models, J CONSTR STEEL RES, 2000, Vol:53, Pages:63-85

Song L. Integrated analysis of steel buildings under fire and explosion. Ph.D. thesis. Imperial College London, University of London; 1998.

Vlassis A.G., Izzuddin B.A., Elghazouli A.Y. and Nethercot D.A. (2008). “Progressive Collapse of Multi-Storey Buildings due to Sudden Column Loss – Part II: Application”, Engineering Structures, 30:5, 1424-1438.

VII Appendix: Robustness assessment procedure

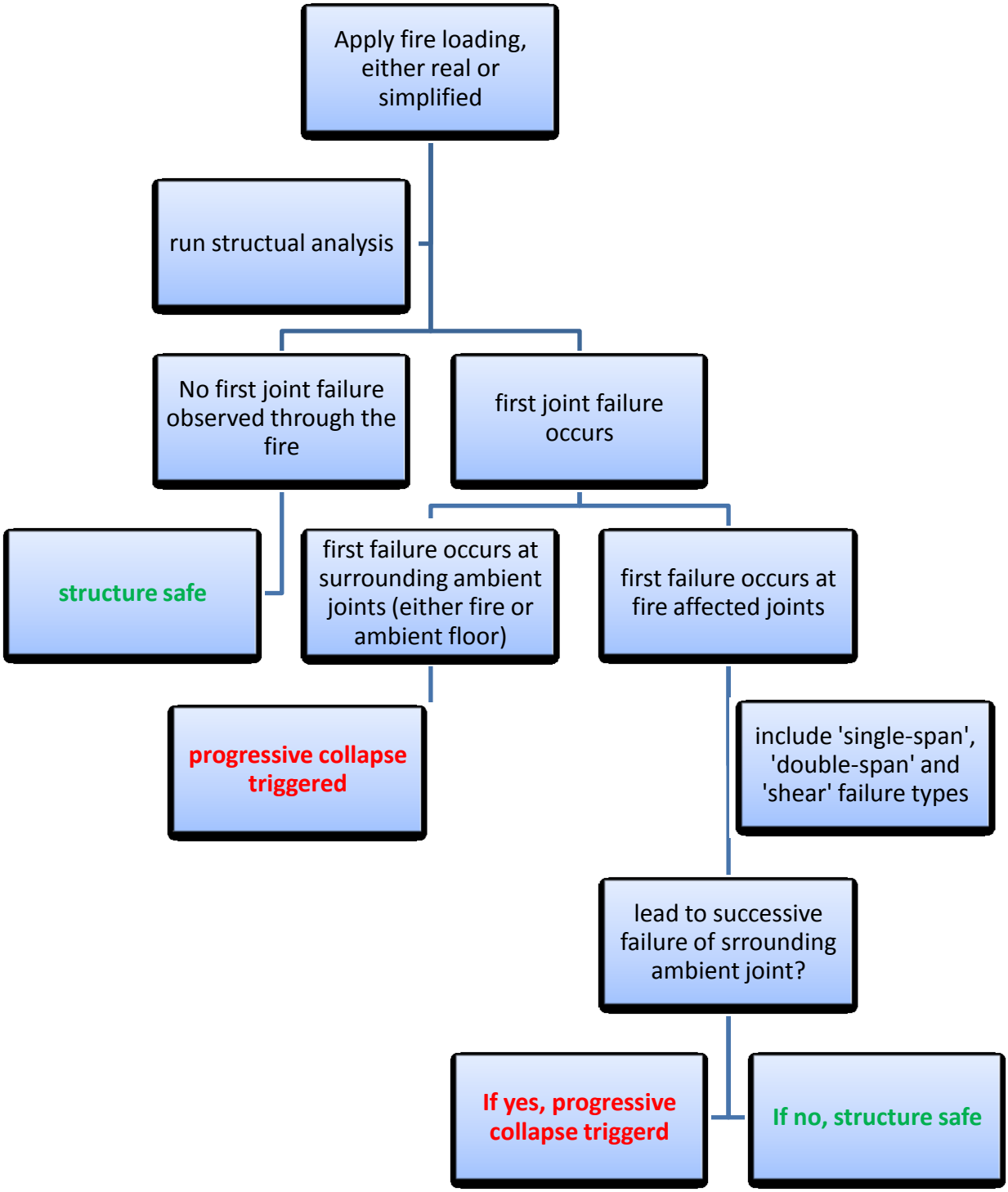

ANNEX C

Faculté des Sciences Appliquées
Département ArGenCo
Secteur MS²F (mécaniques des solides, des fluides et des structures)
Dr. Ir. J.P. JASPART, Professeur
Ir. J.F. DEMONCEAU, Assistant

Liège, the 14th of March 2012

Robustfire project

Global frame analytical model
–
Liège University

Authors:
L. Comeliau
J.-F. Demonceau
C. Huvelle
J.-F. Jaspart

I. Global analytical model 3
I.1. 2D-frame 3
I.1.1. Introduction 3
I.1.2. Substructure 5
I.1.3. Equations related to the substructure 6
I.2. Plasticization of the indirectly affected part 12
I.2.1. Introduction 12
I.2.2. Application of the step-by-step procedure 12
I.3. 3D-frame 19
I.4. Application of the global model to the investigated car park 21
I.4.1. Specificities and simplifications 21
I.4.2. Equations in 2D 22
I.4.3. Equations in 3D (2*2D) 23
II. References 25

I. Global analytical model

Within the present section, a global analytical model able to predict the response of a structure further to a column loss will be first introduced. Then, this model will be adapted to the scenario investigated within this project, i.e. the loss of a column in a parking structure further to a localised fire. In particular, the main assumptions leading to a simplification of the global model will be reflected.

The global concept will be first introduced on a 2D frame, and then generalised to a 3D frame.

The aim of the global model is to determine the displacements and efforts in the whole structure when the column is completely disappeared, i.e. at the end of the considered scenario. Knowing these efforts and displacements in the structure at this stage, it is possible to verify if the structure is robust or not, by checking, on one hand, ductility conditions (can the joints sustain such rotations?,...) and on the other hand, resistance conditions for key-elements (can the columns next to the lost one sustain the additional compression?,...).

To achieve this goal, a substructure is extracted from the entire structure. The influence of the rest of the structure is considered by inserting horizontal springs in the so-extracted simplified substructure.

I.1. 2D-frame

I.1.1. Introduction

In this part, the beneficial effects of the slab are not considered. The study is focusing on frames only composed with columns and beams. No dynamics effects are considered as the considered scenario does not induce such effects and the method is for ambient temperature. It will be explained later on how this model can be applied to parking affected by a localised fire.

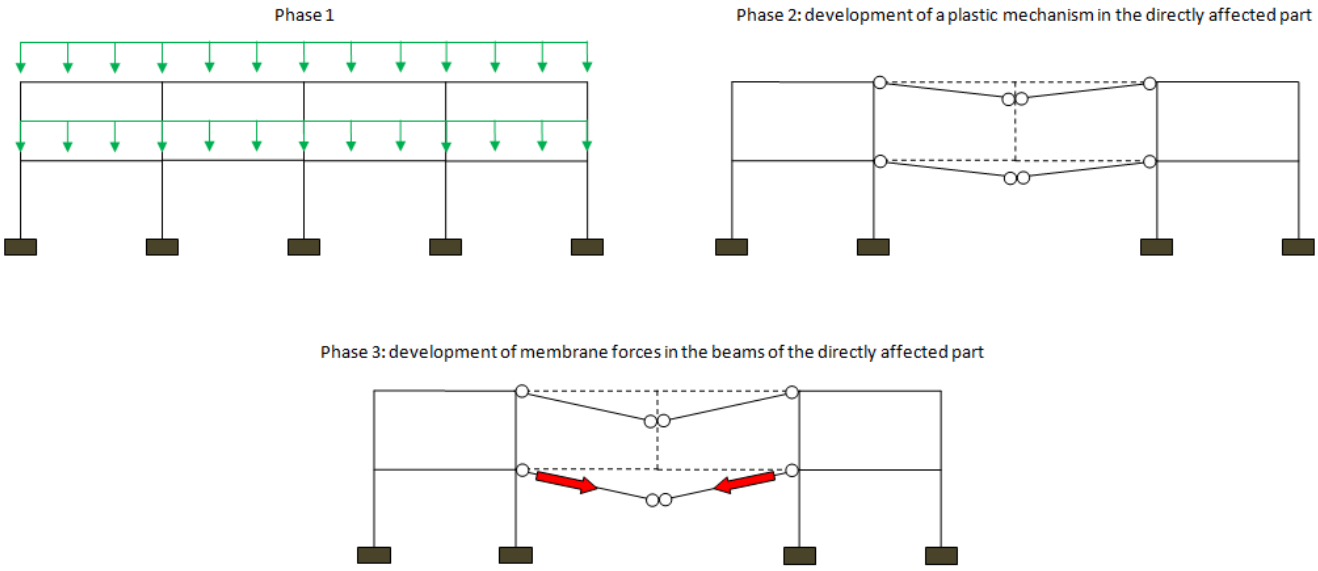

Figure 1. Phases during a column loss in a frame

When a 2D frame still has its column, the frame is normally loaded (phase n°1 on Figure 1); the column which will be lost is supporting a compression load N_0. For phase 1, it is equivalent to consider the entire frame submitted to its normal loads (Figure 2 on the left) and to consider the same frame, without one of its column, submitted to the uniformly distributed loads and to a force N_0 going upward (Figure 2 on the right).

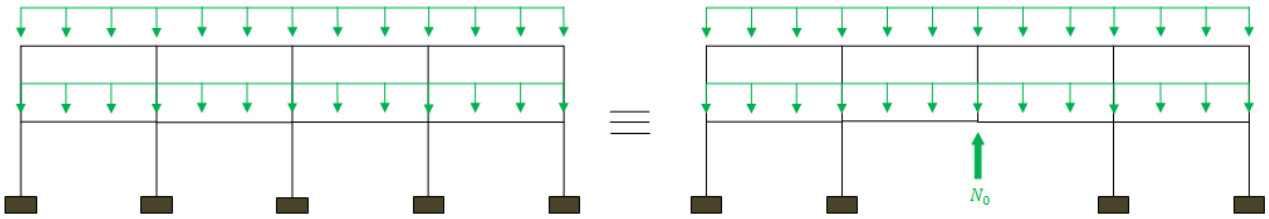

Figure 2. Lost column replaced by $\boldsymbol{N_0}$

To simulate the loss of the column, a concentrate load Q, going downwards (Figure 3) is introduced. This force Q increases as the column disappears, and the column is totally removed when $Q = N_0$.

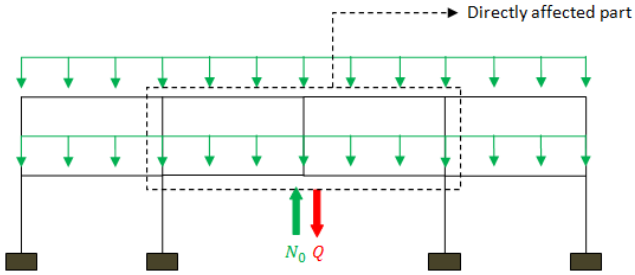

Figure 3. Force Q simulating the column loss

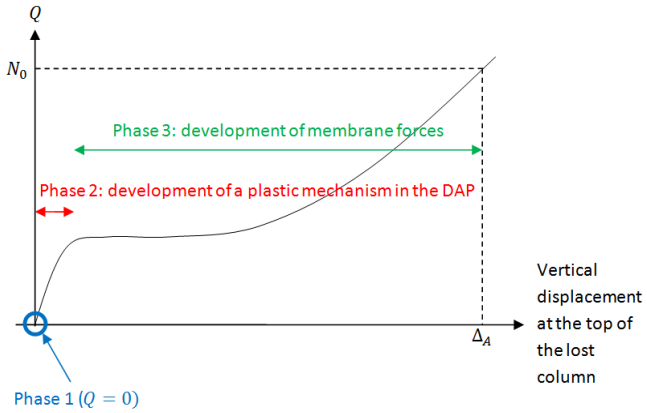

Figure 4. $\boldsymbol{Q - \Delta_A}$ curve

When the column is progressively removed (i.e. Q increases), the directly affected part (see Figure 3) begins to deform. During the column removal, two phases are identified:

- Phase 2, which is developing from $Q = 0$ to $Q = Q_{pl}$, which corresponds to the formation of a plastic mechanism in the directly affected part
- Phase 3, which starts at $Q = Q_{pl}$ and ends at $Q = N_0$, i.e. when the column is fully removed

It is only possible to reach the end of phase 3, i.e. $Q = N_0$, if:

- the loads which are reported from the directly affected part to the rest of the structure do not induce the collapse of elements in the latter (for instance, buckling of the columns or formation of a plastic mechanism);
- the compression loads which may appear in the upper beams of the directly affected part associated to an "arch" effect, do not lead to the buckling of the latter;
- if the different structural elements possess a sufficient ductility to reach the vertical displacement corresponding to point (5).

It is also possible that the complete removal of the column is reached (i.e. $N_0 = Q$) before reaching phase 3.

During Phase 3, as a plastic mechanism has formed in the directly affected part, the first order stiffness of the structure is equal to zero and so, large displacements occur. Due to these large displacements, significant membrane forces develop in the beams of the directly affected part, which are associated to second order effects.

To predict the behaviour of the structure during phase 1 and 2 is easy as usual methods of analysis can be used. However, during phase 3, the analysis of the frame and the prediction of its response become difficult as significant second order effects are developing.

The objective with the developed analytical procedure is to be able to predict the response of the frame during phase 3. In particular, the object is to determine the displacement Δ_A (the vertical displacement at the top of the lost column) when Q reaches the value of N_0, i.e. when the column has totally disappeared (Figure 4). Knowing this value of Δ_A, it is possible to determine:

- the requests in terms of deformation capacity for the structural elements
- the load distribution within the structure and so, to check the structural member resistance

I.1.2. Substructure

In the analytical model, only the force Q going downwards in considered (Figure 5), because provided that the uniformly distributed loads acting on the beams are not too important (which is generally the case), it has been demonstrated [1] that the influence of these loads is negligible.

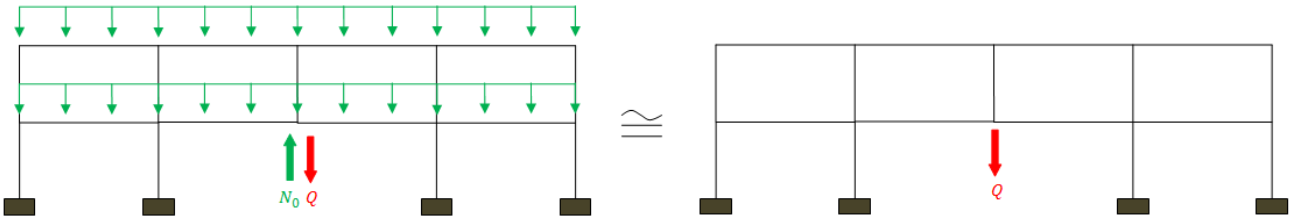

Figure 5. Simplification in the loads acting on the structure

As can be seen in Figure 6, the studied substructure is composed of all the stories of the directly affected part. The indirectly affected part composed of the rest of the structure is replaced by horizontal springs, representing the lateral anchorage leading to the development of membrane forces. As the developed method is used to predict the structural response during phase 3, i.e. when a plastic mechanism is formed in the directly affected part, this substructure is studied through a rigid-plastic analysis.

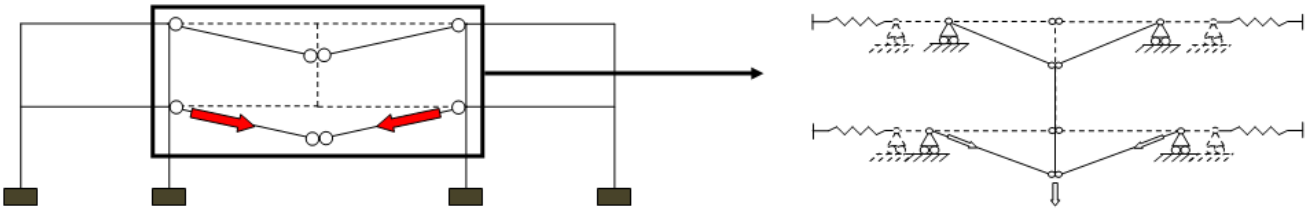

Figure 6. Extraction of the substructure

Within the present project, the substructure model has been improved if compared to the one develop in the framework of the previous project "Robustness" ([2], see also [1]). Indeed, in [2] and [1], the substructure was composed of only one storey of the directly affected part (Figure 7), and this because it is in this double-beam that the biggest tension forces develop. Moreover, it was then assumed that the compression effort in the column just above the lost one was constant during the phase 3 ([2]). It appeared [5] that this hypothesis was not true in all circumstances; it is the reason why it was decided to develop a new substructure.

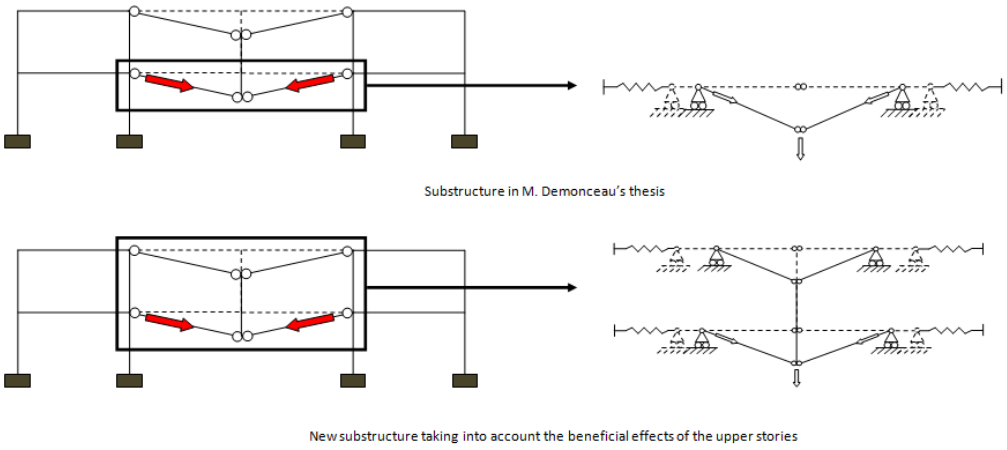

Figure 7. Evolution in the definition of the substructure

Indeed, if a very high building is considered (Figure 8), when a column of the ground floor is lost, an arch effect is developing. This arch effect leads to a greater stiffness, and the part just above the lost column is literally "suspended" on this newly developed arch. So, the effort in the column above the lost one will progressively move from compression to tension. It is as if there was a vertical spring missing in the substructure developed in ([2]), spring that would represent the additional stiffness brought by the upper stories of the directly affected part.

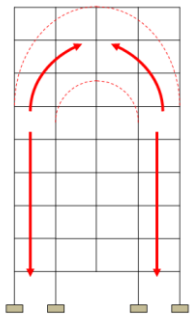

Figure 8. Arch effect

In the substructure containing all the stories of the directly affected part, it is possible to detect a compression force growing in the upper beams of the directly affected part, which was not possible in the previous version of the substructure.

I.1.3. Equations related to the substructure

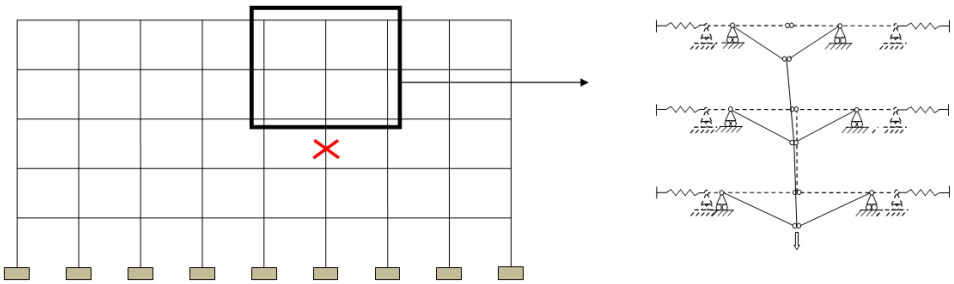

Figure 9. Example for the analytical method

Within the present section, the equations needed to predict the so-defined substructure during phase 3 are presented.

These equations are related to two distinct parts of the frame: the directly affected part (above the lost column) and the indirectly affected part (beside the directly affected part).

Equations coming from the directly affected part

- Elementary block (one storey)

To explain the origin of the equations, only one storey will be considered at first, as shown in Figure 10 (the notations are summarized in Table 1.

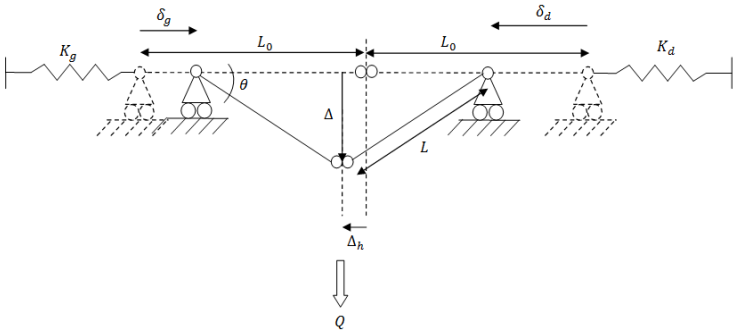

Figure 10. Substructure - one storey

Table 1. Table of notations

Symbol	Signification
Q	Total load applied on the structure, load that simulates the column loss
N_0	Compression effort in the lost column before its disappearance
$\Delta\ (\equiv \Delta_A)$	Vertical displacement of the point at the top of the lost column
Δ_h	Horizontal displacement of the point at the top of the lost column
N	Axial force in the beams of the directly affected part
M_{HOG}	Bending moment in hogging in the hinge in the directly affected part
M_{SAG}	Bending moment in sagging in the hinge in the directly affected part
L_0	Initial length of the beams in the directly affected part
L	Length of the beams in the directly affected part, taking into account their elongations δ_N
δ_d, δ_g	Horizontal displacements at the extremities of the directly affected part (δ_d is for the right extremity, δ_g is for the left one)
F_h	Horizontal force acting on the indirectly affected part, coming from the development of membrane forces in the directly affected part
δ_N	Axial elongation of one plastic hinge
K_N	Axial stiffness of one plastic hinge
$s_{g,ij}, s_{d,ij}$	Terms of the lateral stiffness matrix of the indirectly affected part $s_{g,ij}$ is the horizontal displacement of the left part of the indirectly affected part at the storey n°j when a horizontal force of 1 kN is acting on the storey n°i $s_{d,ij}$ is the same, for the right part of the indirectly affected part

– Equilibrium of the forces (Figure 11)

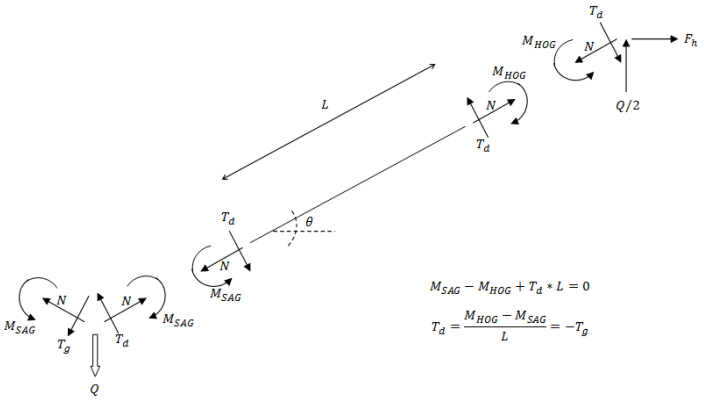

Figure 11. Internal forces in the substructure

$$Q = 2 * N * \sin\theta + 2 * \frac{M_{HOG} - M_{SAG}}{L} * \cos\theta \quad (1)$$

$$N = F_h * \cos\theta + \frac{Q}{2} * \sin\theta \quad (2)$$

– Displacement compatibility (Figure 10)

$$\tan\theta = \frac{\Delta}{L_0 - \frac{\delta_d + \delta_g}{2}} \quad (3)$$

$$L = \sqrt{\left(L_0 - \frac{\delta_d + \delta_g}{2}\right)^2 + \Delta^2} \quad (4)$$

$$L = L_0 + \delta_{N,SAG}(N) + \delta_{N,HOG}(N) \quad (5)$$

$$\Delta_h = \frac{\delta_d - \delta_g}{2} \quad (6)$$

– M-N interaction

$$M_{HOG} = f(N) \ (7)$$
$$M_{SAG} = f(N) \ (8)$$

– $\delta_N - N$ law

$$\delta_{N,SAG} = f(N) \ (9)$$
$$\delta_{N,HOG} = f(N) \ (10)$$

- Assembly of several blocks (multiple stories)

For the case of a number of stories equal to n_{st}, the elementary block described here above has to be considered n_{st} times. All the 10 equations developed are of course still valid for each block, and compatibility equations between these blocks have to be added to the system (Figure 12).

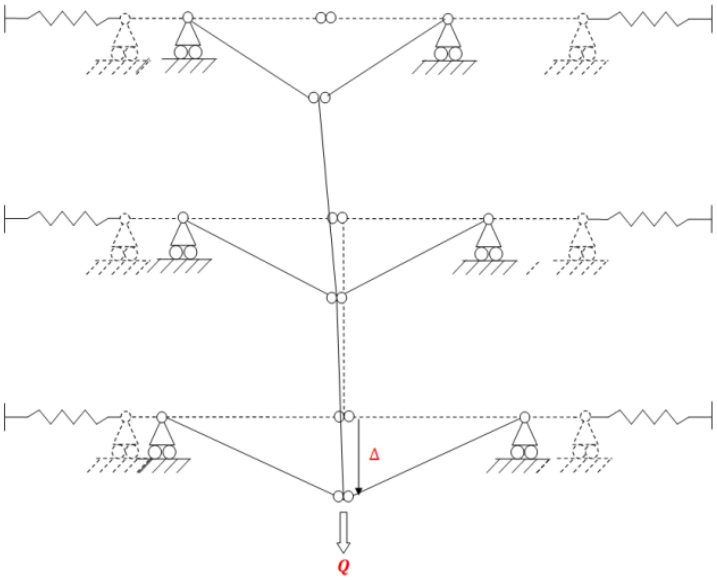

Figure 12. Assembly of multiple "blocks"

$$Q = Q_1 + Q_2 + \cdots + Q_{n_{st}}$$

$$\Delta = \Delta_1 = \Delta_2 = \cdots = \Delta_{n_{st}}$$

Q is the total force applied to the substructure, while Q_i is the part of that force supported by the storey n°i. In terms of displacements, all the stories have the same vertical displacement, equal to Δ (it is assumed here that the elongation of the column just above the lost one can be neglected).

Equations coming from the indirectly affected part

The equations coming from the indirectly affected part are displacement compatibility equations. Indeed, the displacements δ_g and δ_d at each storey are common to the directly affected part and to the indirectly affected one. So, the following equations can be written, for a number of stories equal to n_{st}:

$$\delta_{g,n_{st}} = s_{g,1,n_{st}} * F_1 + s_{g,2,n_{st}} * F_2 + \cdots + s_{g,n_{st},n_{st}} * F_{n_{st}} \qquad \delta_{d,n_{st}} = s_{d,1,n_{st}} * F_1 + s_{d,2,n_{st}} * F_2 + \cdots + s_{d,n_{st},n_{st}} * F_{n_{st}}$$

$$\cdots \qquad \cdots$$

$$\delta_{g,2} = s_{g,1,2} * F_1 + s_{g,2,2} * F_2 + \cdots + s_{g,n_{st},2} * F_{n_{st}} \qquad \delta_{d,2} = s_{d,1,2} * F_1 + s_{d,2,2} * F_2 + \cdots + s_{d,n_{st},2} * F_{n_{st}}$$

$$\delta_{g,1} = s_{g,1,1} * F_1 + s_{g,2,1} * F_2 + \cdots + s_{g,n_{st},1} * F_{n_{st}} \qquad \delta_{d,1} = s_{d,1,1} * F_1 + s_{d,2,1} * F_2 + \cdots + s_{d,n_{st},1} * F_{n_{st}}$$

This represents a total of $2 * n_{st}$ equations.These equations express the presence of the horizontal springs in the substructure, taking into account the fact that these springs are coupled to each other (the displacement at the storey n°j does not only depend on the force F_{hj} acting at this storey)

Determination of the s_{ij} terms: the values of s_{ij}, for the left and right parts, are the term of the "flexibility matrix" of the indirectly affected part, and they are easily determined through first order elastic analyses as follows.

To determine the terms $s_{g,1,i}$ and $s_{d,1,i}$, a force $F = 1\ kN$ is applied at the first storey of the directly affected part (Figure 13). The terms $s_{g,1,i}$ and $s_{d,1,i}$ are the horizontal displacements of the extremities of the directly affected part under this solicitation.

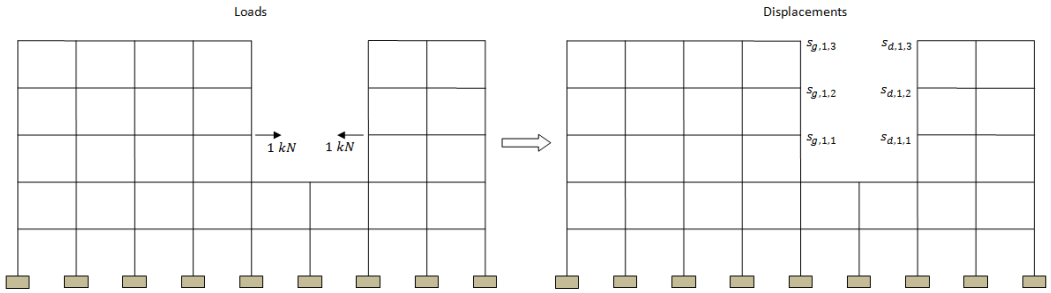

Figure 13. Determination of s_{ij} (1)

In the same way, to determine the terms $s_{g,2,i}$ and $s_{d,2,i}$, a force $F = 1\ kN$ has to be applied at the second storey of the directly affected part (Figure 14). The terms $s_{g,2,i}$ and $s_{d,2,i}$ are the horizontal displacements of the extremities of the directly affected part under this solicitation.

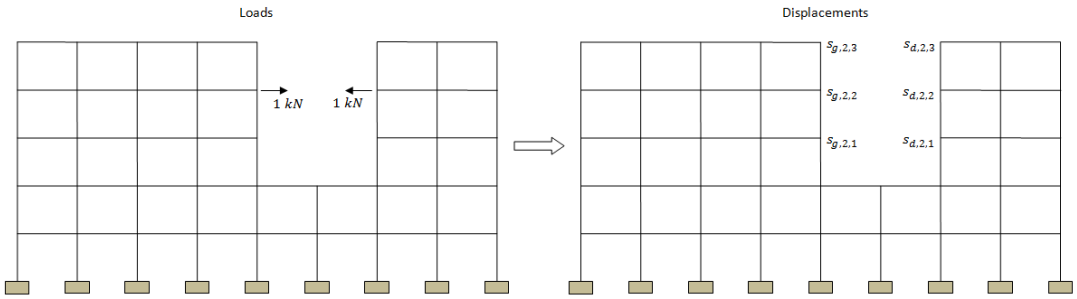

Figure 14. Determination of s_{ij} (2)

And so on for the other s_{ij} terms.

Summary

Unknowns and available equations

Unknowns		Equations	
Q	1	$\Delta = fixed\ value$	1
Δ	1	$Q = Q_1 + Q_2 + \cdots + Q_{n_{st}}$	1
Q_i	n_{st}	$\Delta = \Delta_1 = \Delta_2 = \cdots = \Delta_{n_{st}}$	n_{st}
N_i	n_{st}	$Q_i = 2 * N_i * \sin\theta_i + 2 * \frac{M_{HOG_i} - M_{SAG_i}}{L_i} * \cos\theta_i$	n_{st}
$M_{HOG,i}$	n_{st}	$N_i = F_{h,i} * \cos\theta_i + \frac{Q_i}{2} * \sin\theta_i$	n_{st}
$M_{SAG,i}$	n_{st}	$\tan\theta_i = \frac{\Delta_i}{L_0 - \frac{\delta_{d,i} + \delta_{g,i}}{2}}$	n_{st}
$\delta_{N,SAG,i}$	n_{st}	$L_i = \sqrt{\left(L_0 - \frac{\delta_{d,i} + \delta_{g,i}}{2}\right)^2 + \Delta_i^2}$	n_{st}
$\delta_{N,HOG,i}$	n_{st}	$L_i = L_0 + \delta_{N,SAG,i} + \delta_{N,HOG,i}$	n_{st}
θ_i	n_{st}	$\Delta_{h,i} = \frac{\delta_{d,i} - \delta_{g,i}}{2}$	n_{st}
$F_{h,i}$	n_{st}	$M_{HOG,i} = f(N_i)$	n_{st}
L_i	n_{st}	$M_{SAG,i} = f(N_i)$	n_{st}
$\Delta_{h,i}$	n_{st}	$\delta_{N,SAG,i} = f(N_i)$	n_{st}
Δ_i	n_{st}	$\delta_{N,HOG,i} = f(N_i)$	n_{st}
$\delta_{g,i}$	n_{st}	$\delta_{g,n_{st}} = s_{g,1,n_{st}} * F_{h1} + s_{g,2,n_{st}} * F_{h2} + \cdots + s_{g,n_{st},n_{st}} * F_{hn_{st}}$ ... $\delta_{g,2} = s_{g,1,2} * F_{h1} + s_{g,2,2} * F_{h2} + \cdots + s_{g,n_{st},2} * F_{hn_{st}}$ $\delta_{g,1} = s_{g,1,1} * F_{h1} + s_{g,2,1} * F_{h2} + \cdots + s_{g,n_{st},1} * F_{hn_{st}}$	n_{st}
$\delta_{d,i}$	n_{st}	$\delta_{d,n_{st}} = s_{d,1,n_{st}} * F_{h1} + s_{d,2,n_{st}} * F_{h2} + \cdots + s_{d,n_{st},n_{st}} * F_{hn_{st}}$ ... $\delta_{d,2} = s_{d,1,2} * F_{h1} + s_{d,2,2} * F_{h2} + \cdots + s_{d,n_{st},2} * F_{hn_{st}}$ $\delta_{d,1} = s_{d,1,1} * F_{h1} + s_{d,2,1} * F_{h2} + \cdots + s_{d,n_{st},1} * F_{hn_{st}}$	n_{st}
Total=	$13 * n_{st} + 2$	Total=	$13 * n_{st} + 2$

Input data's:

- L_0, the initial length of the beams
- The matrix of rigidity of the indirectly affected part (terms $s_{d,i,j}$ and $s_{g,i,j}$)(paragraph 0)
- The $M - N$ interaction law, in both hogging and sagging. If the hinge occurs in the beam, then it is the M-N resistant interaction curve of a steel or composite section. If the hinge occurs in the joint, then it is the M-N resistant interaction curve of the joint (more details are available in Deliverable 3)

– The law between $\delta_{N,SAG}$ and N and the law between $\delta_{N,HOG}$ and N. These laws cannot be, at this stage of the developments, determined analytically. They are assumed to be linear (as highlighted through numerical simulations), so that $K_N * \delta_N = N$. The development of an analytical procedure for the prediction of this law constitutes a perspective to the present project.

Solving procedure

For a given value of Δ, and since the number of unknowns is equal to the number of equations, this equations system can be solved (for instance, using MATLAB), and the value of Q corresponding to the given value of Δ can finally be obtained.

I.2. Plasticization of the indirectly affected part

I.2.1. Introduction

If the indirectly affected part is assumed to be indefinitely elastic, then the lateral support provided by this part of the structure to the membrane forces that occur in the directly affected part stays constant.

If this indirectly affected part is supposed to plasticize, then the lateral anchorage of the membrane forces decreases and so, membrane forces cannot be so developed. The result is that vertical displacements are greater, which is dangerous for the structure (higher need in terms of ductility and higher loads reported in the rest of the structure).

At the end, a plastic mechanism can be reached in the indirectly affected part (Figure 15).

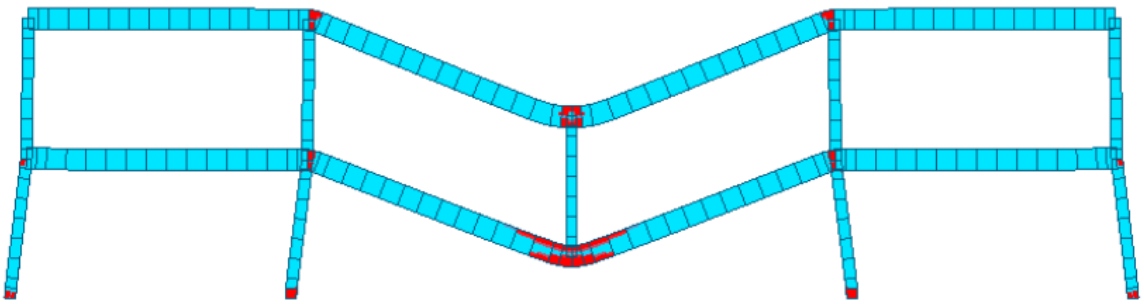

Figure 15. Panel plastic mechanism in the indirectly affected part

A way to take into account the loss of lateral anchorage is to follow, step by step, the development of hinges in the indirectly affected part under the effect of membrane forces. This step-by-step procedure has been developed in [5], and is still under investigation. An example of application of this procedure is given in here below

I.2.2. Application of the step-by-step procedure

This step-by-step procedure will be based on the following simple example (Figure 16):

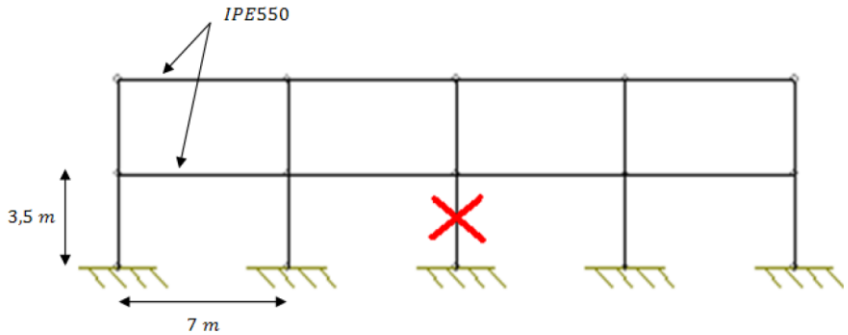

Figure 16. Example for the step-by-step procedure

Particular attention must be paid to the efforts in some "critical sections" of the indirectly affected part. These critical sections are, as can be seen in Figure 15, the extremities of the columns in the indirectly affected part. Moreover, the extremities of the beams must also be observed. Indeed, when a horizontal force is acting on the indirectly affected part, it induces important bending moment in the columns, but also in the beams. These bending moments add to the moments due to the gravitational forces (Figure 17).

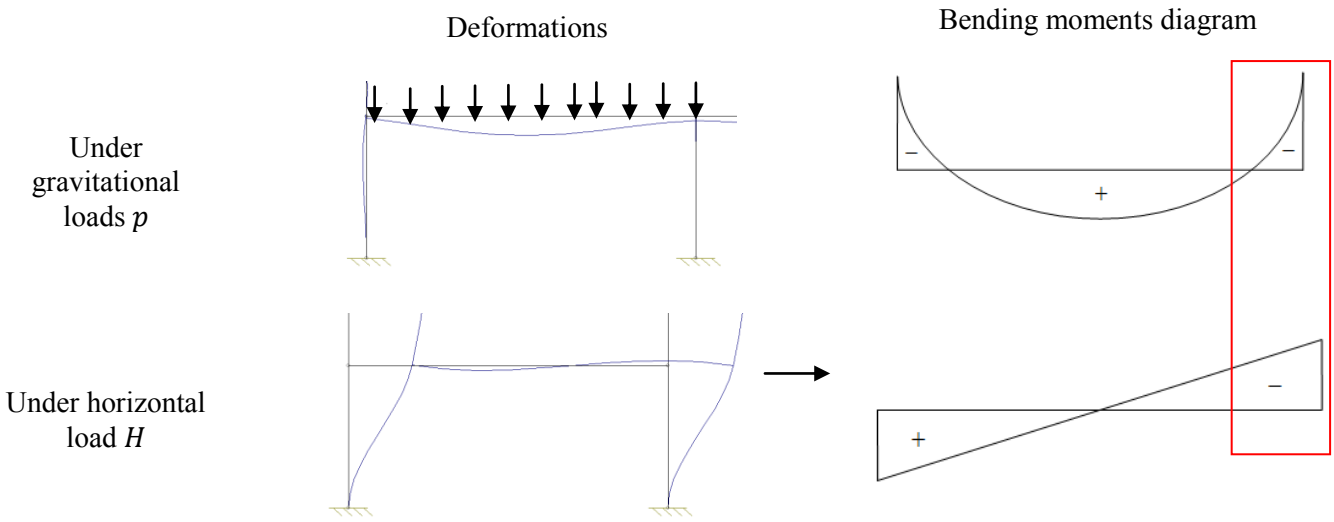

Figure 17. Bending moments in the beams of the indirectly affected part

So, the critical sections that will be studied are the following (Figure 18):

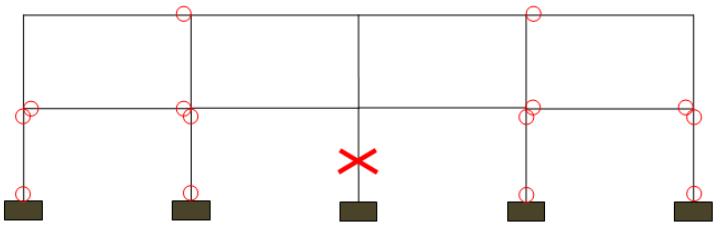

Figure 18. Critical sections in the indirectly affected part

0. Step 0: at the end of phase 2, all the efforts and displacements in the structure are known and can be obtained analytically [3].
1. Step 1:
   1.1. determine the value of $s_{d,ij}$ and $s_{g,i,j}$ considering that there is no plastic hinges in the indirectly affected part:

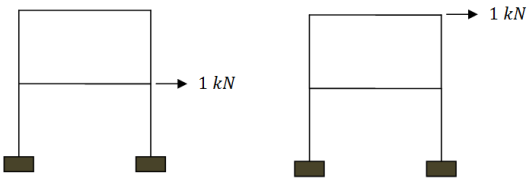

Figure 19: Determination of the stiffness matrix of the indirectly affected part (left part represented)

The stiffness matrix of the indirectly affected part is obtained (here, as the structure is symmetrical, $s_{g,i,j}$ and $s_{d,ij}$ are equal):

$$\delta_{h1} = \frac{0.0238}{1000} * F_{h1} + \frac{0.0337}{1000} * F_{h2}$$

$$\delta_{h2} = \frac{0.0337}{1000} * F_{h1} + \frac{0.0823}{1000} * F_{h2}$$

1.2. solve the equations developed in paragraph I.1.3 with these value of $s_{d,ij}$ and $s_{g,i,j}$

1.2.1. obtain the curves $Q - F_{h1}$ and $\Delta_A - F_{h1}$

1.2.2. obtain the ratios between F_{h1} and F_{h2}, F_{h1} and F_{h3}, F_{h1} and $F_{h\dots}$, F_{h1} and $F_{hn_{st}}$. Here, when the system of equations is solved, the unique ratio to know is $\frac{F_2}{F_1}$, which is equal to 0.4282

1.3. solve the indirectly affected part submitted to $F_{h1} = 1\ kN$ and F_{hi} determined at the precedent step 1.2.2:

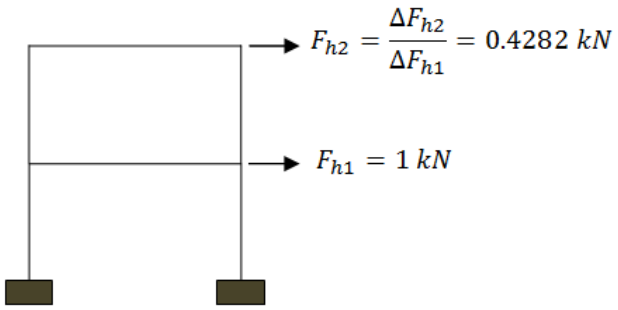

Figure 20: Solicitation of the indirectly affected part

1.3.1. Determine, in the critical sections of the indirectly affected part, the ΔM's due to this solicitation (column n°3 in Table 2)

1.4. On the basis of these ΔM's, compute a multiplier for each critical section (column n°5 in Table 2)

The first hinge will occur in the critical section that has the smallest multiplier.

In the example of Table 2, the first hinge appears at the internal extremity of the inferior beam, for a multiplier of 529,6.

1.5. Knowing this value of the multiplier, deduce the values of the bending moments in the critical sections when the first hinge forms (column 6 of Table 2)

1.5.1. For the horizontal displacements:

As the multiplier is known, the variation of F_{h1} is known and so, the variation of the horizontal displacements can be known (see Table 3).

1.5.2. For the vertical displacement at the top of the lost column

At step 1.2.1, the curves $Q - F_h$ and $\Delta_A - F_h$ were obtained, so, knowing the variation of F_{h1}, the value Q and Δ_A can be known

1.6. Finally, all the forces and displacements in the structure are known when the first hinges occurs in the indirectly affected part

Table 2. Evolution of the bending moments until the formation of the first hinge

Critical sections	M_0, the bending moments in the critical sections at the end of phase 2 [kN.m]	ΔM, the bending moments under the solicitation described in Figure 20 [kN.m]	M_{pl}, the plastic bending moment of the considered critical section[kN.m]	$\lambda = \frac{M_{pl}-M_0}{\Delta M}$,the multiplier [-]	M_1, the bending moment in the critical sections when the first hinge forms $M_1 = M_0 + \lambda_{min} * \Delta M$ [kN.m]
External column, base	-50	1.5478	1200	807.597881	769.736958
External column, summit	$-100 = -50 * 2$	0.8982	1200	1447.33912	375.699532
Internal column, base	-65	1.6068	1000	662.808066	785.9842
Internal column summit	$-130 = -65 * 2$	0.946	1000	1194.50317	371.015094
External extremity of the inferior beam	-200	1.1264	1000	1065.34091	396.557507
Internal extremity of the inferior beam	400	1.1329	1000	529.614264	1000
Internal extremity of the superior beam	430	0.5363	1000	1062.838	723.49987

Table 3. Evolution of the horizontal displacements (until first hinge)

	At the end of phase 2	When the first hinge forms
δ_{h1}	0	$0 + \Delta\delta_{h1} = \frac{\Delta\delta_{h1}}{\Delta F_{h1}} * \Delta F_{h1} = \left(\frac{0.0238}{1000} + \frac{0.0337}{1000} * \frac{\Delta F_{h2}}{\Delta F_{h1}}\right) * \Delta F_{h1}$ $= \left(\frac{0.0238}{1000} + \frac{0.0337}{1000} * 0.4282\right) * 529{,}6$ $= 0.02025\ m = 2.025\ cm$
δ_{h2}	0	$0 + \Delta\delta_{h2} = \frac{\Delta\delta_{h2}}{\Delta F_{h1}} * \Delta F_{h1} = \left(\frac{0.0337}{1000} + \frac{0.0823}{1000} * \frac{\Delta F_{h2}}{\Delta F_{h1}}\right) * \Delta F_{h1}$ $= \left(\frac{0.0337}{1000} + \frac{0.0823}{1000} * 0.4282\right) * 529.6$ $= 0.036511\ m = 3.65\ cm$

2. Step 2:

2.1. determine the value of $s_{d,ij}$ and $s_{g,i,j}$ considering that there is ONE plastic hinge in the indirectly affected part, in the critical section identified at the last step (Figure 21).

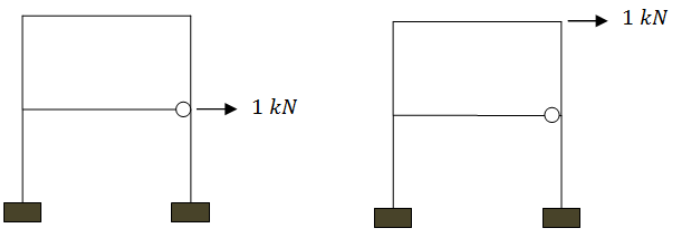

Figure 21. Determination of the stiffness matrix of the indirectly affected part (left part represented) if one hinge is developed

The stiffness matrix of the indirectly affected part is modified, and the relations between the horizontal displacements and forces become:

$$\delta_{h1} = \frac{0.0328}{1000} * F_{h1} + \frac{0.0535}{1000} * F_{h2}$$

$$\delta_{h2} = \frac{0.0535}{1000} * F_{h1} + \frac{0.1264}{1000} * F_{h2}$$

2.2. solve the equations developed in paragraph I.1.3 with these value of $s_{d,ij}$ and $s_{g,i,j}$

2.2.1. obtain the curves $Q - F_h$ and $\Delta_A - F_h$

2.2.2. obtain the ratios between F_{h1} and F_{h2}, F_{h1} and F_{h3}, F_{h1} and $F_{h\dots}$, F_{h1} and $F_{hn_{st}}$. Here, when the system of equations is solved, the ratio $\frac{F_2}{F_1} = 0.3393$

2.3. solve the indirectly affected part submitted to $F_{h1} = 1\ kN$ and F_{hi} determined at the precedent step 2.2.2:

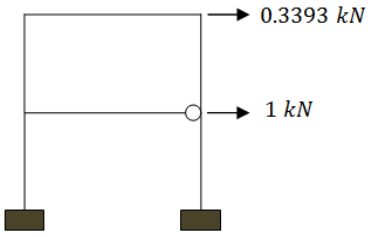

Figure 22. Solicitation of the indirectly affected part when one hinge

2.3.1. Determine, in the key element of the indirectly affected part, the ΔM's due to this solicitation (column n°3 in Table 4)

2.4. On the basis of these ΔM's, compute a multiplier for each critical section (column n°5 in Table 4)

The second hinge will occur in the critical section that has the smallest multiplier.

In the example of Table 4, the second hinge in the indirectly affected part appears in the base of the internal column, for a multiplier of 127.55.

2.5. Knowing this value of the multiplier, deduce the values of the bending moments in the critical sections when the second hinge forms (column 6 of Table 4)

2.5.1. For the horizontal displacements:

As the multiplier is known, the variation of F_{h1} is known and so, the variation of the horizontal displacements can be known (see Table 5)

2.5.2. For the vertical displacement at the top of the lost column

At step 2.2.1, the curves $Q - F_h$ and $\Delta_A - F_h$ were obtained, so, knowing the variation of F_{h1}, the value Q and Δ_A can be known

2.6. Finally, all the forces and displacements in the structure are known when the second hinge occurs in the indirectly affected part

3. Step 3

And so on, until a plastic mechanism is reached in the indirectly affected part.

Table 4. Evolution of the bending moments until the formation of the second hinge

Critical sections	M_0, the bending moments when the first hinge forms [kN.m]	ΔM, the bending moments under the solicitation described in Figure 22 [kN.m]	M_{pl}, the plastic bending moment of the considered critical section [kN.m]	$\lambda = \frac{M_{pl}-M_0}{\Delta M}$, the multiplier [-]	M_1, the bending moment in the critical sections when the second hinge forms $M_1 = M_0 + \lambda_{min} * \Delta M$ [kN.m]
External column, base	769.736958	1.8735	1200	229.657348	1008.7015
External column, summit	375.699532	0.8018	1200	1028.06244	477.968957
Internal column, base	785.9842	1.6779	1000	127.549794	1000
Internal column summit	371.015094	0.3344	1000	1880.93572	413.667745
External extremity of the inferior beam	396.557507	0.9304	1000	648.583935	515.229836
Internal extremity of the inferior beam	1000	0	1000	–	1000
Internal extremity of the superior beam	723.49987	0.6615	1000	417.989615	807.874059

Table 5. Evolution of the horizontal displacements (until 2nd hinge)

	When the first hinge forms	When the second hinge forms
δ_{h1}	$0.02025\ m$	$0.02025 + \Delta\delta_{h1} = \frac{\Delta\delta_{h1}}{\Delta F_{h1}} * \Delta F_{h1} = 0.02025 + \left(\frac{0.0328}{1000} + \frac{0.0535}{1000} * \frac{\Delta F_{h2}}{\Delta F_{h1}}\right) * \Delta F_{h1}$ $= 0.02025 + \left(\frac{0.0328}{1000} + \frac{0.0535}{1000} * 0.3393\right) * 127.55$ $= 0.02675\ m = 2.67\ cm$
δ_{h2}	$0.036511\ m$	$0.36511 + \Delta\delta_{h2} = \frac{\Delta\delta_{h2}}{\Delta F_{h1}} * \Delta F_{h1} = 0.036511 + \left(\frac{0.0535}{1000} + \frac{0.1264}{1000} * \frac{\Delta F_{h2}}{\Delta F_{h1}}\right) * \Delta F_{h1}$ $= 0.036511 + \left(\frac{0.0535}{1000} + \frac{0.1264}{1000} * 0.3393\right) * 127.55$ $= 0.0488m = 4.88\ cm$

I.3. 3D-frame

For the analytical study of a 3D-frame (still considered with no slab), the idea is the same as for the 2D-case: write equations for a substructure containing all the directly affected part, in which the indirectly affected one is replaced by horizontal springs. The substructure is now a 2*2D-substructure (Figure 23). Indeed, it is assumed here that the two main perpendicular plans are not coupled to each other. Moreover, the frames are assumed to be uncoupled to the other frames parallel to them (Figure 24).

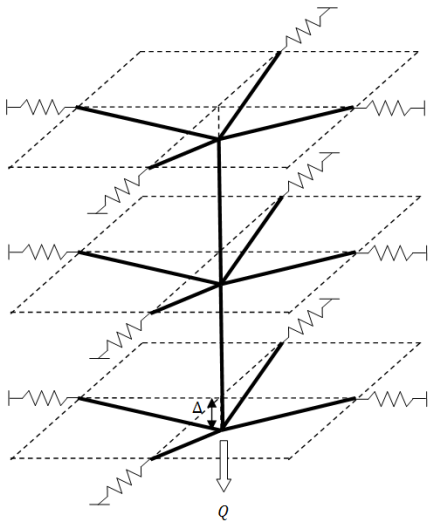

Figure 23. 2*2D-substructure

Indeed, in reality, when membrane forces develop in the directly affected part, not only the two perpendicular plans containing the lost column are influenced. Actually, when membrane beams pull on the indirectly affected part in the "x" direction, the other frames (parallels to "x") tend to restraint the horizontals displacements and so, bring an additional stiffness to the system. Moreover, when the directly affected part pulls on the "x" direction, there is also displacement in the "y" direction.

So here it is assumed that the two perpendicular frames containing the lost column are totally independent, from each other but also from the other frames that are parallel to them (Figure 24).

Accordingly, it is possible to study a 3D-frame through the study of two 2D-substructures, so the equations developed in paragraph I.1.3 can be applied in the two perpendicular directions.

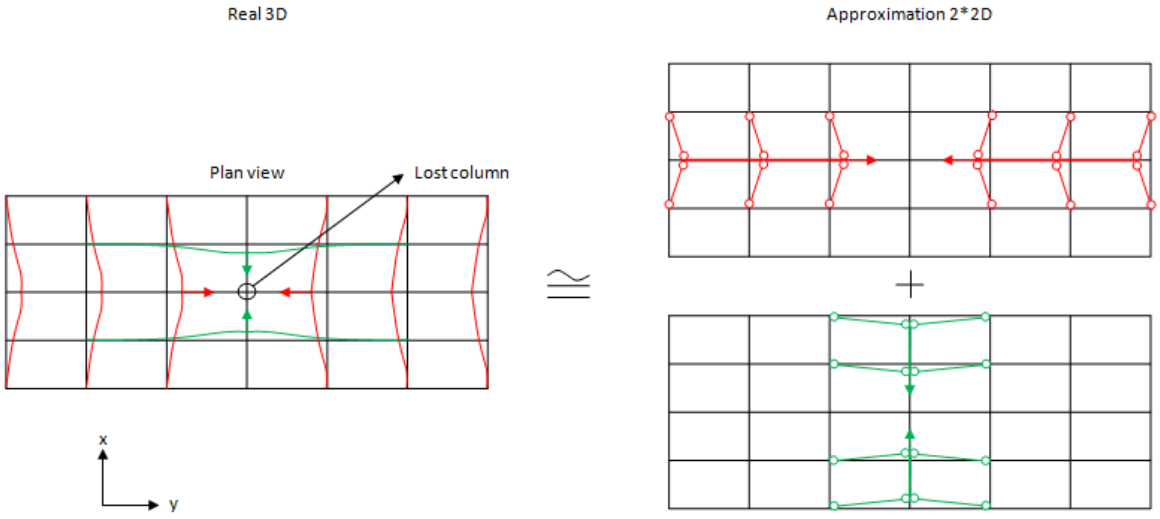

Figure 24. 2*2D approximation

So the analysis is a 2 times 2D analysis, and the equations developed in I.1.3 can be used for each direction. The unknowns and the equations are summarized here below.

Summary

Unknowns and available equations

Unknowns		Equations	
Q	1	$\Delta = fixed\ value$	1
Δ	1	$Q = Q_{1x} + Q_{1y} + Q_{2x} + Q_{2y} \dots + Q_{n_{st},x} + Q_{n_{st},y}$	1
Q_i	$2 * n_{st}$	$\Delta = \Delta_1 = \Delta_2 = \cdots = \Delta_{n_{st}}$	n_{st}
N_i	$2 * n_{st}$	$Q_{i_y}^{x} = 2 * N_{i_y}^{x} * \sin\theta_{i_y}^{x} + 2 * \frac{M_{HOG_{i_y}^{x}} - M_{SAG_{i_y}^{x}}}{L_{i_y}^{x}} * \cos\theta_{i_y}^{x}$	$2 * n_{st}$
$M_{HOG,i}$	$2 * n_{st}$	$N_{i_y}^{x} = F_{h,i_y}^{x} * \cos\theta_{i_y}^{x} + \frac{Q_{i_y}^{x}}{2} * \sin\theta_{i_y}^{x}$	$2 * n_{st}$
$M_{SAG,i}$	$2 * n_{st}$	$\tan\theta_{i_y}^{x} = \frac{\Delta_i}{L_{0_y}^{x} - \frac{\delta_{d,i_y}^{x} + \delta_{g,i_y}^{x}}{2}}$	$2 * n_{st}$
$\delta_{N,SAG,i}$	$2 * n_{st}$	$L_{i_y}^{x} = \sqrt{\left(L_{0_y}^{x} - \frac{\delta_{d,i_y}^{x} + \delta_{g,i_y}^{x}}{2}\right)^2 + \Delta_i^2}$	$2 * n_{st}$
$\delta_{N,HOG,i}$	$2 * n_{st}$	$L_{i_y}^{x} = L_0 + \delta_{N,SAG,i_y}^{x} + \delta_{N,HOG,i_y}^{x}$	$2 * n_{st}$
θ_i	$2 * n_{st}$	$\Delta_{h,i_y}^{x} = \frac{\delta_{d,i_y}^{x} - \delta_{g,i_y}^{x}}{2}$	$2 * n_{st}$
$F_{h,i}$	$2 * n_{st}$	$M_{HOG,i_y}^{x} = f\left(N_{i_y}^{x}\right)$	$2 * n_{st}$
L_i	$2 * n_{st}$	$M_{SAG,i_y}^{x} = f\left(N_{i_y}^{x}\right)$	$2 * n_{st}$
$\Delta_{h,i}$	$2 * n_{st}$	$\delta_{N,SAG,i_y}^{x} = f(N_{i_y}^{x})$	$2 * n_{st}$
Δ_i	n_{st}	$\delta_{N,HOG,i_y}^{x} = f(N_{i_y}^{x})$	$2 * n_{st}$
$\delta_{g,i}$	$2 * n_{st}$	For x and y directions : $\delta_{g,n_{st}} = s_{g,1,n_{st}} * F_1 + s_{g,2,n_{st}} * F_2 + \cdots + s_{g,n_{st},n_{st}} * F_{n_{st}}$ ... $\delta_{g,2} = s_{g,1,2} * F_1 + s_{g,2,2} * F_2 + \cdots + s_{g,n_{st},2} * F_{n_{st}}$ $\delta_{g,1} = s_{g,1,1} * F_1 + s_{g,2,1} * F_2 + \cdots + s_{g,n_{st},1} * F_{n_{st}}$	$2 * n_{st}$
$\delta_{d,i}$	$2 * n_{st}$	For x and y directions : $\delta_{d,n_{st}} = s_{d,1,n_{st}} * F_1 + s_{d,2,n_{st}} * F_2 + \cdots + s_{d,n_{st},n_{st}} * F_{n_{st}}$ ... $\delta_{d,2} = s_{d,1,2} * F_1 + s_{d,2,2} * F_2 + \cdots + s_{d,n_{st},2} * F_{n_{st}}$ $\delta_{d,1} = s_{d,1,1} * F_1 + s_{d,2,1} * F_2 + \cdots + s_{d,n_{st},1} * F_{n_{st}}$	$2 * n_{st}$
TOTAL =	$25 * n_{st} + 2$	TOTAL=	$25 * n_{st} + 2$

Input data's:

- L_{0x} and L_{0y}, the initial lengths of the beams (primary and secondary)
- The matrix of rigidity of the indirectly affected part (terms $s_{d,i,j}$ and $s_{g,i,j}$ in the two perpendicular directions)(paragraph I.1.3)
- The $M-N$ interaction law, in both hogging and sagging, for the two directions. As previously said, if the hinge forms in the joint, the M-N resistant interaction curve can be determined following the method described in Deliverable 3.
- The law between $\delta_{N,SAG}$ and N and the law between $\delta_{N,HOG}$ and N, for the two directions. As previously said, these laws are still under investigation, and are, for now, assumed to be linear ($K_N * \delta_N = N$, the values given to the parameters K_N can be found in Deliverable 6)

Solving procedure

For a given value of Δ, and since the number of unknowns is equal to the number of equations, this equations system can be solved (for example, using MATLAB), and the value of Q corresponding to the given value of Δ can be obtained.

I.4. Application of the global model to the investigated car park

I.4.1. Specificities and simplifications

Now that the general method has been presented, for 2D and 3D structures, the study case of the ROBUSTFIRE project (designed within WP5) is examined. Its specificities are as follows:

- The beams are composite beams
- There is a reinforced concrete slab "linking" these composite beams
- The exceptional event is a fire occurring next to a supporting column
- There is a bracing system in the two main directions

To apply the global model, the following assumptions are made:

- The first assumption is to consider that, due to the fire, the column is completely lost and there is no remaining strength in the column.
- The second assumption consists in considering that the extremities of the substructure are totally fixed. Indeed, it can be assumed that, thanks to the bracing systems in both directions and the slabs acting as diaphragms and ensuring the formation of a compression ring, the rigidity of the indirectly affected part is very high against membrane forces.
- The third assumption is to neglect the beneficial effect of the slab on the behaviour of the directly affected part. Only a mesh of composite beams will be considered.
- The fourth assumption is to neglect the heated beams, just above the lost column. Indeed, its rigidity will be very small compared to the other stories, so the contribution of the first storey to the structural resistance is considered as negligible.

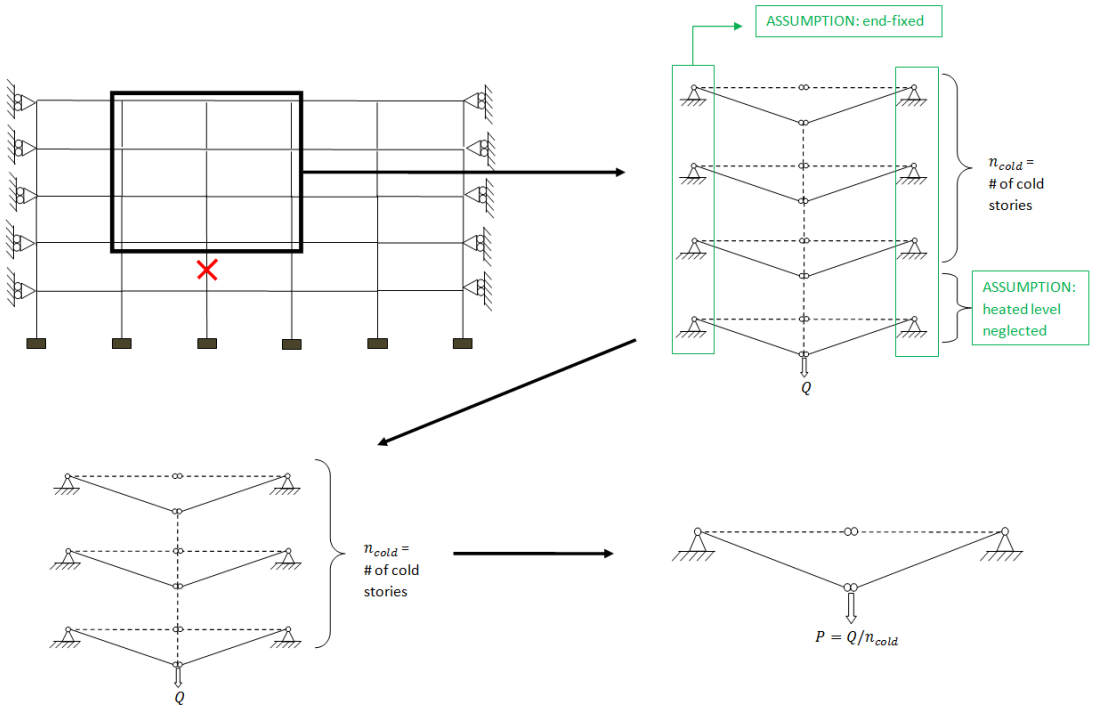

Figure 25. Simplifications for the case study

All these assumptions are summarized in Figure 25. The substructure to be studied at the end is only composed with a single double-beam, at ambient temperature, submitted to a force P equal to the total load Q acting on the structure, divided by the number of cold stories, n_{cold}. Indeed, as the extremities of the beams at each storey are assumed to be fixed and as the beams are the same, the storey can be studied independently as illustrated in Figure 25 and the load Q is uniformly distributed between the storeys. In Figure 25, a 2D-frame is represented. In the case study, it is a 3D-frame, so the substructure to study will be composed with two double-beams, one in each plan.

Remark: if the lost column is at the last storey, $n_{cold} = 0$. In this case, only the slab will be considered, and the heated beams will be neglected. Accordingly, the analytical model presented in paragraph 2 of Deliverable 5 will have to be used.

I.4.2. Equations in 2D

The equations to be used for this substructure are the same as the one developed in paragraph I.1.3, but slightly simplified.

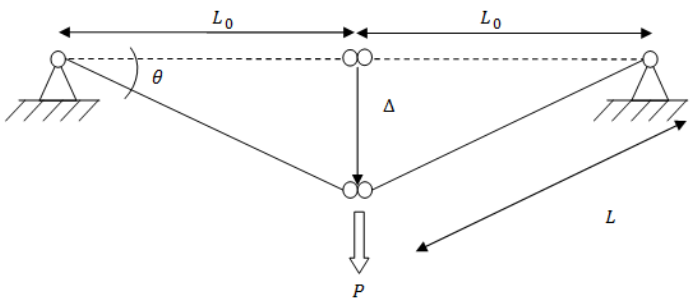

Figure 26. Single double-beam, ends fixed

– Forces equilibrium

$$P = 2 * N * \sin\theta + 2 * \frac{M_{HOG} - M_{SAG}}{L} * \cos\theta \quad (1)$$

$$N = F_h * \cos\theta + \frac{P}{2} * \sin\theta \quad (2)$$

– Displacement compatibility

$$\tan\theta = \frac{\Delta}{L_0} \quad (3)$$

$$L = \sqrt{L_0^2 + \Delta^2} \quad (4)$$

$$L = L_0 + \delta_{N,SAG}(N) + \delta_{N,HOG}(N) \quad (5)$$

– M-N interaction

$$M_{HOG} = f(N) \quad (6)$$

$$M_{SAG} = f(N) \quad (7)$$

– $\delta_N - N$ law

$$\delta_{N,SAG} = f(N) \quad (8)$$

$$\delta_{N,HOG} = f(N) \quad (9)$$

As can be seen in formulas (3) and (4), the value of θ and L can directly be obtained for a given value of Δ. Then the system of equations (1), (5), (6), (7), (8) and (9) can give the values of P, N, M_{HOG}, M_{SAG}, $\delta_{N,SAG}$ and $\delta_{N,HOG}$. Finally, the equation (2) can give F_h knowing the other variables.

I.4.3. Equations in 3D (2*2D)

For the 3D case, as said before, a 2*2D analysis is considered and the substructure is composed with 2 double-beams, one in each direction, and both with fixed-ends (Figure 27).

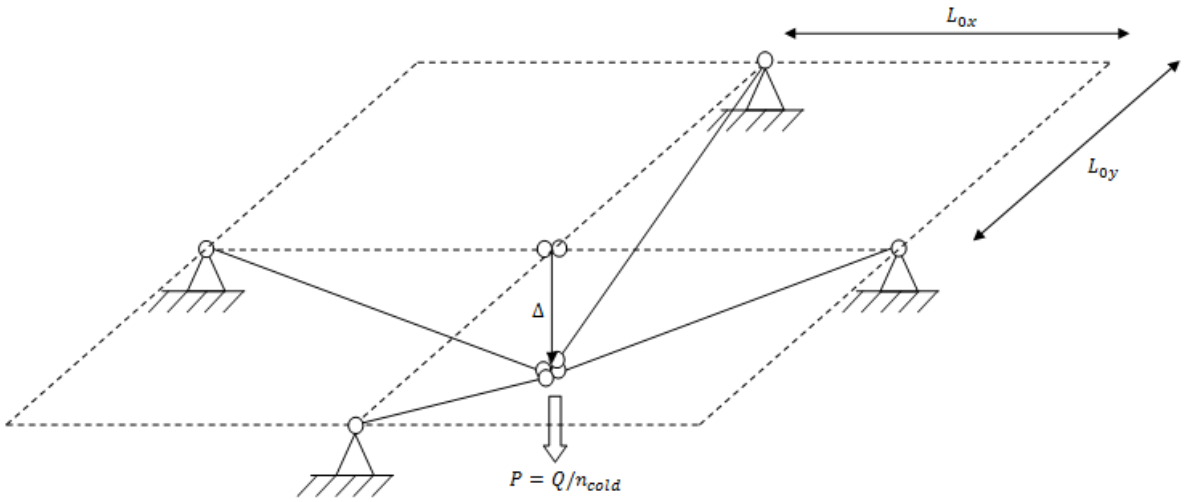

Figure 27. 2*2D substructure, ends fixed

The solving procedure for the complete case is the following:

– choose a value of Δ
– for this value of Δ, compute:
  ○ $\theta_x = \arctan\frac{\Delta}{L_{0x}}$
  ○ $\theta_y = \arctan\frac{\Delta}{L_{0y}}$
  ○ $L_x = \frac{L_{0x}}{\cos\theta_x}$
  ○ $L_y = \frac{L_{0y}}{\cos\theta_y}$
– solve the following system of equations:
  ○ $P = 2 * N_x * \sin\theta_x + 2 * \frac{M_{HOG,x} - M_{SAG,x}}{L_x} * \cos\theta_x + 2 * N_y * \sin\theta_y + 2 * \frac{M_{HOG,y} - M_{SAG,y}}{L_y} * \cos\theta_y$
  ○ $L_x = L_{0,x} + \delta_{N,SAG,x} + \delta_{N,HOG,x}$
  ○ $L_y = L_{0,x} + \delta_{N,SAG,y} + \delta_{N,HOG,y}$

Indeed, in these 3 equations, the 11 unknowns are:

- P
- N_x and N_y
- $M_{HOG,x}$, $M_{SAG,x}$ and $M_{HOG,y}$, $M_{SAG,y}$
- $\delta_{N,HOG,x}$, $\delta_{N,SAG,x}$ and $\delta_{N,HOG,y}$, $\delta_{N,SAG,y}$

The 8 "missing" equations are the links between $M - N$ and $\delta_N - N$:

- $M_{HOG,x} = f(N_x)$
- $M_{SAG,x} = f(N_x)$
- $M_{HOG,y} = f(N_y)$
- $M_{SAG,y} = f(N_y)$
- $\delta_{N,HOG,x} = f(N_x)$
- $\delta_{N,SAG,x} = f(N_x)$
- $\delta_{N,HOG,y} = f(N_y)$
- $\delta_{N,SAG,y} = f(N_y)$

There are as many equations as there are unknowns so the system can be solved. Finally, the value of P corresponding to the chosen Δ can be found.

The input data's for this method are the following:

- L_{0x} and L_{0y}, the initial lengths of the beams in the two directions
- The interaction laws $M - N$ for both sagging and hogging, and for the two perpendicular directions (see Deliverable 3for the computation of M-N resistant interaction laws for joints)
- The law between δ_N and N, laws that cannot be, at this stage of the developments, determined analytically. It is assumed to be linear ($K_N * \delta_N = N$, the values given to the parameters K_N can be found in Deliverable 6)

A Matlab-code (with an explanation note) that solves these equations can be found in the annexes of Deliverable 6.

II. References

[1] Demonceau J.-F. (2008), "Steel and composite building frames: sway response under conventional loading and development of membrane effects in beams further to an exceptional action", PhD Thesis realised at the ULg.

[2] U. Kuhlmann, L. Rolle, J.P. Jaspart, J.F. Demonceau, O. Vassart, K. Weynand, C. Ziller, E. Busse, M. Lendering, R. Zandonini and N. Baldassino. « Robust structures by joint ductility », Final report, Science Research Development, European Commission, 2008.

[3] Luu N.N.H. (2009), "Structural response of steel and composite building frames further to an impact leading to the loss of a column", PhD Thesis realised at the ULg.

[4] Lemaire F. (2010), "Etude du comportement 3D de structures en acier ou mixtes lors de la perte d'une colonne", Master Thesis realised at the ULg.

[5] Huvelle C. (2011), "Contribution à l'étude de la robustesse des structures de bâtiments. Prise en compte de la plastification progressive de la structure « non directement » affectée par l'évènement exceptionnel considéré", Master Thesis realised at the ULg.

[6] Six-monthly report of Robustfire project

[7] Deliverable 3 (paragraph on M-N interaction in joints)